UNIVERSITY OF NICE - SOPHIA ANTIPOLIS
DOCTORAL SCHOOL STIC
SCIENCES ET TECHNOLOGIES DE L'INFORMATION
ET DE LA COMMUNICATION

PHD THESIS

to obtain the title of

PhD of Science

of the University of Nice - Sophia Antipolis
Specialty : AUTOMATISME, TRAITEMENT DU SIGNAL ET DES IMAGES

Defended by

Marco LORENZI

Deformation based morphometry of the brain for the development of surrogate markers in Alzheimer's disease

Thesis Advisor: Xavier PENNEC

prepared at INRIA Sophia Antipolis, ASCLEPIOS research group
defended on December 20th, 2012

Reviewers :	Olivier COLLIOT	-	CNRS - ICM
	Sebastien OURSELIN	-	University College London
	Daniel RUECKERT	-	Imperial College London
Advisors :	Xavier PENNEC	-	INRIA Asclepios
	Nicholas AYACHE	-	INRIA Asclepios
Jury President:	Giovanni B. FRISONI	-	IRCCS San Giovanni di Dio Fatebenefratelli

Acknowledgments

I would like first to thank my thesis advisor, Xavier Pennec. His invaluable guidance was fundamental for the success of this project, and his creativity and passion for research will be always an important source of inspiration for my work. I would also to gratefully acknowledge Nicholas Ayache for his precious advises, and for the enthusiasm and positivity that he can always transmit in our meetings. I wish to express my deepest gratitude to Giovanni Frisoni, who trusted and strongly supported me since my first steps in this field. This project is also the result of his openness and enthusiasm.

A sincere thank to the jury members Olivier Colliot, Daniel Rueckert and Sebastien Ourselin, who reviewed this manuscript and provided me important insights for the future development of my work.

I would also like to take the opportunity to thank Marc Niethammer, Bjoern Menze and Stephen Marsland, for the insteresting discussions and time spent together during their visit to Asclepios team, and I'm greateful to Isabelle Strobant and to the administrave office of IRCCS Fatebenefratelli for the kind help in organizing the PhD project.

This PhD was a wonderful opportunity to share time and experiences with colleagues and friends from Asclepios and LENITEM teams. I'm greateful to all of them, in particular to Tommaso Mansi, who took care of me during my first times at Asclepios; Christof Seiler, for showing me how easily days can be longer than 24h; Vikash Gupta, for hosting and feeding me in the moment of need; Martina Bocchetta, for all the things I learnt from her. I would also to specially thank Rossana Ganzola, Federico Spadoni, Moira Marizzoni, Alberto Redolfi, Chiara Barattieri, Hervé Lombaert, Maxime Sermesant, Vincent Garcia, Stephan Schmidt and Andrew Sweet.

I would like finally to thank my mother and my father for their continuous support and influence, and Barbara, for being my closest supporter and for understanding me despite the sometimes difficult moments. Thank you!

Table of Contents

Chapter 1

Introduction

Contents

1.1 Alzheimer's Disease

Alzheimer's disease (AD) is a neurodegenerative pathology of the brain, and is the most common form of dementia. This disease is diagnosed typically in elderly people, but early appearance of symptoms may happen before the age of 65, especially in presence of specific genetic factors (familial AD). Even though AD is a progressive disease and may develop differently in individuals, a set of common symptoms can be identified at the earlier stages like memory and functionality loss, mood alterations, and a general difficulty in carrying out everyday activities. As the disease progresses, the impairment in memory, communication and mobility worsens, and the individuals gradually become totally dependent on the caregivers. The worldwide prevalence of AD in the world is 26.6 millions and it was estimated that, based on the current United Nations projections, it might quadruple by the year 2050, leading to a "looming epidemic" [Brookmeyer et al., 2007]. The estimation is a consequence of the global aging of the world's population. At the present moment there is neither cure nor preventive measures for this pathology [Daviglus et al., 2010]. It becomes therefore evident the burden on the society in terms of enormous social and economical costs [Demokis, 2007], and even mild therapeutic advancement in slowing down the pathological progression would result in significant benefits for patients, caregivers, and more generally on the healthcare system.

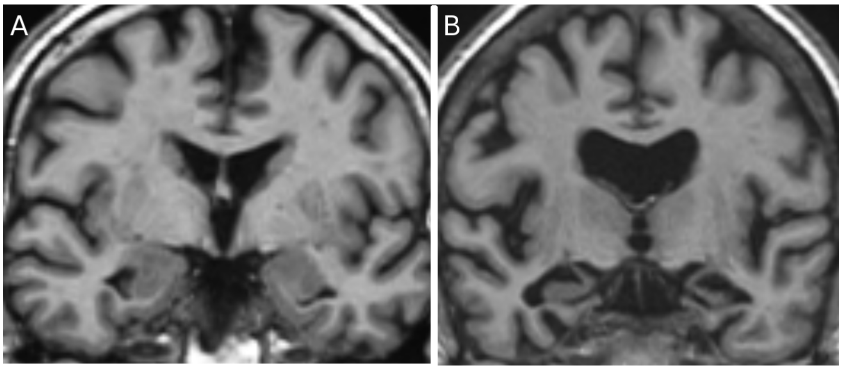

Figure 1.1: High resolution T1 MRIs of A) an healthy elder (005_S_0602) and B) an AD subjects (005_S_0221) of the ADNI database.

1.1.1 AD Mechanisms and Treatments

AD is characterized by the co-occurrence of different phenomena, starting from the deposition of amyloid plaques and neurofibrillary tangles, to the progressive synaptic, neuronal and axonal damage. These findings reported by several independent scientific studies led recently to the formulation of the so called "amyloid cascade hypothesis" [Jack et al., 2010a], in which the authors proposed a temporal model for the progression of the neurodegenerative biomarkers in AD. According to this model, the pathology is initiated by the accumulation of amyloid deposits in the brain, which can occur decades before the development of the clinical symptoms. The amyloid deposition induces a cascade of pathological processes which lead to the endpoint of stereotypical pattern of neuronal loss in the temporal and cortical areas (Figure 1.1). Above a certain threshold of structural damage, the amnestic symptoms progressively increase from the initial appearance of memory disturbance, which characterizes the clinical intermediate stage commonly defined as amnestic mild cognitive impairment (MCI), to the widespread cognitive deficits in multiple domains (Figure 1.2).

The recent failure of AD anti-amyloid drugs in showing a protective effect against neurodegeneration [Palmer, 2011] led to the current rediscussion of the amyloid cascade model [Fjell and Walhovd, 2012]. This pointed also the attention to the evaluation of the treatments in the presymptomatic and even prodromal stages of the disease, when the effectiveness of the drug can be maximised and the pathology is not yet in the more advanced and probably irrecoverable stages [Reiman et al., 2010].

1.1.2 The Role of MRI in the Study of AD

Structural atrophy of the whole brain characterizes the transition from MCI to AD and it was shown to strongly correlate with cognitive performance and neuropsychological scores [Jack et al., 2003]. As can be noted in Figure 1.2, the brain atrophy appears at the early stages of the disease and increases progressively with the disease

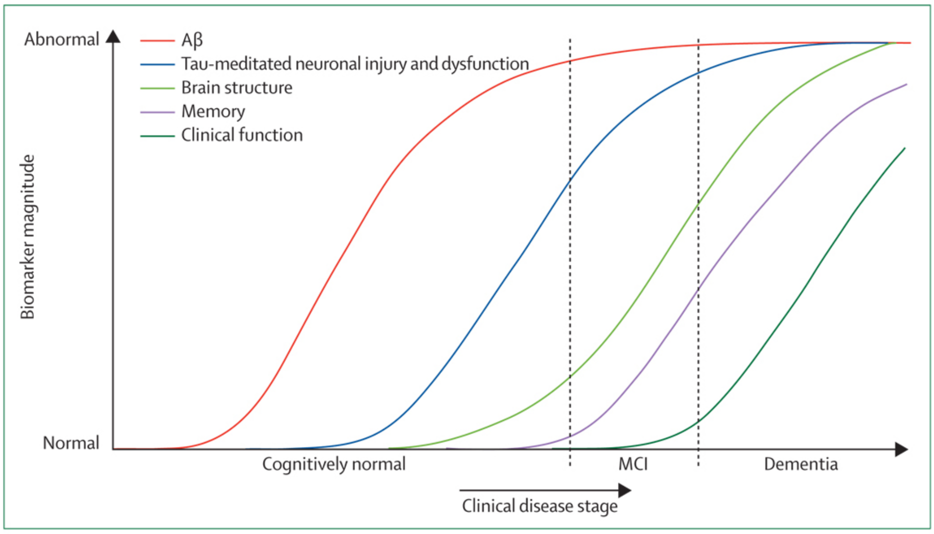

Figure 1.2: Hypothetical model of Alzheimer's disease based on the "amyloid cascade hypothesis" (from [Jack et al., 2010a]).

evolution until reaching a plateau level. Most importantly, the structural atrophy is more sensitive to the progression from pre-clinical to pathological stages than amyloid markers which reach the plateau earlier.

In light of these observations, the brain atrophy detectable from magnetic resonance imaging (MRI) was included as an AD marker in the diagnostic criteria of Alzheimer's disease [Dubois et al., 2007], and is a potential surrogate outcome measure for the monitoring of the disease progression in phase II and III clinical trials. Indeed, increasing evidence indicates that structural markers are more precise and stable than the standard cognitive and functional neuropsychological scales [Fox et al., 2000, Jack et al., 2004].

A valid marker of disease progression should provide low variability and high precision in tracking the atrophy in order to guarantee the highest statistical power in detecting treatment effects, and therefore to allow shorter trial durations with smaller groups of patients. Several markers of AD based on structural MRI have been proposed and are currently under study [Frisoni et al., 2010]. The most accepted and established are the atrophy detectable on high-resolution T1 weighted MRI, assessed in the whole brain, or in sensitive regions like the hippocampi, temporal lobes, or ventricles (Figure 1.1). At the clinical level, qualitative scales of the temporal atrophy have been developed for the classification of the pathological stages [DeCarli et al., 2007], while volumetric measures were historically computed through manual tracing of the anatomical structures. Manual measurements are however time consuming, require trained operators and are characterized by large inter-subject variability. This poses the problem of the reliable estimation and comparison of atrophy measures in large multicentric studies.

1.2 Computational Anatomy for Research and Therapy in AD

AD is a complex pathology whose aetiology is unknown. In absence of a definitive pathophysiological model, large studies are currently ongoing for providing more insights on the biology and evolution of the disease. As a result, we are already witnessing the increase of multicentric and longitudinal studies, with the associated large amount of medical data to consistently process and analyze. The need of automatic methods for the serial analysis of medical images, in particular MRIs, is therefore evident for helping the research in understanding and quantifying the pathology across its temporal stages.

An important contribution to the recent understandings of AD and to the technical developments on the atrophy measurements came indeed from "Computational Anatomy", the discipline of modeling and analysing the structure of organs through mathematical and computational methods, which is now playing a central role in both research and therapeutic fields. Computational anatomy is the toolkit for virtually "dissecting" medical images: processing, analysing and quantifying the digital data. *Non-rigid registration* is one of the main instruments for the morphological analysis of brain structures. Non rigid-registration models the structural differences between pairs of images as local spatial transformations which, based on opportune similarity criteria, match homologous anatomical regions [Holden, 2008, Modersitzki, 2004]. This way, we can describe a given anatomy with respect to a reference one, and derive from the spatial transformation the features of interest which can be used to model and quantify the anatomical changes.

1.2.1 Non-Rigid Registration: discoverying the AD dynamics

Since the late 90's of the past century computational methods for the statistical analysis of brain MRI were proposed for group-wise (*cross-sectional*) and *longitudinal* studies of clinical populations. These methods provided for the first time statistical atlases of the spatial distribution of atrophy in AD, and highlighted temporal and spatial dynamics of the pathology. These methods mostly rely on non-rigid registration of the structural images to a pre-defined anatomical template [Ashburner et al., 1998].

Deformation based morphometry for cross-sectional analysis.

A classical approach for morphological studies is the so-called "deformation based morphometry", which is based on the analysis of the deformations estimated by non-rigid registration. In particular, the Jacobian determinant (or Jacobian) $|\nabla\varphi|$ of a deformation φ quantifies the associated local volume change, and is widely used for the quantification of the atrophy. The Jacobian is densely computed in the image at the voxel level and locally describes the volume change with respect to the anatomical reference, thus the matter growth and loss associated to

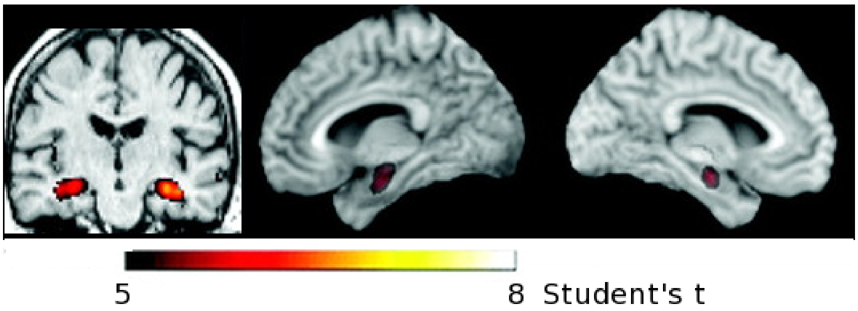

Figure 1.3: Voxel based morphometry. Areas of statistically significant grey matter loss in AD patients as compared to a reference healthy group (from [Frisoni et al., 2009])

the deformation at the specific location. In *tensor based morphometry* (TBM), the Jacobian determinant scalar fields are compared between clinical groups by means of voxel-by-voxel statistical models, for instance for testing the difference in mean atrophy between patients and control groups. Maps of coefficients and p-values are then thresholded and analyzed to identify the anatomical areas of significant difference [Chung et al., 2001, Gaser et al., 2001, Riddle et al., 2004]. A similar approach is used in *voxel based morphometry* (VBM), where the probabilistic segmentations of the gray and white matter tissues are compared voxel-wise (Figure 1.3). The intensities of the probabilistic masks are usually scaled by the Jacobian determinant of the suject-to-template transformation, in order to account for the transport of the tissue masks in the common reference space [Ashburner and Friston, 2000, Ashburner and Friston, 2005] .

Deformation based morphometry for longitudinal analysis.

In spite of the relatively straightforward application of deformation based morphometry in cross-sectional studies, the *longitudinal* setting was less investigated: the problem of modeling and comparing dynamic quantities, such as the changes measured in time series of images, is a more complex issue. As in the cross sectional setting, it was proposed to analyze the Jacobian determinant scalar fields associated to the longitudinal progressions estimated by the deformation fields [Fox et al., 2001, Scahill et al., 2002]. However, the Jacobian determinant is only a summary descriptor of the longitudinal deformations, which are characterized by complex and subtle dynamics and should then be compared on a multivariate basis to obtain more precise assessments and greater statistical significance. This requires to consistently *transport* the full deformations in a common reference.

When transporting we should ideally preserve the geometrical properties of the initial trajectory while adapting to the new coordinate system. Therefore, we are interested in the behavior of the transported dynamics, for instance regarding the ability to preserve the original amount of expansion/contraction in homologous regions.

A preliminary approach consists in performing the longitudinal analysis *after* the subject-to-template normalization [Chetelat et al., 2005, Thompson et al., 2003]. A key issue here is the different nature of the changes occurring at the intra-subject level, which reflects the biological phenomena of interest, and the changes across different subjects, which are usually large and not related to any biological process. In fact, the inter-subject variability is a scale of magnitude higher than the more subtle longitudinal subject-specific variations. To provide a more sensitive quantification of the longitudinal dynamics, the intra-subject changes should be modeled independently from the subject-to-template normalization, and only successively transported in the common reference for statistical analysis.

This is the approach adopted in [Qiu et al., 2008b], where the authors described the group-wise longitudinal shape evolution of the hippocampus in healthy aging and AD. The longitudinal atrophy trajectories were modeled with the “large deformation diffeomorphic metric mapping” (LDDMM) diffeomorphic registration framework, and were normalized to a common reference by “parallel transport” of the deformation vectors. The extension of such approach to a whole brain model of the longitudinal atrophy in AD is however difficult, due to the high computational cost of the LDDMM framework.

1.2.2 Non-Rigid Registration: quantifying the AD effects.

The methods described above are qualitative, i.e. aim to describe the anatomical differences without quantifying the observed changes. Hypothesis testing on voxel-by-voxel statistical models is a powerful instrument for exploratory studies, but is usually not robust for the reliable quantification of atrophy. For example, voxel-by-voxel statistical analysis are prone to the multiple comparisons problem which leads to type I errors. In fact, when multiple independent statistical tests are performed, the probability of false positives increases with the number of tests, and can be unacceptably high for the analysis on hundreds of thousands of voxels in a standard MRI, which must therefore be corrected with statistical techniques like Bonferroni or False Discovery Rate [Benjamini and Hochberg, 1995].

Structural brain imaging is an important surrogate measure in therapeutic trials, and novel techniques for the accurate quantification of the atrophy in AD are under active development. In fact, automated frameworks for the volume measurement and for the quantification of the longitudinal changes are potentially reliable, inexpensive, simple to perform and can be easily applied in multicentric trials.

The more natural approach for the volume measurement of anatomical structures is by segmentation. For instance, several automatic approaches were proposed for the whole brain [FreeBorough and Fox, 1997, Smith, 2002, Iglesias et al., 2011] and hippocampal segmentation [Crum et al., 2001, Fischl et al., 2002, Carmichael et al., 2005, van der Lijn et al., 2008, Chupin et al., 2009b, Lötjönen et al., 2011]. In the longitudinal setting segmentation measures are used to define ratio of volume change as in the “boundary shift integral”

[FreeBorough and Fox, 1997, Barnes et al., 2007], which quantifies the volume changes by computing the shift of the boundaries of the follow-up segmentations of the anatomical structure. This measure is currently employed in clinical trials.

Hippocampal segmentation has now reached good reliability, and seems mature for meeting the rigid qualitative standards required in the therapeutic field. This is essentially due to the good definition of the boundary of the structure on high resolution MRI which easies the automatic identification of the hippocampal surface. However, AD is not completely described by the atrophy in the hyppocampus and is characterized by a more complex pattern of structural loss all over the brain. Unfortunately other structures involved in the atrophy process, like the amygdalae and the enthorinal cortex, are more difficult to be visually or automatically identified in the MRI, and therefore are currently not monitored in therapeutic trials. This issue, which is purely technique, might lead to the inability to detect the more subtle drugs effects in the exquisitely local topography of progressive brain damage: the failure in the recent trials on AD to show significant treatment effects on the hippocampal volume changes led to question whether a more general atrophy analysis would have been able to detect possible benefits [Raschetti et al., 2007].

Deformation based morphometry for quantitative purposes

Deformation based morphometry might address this issue since it describes the atrophy process through spatially dense deformation fields, and thus provides anatomical quantifications which range from the local (voxel) to the regional level. Importantly, the estimated anatomical changes are independent from the ability to clearly delineate anatomical boundaries.

Non-rigid registration was used mainly to quantify average volume changes by integration of the Jacobian determinant on selected regions [Aljabar et al., 2008, Camara et al., 2008, Boyes et al., 2006, Gaser et al., 2001]. Moreover, the deformation fields provide several anatomical measures which might go beyond the classical average volume change [Chung et al., 2001]. For example, the mathematical counterpart of the boundary shift integral is the flux of the deformation across the boundaries of the region. However, these measures were seldom investigated partly due to the numerical complexity and the lack of robustness of the evaluation. As an example, computing the flux of the deformation across the boundaries of a region requires the computation of vector normals to surfaces, which normally leads to large approximation errors.

In spite of its wide use in research, non-rigid registration is barely employed for the longitudinal atrophy quantification in clinical trials. This is partly due to the higher technical requirements asked in the clinical context in terms of accuracy, robustness to the biases affecting the medical images, and stability of the measures over time. The failing in controlling these factors inevitably leads to a decreased sensibility of the atrophy measures, and thus to the potential failing or increase in cost of the trial.

Recently, [Fox et al., 2012] identified a set of “quality criteria” that an imaging tool should satisfy in order to find application in the clinical setting:

- *Biological plausibility.* The algorithm should provide atrophy measurements consistent with the known pathophysiology.
- *Symmetry.* The atrophy quantified from A to B should be consistent with the one quantified from B to A.
- *Transitivity.* The atrophy quantified from A to C should be equivalent to the cumulative one from A to B and B to C.
- *Comparison with the "state of art".* The atrophy measurements should be validated on shared data and compared to those obtained from more established algorithms.
- *Reproducibility on back-to-back images.* The group average on same days scans should be zero.
- *Statistical validation.* The accuracy of the measurements should be evaluated by sample size analysis based on the differential progression between AD and normal aging.

More validation efforts are therefore required to define a reliable imaging tool based on non-rigid registration which can be employed in both research and clinical settings.

1.3 Objectives and Contributions

The current research scenario for AD shows an increasing need for efficient, reliable and stable computational methods for the analysis of MRI. The problem is challenging and involves various aspects: the analysis over the 3 dimensional brain volume should be consistently integrated in the longitudinal dimension, while the exploration of the AD patterns of neurodegeneration should be followed by robust numerical quantification. Therefore, the new emerging challenge is the development of general computational frameworks whose elements could consistently interact to address all the above requirements.

The present PhD thesis aims to build a solid and reliable toolkit of computational instruments based on non-rigid registration for the consistent analysis of longitudinal MRIs, with the duplice purpose to provide the research with computationally efficient instruments for explorative longitudinal studies, and to define precise and stable quantification methods, to be effectively applied in the clinical domain.

This thesis is founded on the estimation of morphological changes by non-rigid registration parameterized by stationary velocity fields [Arsigny et al., 2006, Vercauteren et al., 2008]. When used with medical images, the non-rigid registration must be robust to the intensity biases and provide consistent measures of the anatomical changes. Computational efficiency is also a key factor for the successful employment in the practical context.

In chapter 2 we propose the LCC-Demons, a novel registration framework based on stationary velocity fields and built upon the log-Demons algorithm. The proposed framework is designed to target the above requisites. It allows the consistent evaluation of spatial changes as either average volume changes or boundary shift, by stable computation of the Jacobian determinant of the deformation. Moreover, the LCC-Demons robustly detects the anatomical changes in presence of affine biases on the intensities, is computationally efficient (around 20 minutes for registering high resolution T1 MRI images on an AMD Opteron dual core 2000Mhz without any specific GPU parallel optimization), and is comparable to the state-of-art methods for both inter-subject registration and intra-subject assessment of longitudinal changes. The chapter was submitted as a journal paper to NeuroImage [Lorenzi et al., 2012b].

Once we have an efficient and robust way to estimate longitudinal anatomical deformations in time series of a given patient, we address the problem of comparing the trajectories for different patients in a common reference. This is a central topic for the development of atlases for the longitudinal evolution of physiological processes in organs, like brain atrophy. So far a consensus on the methodology is not yet reached, and there are not publicly available instruments. In chapter 3 we propose an efficient and numerically stable computational scheme for the *parallel transport* of diffeomorphic deformation trajectories parametrized by tangent vectors. The scheme is based on the “Schild’s Ladder”, a method for transporting tangent vector fields in manifold with an affine connection that was introduced in Gravitation & Relativity in the 70ies. Here the method is applied to the estimation of a whole brain dynamic model of the longitudinal changes in AD. The chapter is based on the article [Lorenzi et al., 2011b] presented at the 22nd Information Processing on Medical Imaging conference (IPMI) in 2011. The article was awarded with the honorable mention (runner-up) for the prestigious Erbsmann prize.

Since our Schild’s Ladder theoretically requires the use of geodesics, we investigate in chapter 4 the relationship between the one-parameter subgroups parameterized by SVFs and geodesics. We review the basic properties of the finite dimensional Lie group and defined the Cartan connections, for which the one-parameter subgroups are geodesics, and we show that the parallel transport can be computed straightforwardly. Diffeomorphic image registration requires to generalize these properties in the infinite dimensional case, and this is theoretically not always possible. Our experiments put here into evidence the central role played by the discrete approximation and the numerical implementation, which may hide part of the theoretical issues. The same conclusion emerges when comparing the stationary velocity field setting to the LDDMM one. In case of longitudinal deformations, the settings provides similar and compatible results. The chapter is in press as a journal paper on International Journal of Computer Vision (IJCV) [Lorenzi and Pennec, 2012], and is based on the material presented at the 3rd Mathematical Foundation of Computational Anatomy workshop, hosted at MICCAI in 2011 [Lorenzi and Pennec, 2011].

We turn now in the second part of the manuscript, in which the previous methodological contributions are applied for defining novel instruments for the explorative analysis of group-wise longitudinal changes, and for the robust and precise quantification of subject-specific regional atrophy rates.

We propose in chapter 5 a generative framework based on the robust and consistent registration of time series of MRI to define subject specific deformation trends, which are then parallel transported in a reference template space to compute groupwise exploratory statistics of longitudinal deformations. This hierarchical formulation is here applied for testing the effects of abnormal CSF $A\beta_{42}$ levels in the structural evolution of the brain in healthy elderly subjects. The method provided a voxel-by-voxel spatio-temporal model of the accelerated atrophy trajectory in subjects positive to $A\beta_{42}$ with respect to the negative ones, which was statistically assessed by multivariate analysis on the trajectory components. The chapter was presented at the 14th International Conference on Medical Image Computing and Computer Assisted Intervention (MICCAI) [Lorenzi et al., 2011a].

After the introduction of the explorative framework for the analysis of groupwise anatomical changes, we focus now on the robust quantification of the regional atrophy. The anatomical quantification of the longitudinal changes in AD is usually performed in selected apriori regions where the pathology is known and which are easier to identify (for instance hippocampus and ventricles). In chapter 6 we propose a novel approach for the atrophy assessment with a more complete, but yet statistically powered, description of the longitudinal changes. The approach *unifies explorative longitudinal analysis and robust atrophy quantification*. The pressure potential associated to the irrotational component of the SVF describing the longitudinal AD trajectory is used to discover the sinks and sources of the atrophy process, which represent respectively the areas of maximal matter loss and CSF expansion. These areas provide a data driven atlas of the AD evolution, that we used for the subject-specific probabilistic analysis of the longitudinal atrophy. The chapter was accepted as an oral communication at the 15th International Conference on Medical Image Computing and Computer Assisted Intervention (MICCAI) [Lorenzi et al., 2012d].

After showing how to estimate powered atrophy measurements on regions identified by the pressure potential, in chapter 7 we define an effective pipeline for validating the proposed method against state-of-art methods for the longitudinal measurements of hippocampal atrophy and ventricular enlargement. Differently from the previuos section, the atrophy is here quantified on apriori regions. The proposed pipeline provides biologically plausible atrophy measures which are consistent in time, and statistically powered. The pipeline was employed for the MICCAI challenge “Atrophy measurement biomarkers using structural MRI for Alzheimer’s disease: a challenge to assess measurement reliability and bias 2012” [Lorenzi et al., 2012a].

Finally, in chapter 8 we provide a glimps of the potential of the longitudinal modeling in understanding the dynamics of pathologies and highlight new research direction. We propose here to analyse the brain atrophy in AD by modeling the anatomical changes as the contribution of an healthy aging component plus a pathological one which is AD specific. This is achieved by projecting the observed brain anatomy on the trajectory of healthy aging modeled with the instruments presented in the previous sections. The experimental results show that AD is characterized by accelerated aging plus specific atrophy changes which are highly discriminative from the healthy condition. This chapter was presented at the MICCAI Workshop on Novel Imaging Biomarkers for Alzheimer's Disease and Related Disorders 2012 [Lorenzi et al., 2012e].

1.4 List of Publications and Awards

Journal articles

- [Lorenzi et al., 2012b] M. Lorenzi, N. Ayache, X. Pennec. LCC-Demons: a robust and accurate diffeomorphic registration algorithm. *Submitted to NeuroImage.* Chapter 2.

- [Lorenzi et al., 2011b] M. Lorenzi, N. Ayache, X. Pennec. Parallel transport of deformations in time series of images: Schild's and Pole ladders. *to be submitted.* Chapter 3.

- [Lorenzi and Pennec, 2012] M. Lorenzi, X. Pennec. Geodesics, parallel transport & one-parameter subgroups for diffeomorphic image registration. *to appear in International Journal of Computer Vision.* Chapter 4.

- [Lorenzi et al., 2010c] M. Lorenzi, N. Donohue, D. Paternicò, C. Scarpazza, S. Ostrowitzki, O. Blin, E. Irving, G.B. Frisoni. Enrichment through biomarkers in clinical trials of Alzheimer's drugs in patients with mild cognitive impairment. *Neurobiology of Aging, 31(8), 1443-1451, 2010.* Summarized in Appendix C.

- R. Rossi, M. Pievani, **M. Lorenzi**, M. Boccardi, R. Beneduce, S. Bignotti, G. Borsci, M. Cotelli, P. Giannakopoulos, L.R. Magni, L. Rillosi, S. Rosini, G. Rossi, G.B. Frisoni. Structural brain features of borderline personality and bipolar disorders. *Psychiatry Research: Neuroimaging, in Press, 2012.*

Selective Peer-Reviewed Conference Papers

- [Lorenzi et al., 2011b] M. Lorenzi, N. Ayache, X. Pennec. Schild's Ladder for the parallel transport of deformations in time series of images *Proceedings in Information Processing on Medical Imaging - IPMI*, 463–474, 2011 (Oral podium presentation, acceptance Rate: 24 out of 800 papers submitted =3%). Chapter 3.

- [Lorenzi et al., 2011a] M. Lorenzi, N. Ayache, G.B. Frisoni, X. Pennec. Mapping the effects of Aβ_{1-42} levels on the longitudinal changes in healthy aging: hierarchical modeling based on stationary velocity fields *Proceedings in Medical Image Computing and Computer Assisted Intervention - MICCAI*, 663–670, 2011 (Acceptance rate: 252 out of 781 papers = 32.3%). Chapter 5.

- [Lorenzi et al., 2012d] M. Lorenzi, N. Ayache, X. Pennec. Regional flux analysis of longitudinal atrophy in Alzheimer's disease. *Proceedings in Medical Image Computing and Computer Assisted Intervention - MICCAI*, 2012 (Oral podium presentation, acceptance rate: 37 out of 781 papers submitted = 4.7%). Chapter 6.

Workshop Papers

- [Lorenzi et al., 2012e] M. Lorenzi, N. Ayache, X. Pennec, G.B. Frisoni. Disentangling the normal aging from the pathological Alzheimer's disease progression on cross-sectional structural MR images. *NIBAD Workshop - MICCAI*, 2012. Oral podium presentation. Chapter 8.
- [Lorenzi et al., 2012a] M. Lorenzi, G.B. frisoni, N. Ayache, X. Pennec. Probabilistic flux analysis of cerebral longitudinal atrophy. *Atrophy measurement biomarkers using structural MRI for Alzheimer's disease: a challenge to assess measurement reliability and bias - NIBAD workshop - MICCAI*, 2012. Oral podium presentation. Chapter 7.
- [Lorenzi and Pennec, 2011] M. Lorenzi, X. Pennec. Geodesics, parallel transport & one-parameter subgroups for diffeomorphic image registration. *Mathematical Foundation of Computational Anatomy Workshop* - MICCAI, 2011. Oral podium presentation. Extended version in Chapter 4.
- [Lorenzi et al., 2010b] M. Lorenzi, N. Ayache, G.B. Frisoni, X. Pennec. 4D registration of serial brain's MR images: a robust measure of changes applied to Alzheimer's disease. *Spatio-Temporal Image Analysis (STIA) workshop, MICCAI*, 2010. Oral podium presentation and best presentation award. Summarized in Appendix A.

Oral Podium Presentations in Clinical Conferences

- M. Lorenzi, N. Ayache, X. Pennec, G.B. Frisoni. Disentangling the normal aging from the pathological Alzheimer's disease progression on cross-sectional structural MR images. *Virtual Physiological Human Conference, London*, 2012. Based on [Lorenzi et al., 2012e].
- M. Lorenzi, N. Ayache, X. Pennec, G.B. Frisoni. Disentangling the normal aging from the pathological Alzheimer's disease progression on cross-sectional structural MR images. *International Conference on Clinical Trials on Alzheimer's Disease (CTAD), Monaco*, 2012. Based on [Lorenzi et al., 2012e].
- M. Lorenzi, N. Donohue, D. Paternicò, C. Scarpazza, S. Ostrowitzki, O. Blin, E. Irving, G.B. Frisoni. Enrichment through biomarkers in clinical trials of Alzheimer's drugs in patients with mild cognitive impairment. *International Conference on Clinical Trials on Alzheimer's Disease (CTAD), Toulouse*, 2010. Based on [Lorenzi et al., 2010c]. Summarized in Appendix C.

Conference Abstracts

- M. Lorenzi, N. Ayache, X. Pennec, and G.B. Frisoni. Effects of abnormal CSF Aβ42 values on the longitudinal atrophy in healthy elders. 12th International Stockholm/Springfield Sympoisium on Advances in Alzheimer Therapy, Stockholm, 2012.

- M. Lorenzi, N. Ayache, X. Pennec, and G.B. Frisoni. Modeling the longitudinal atrophy in healthy subject at risk for Alzheimer's disease. Alzheimer's Association International Conference on Alzheimer's Disease (AAICAD), Vancouver, 2012.

- M. Lorenzi, N. Ayache, X. Pennec, and G.B. Frisoni. Spatio-temporal model of the atrophy progression in subject at risk for Alzheimer's disease. Alzheimer's Association International Conference on Alzheimer's Disease (AAICAD), Vancouver, 2012.

- M. Lorenzi, X. Pennec, and G.B. Frisoni. Monitoring the brain's longitudinal changes in clinical trials for Alzheimers disease: a robust and reliable non-rigid registration framework. Alzheimer's Association International Conference on Alzheimer's Disease (AAICAD), Paris, 2011.

- M. Lorenzi, G.B. Frisoni, N. Ayache and X. Pennec. Mapping longitudinal changes in the brain affected by Alzheimer's disease. Virtual Physiological Human Conference, Brussels, 2010.

- M. Lorenzi and G.B. Frisoni. Voxel-based longitudinal changes of gray matter density in incipient Alzheimer's Disease. Organization for Human Brain Mapping, Barcelona, 2010.

Awards and Invitations

- The paper "Schild's Ladder for the parallel transport of deformations in time series of images" was awarded the Honorable Mention (runner-up) for the Erbsmann Award. The prize awards the best oral presentations (and answer to unlimited questions) of first-time IPMI presenters.

- Invitation to submit a significantly extended and augmented version of the MICCAI workshop paper "Geodesics, parallel transport & one-parameter subgroups for diffeomorphic image registration" to the International Journal of Computer Vision.

- Best oral presentation award of the STIA MICCAI workshop for "4D registration of serial brain's MR images: a robust measure of changes applied to Alzheimer's disease".

- The abstract "Spatio-temporal model of the atrophy progression in subject at risk for Alzheimer's disease" received the travel fellowship for the participation to the Alzheimer's Association International Conference (AAIC), Vancouver, 2012.

- Invited speaker at the Workshop on Shape and Size in Medicine, helded by the Department of Mathematics of the Univerity of Milan, Italy, 2011 (https://sites.google.com/site/shapemilan/).
- Invited speaker at the Workshop on Geometry and Statistics in Bioimaging: Manifolds and Stratified Spaces, helded by the Center for Stochatic Geometry and Advanced Bioimaging, Snderborg, Denmark, 2012 (http://csgb.dk/activities/2012/geostat/programme/).

Part I

Theory & Algorithms for Evaluating and Analyzing the Morphological changes in MRIs

Chapter 2

A Stable and Robust Framework for Measuring Morphological Changes Through Non-rigid Registration.

Contents

This chapter has been submitted as a journal article to NeuroImage. It describes the LCC-Demons framework, and shows that it is an efficient and robust non-rigid registration algorithm for general medical images, and in particular for the spatially consistent measurement of anatomical changes. The framework is tested on synthetic and real data, in both inter- and intra-subject registration setting.

Non-rigid registration is a key instrument for computational anatomy to study the morphology of organs and tissues. However, in order to be an effective instrument for the clinical practice, registration algorithms must be computationally efficient, accurate and most importantly robust to the multiple biases affecting medical images. In this work we propose a fast and robust registration framework based on the log-Demons diffeomorphic registration algorithm. The transformation is parameterized by stationary velocity fields (SVFs), and the similarity metric implements a symmetric *local correlation coefficient (LCC). Moreover, we show how the SVF setting provides a stable and consistent numerical scheme for the computation of the Jacobian determinant and the flux of the deformation across the boundaries of a given region. Thus, it provides a robust evaluation of spatial changes. We tested the LCC-Demons in the* inter-subject *registration setting, by comparing with state of art registration algorithms on public available datasets, and in the* intra-subject *longitudinal registration problem, for the statistically powered measurements of the longitudinal atrophy in Alzheimer's disease. Experimental results show that LCC-Demons is a generic, flexible, efficient and robust algorithm for the accurate non-rigid registration of images, which can find several applications in the field of medical imaging. Without any additional optimization, it solves equally well intra & inter-subject registration problems, and compares favorably to the state of art methods.*

2.1 Introduction

In the recent past, computational anatomy acquired an increasing weight in the analysis of medical data and several methods have been developed to study organs in the *cross-sectional* and *longitudinal* settings. The cross-sectional approach evaluates the geometrical differences between subjects and highlights the morphological differences between clinical groups. The longitudinal perspective evaluates the changes in time from serial data of the same subject acting as his own control, and is more useful in detecting the subtle changes related to biological processes.

The key instrument of computational anatomy is non-rigid registration, which allows to retrieve morphological differences as deformation fields. A great variety of registration techniques have been proposed in medical imaging, depending on the practical application and the theoretical requirements. However, in order to define a reliable image processing tool, we can identify a set of requirements to be satisfied: robustness to bias, theoretical solidity coupled with numerical efficiency, and consistency of the anatomical measures.

2.1.1 Similarity Measures to Robustly Detect the Anatomical Differences

In non-rigid registration the deformation is found by optimizing a similarity measure which quantifies the amount of differences between two images. Thus, the quality of the retrieved deformations greatly depends on the choice of this metric. A classical similarity measure is the sum of squared differences of the intensities, which is completely driven by the global intensity differences [Bajcsy et al., 1993, Stefanescu, 2005]. Despite the simple numerical implementation, this metric is highly sensitive to the intensity biases which affect the medical images. For this reason, more complex similarity criterion able to account for the bias have been proposed. For instance the (normalized) correlation criteria assumes a global affine relationship between the intensities in the images, to account for global multiplicative and additive bias [Dong and Boyer, 1995, Collins et al., 1995], while the (normalized) mutual information does not require any parametric assumption on the relationship between the intensities, and is based on the global joint intensity histogram [Wells et al., 1996, Studholme et al., 1996, Maes et al., 1997]. The robustness of NMI comes at the price of the computation of the histogram, and thus of complex optimization schemes.

Importantly, all the above criteria are global, i.e. they assume a uniform bias distribution over the image space. However in the medical images the bias is frequently locally varying, and in this case a global similarity measure might lead to wrong estimations of the deformations. By assuming that the information in the image is locally sufficient to estimate the intensity bias, in [Cachier and Pennec, 2000, Cachier et al., 2003] the authors proposed a local implementation of the correlation criteria. Interestingly, such a framework led to an efficient optimization scheme based on Gaussian convolutions and computed through the classical Demons registration close form solution.

The local correlation coefficient (or local cross correlation) was later used in several successful registration algorithms as a good trade-off between the very constrained SSD and the very loose Mutual Information [Hermosillo and Faugeras, 2004, Jolly et al., 2010, Avants et al., 2008].

2.1.2 Diffeomorphic Registration: Mathematical Formulation and Numerical Efficiency

The new-generation non-rigid registration algorithms perform diffeomorphic registration by parameterizing the deformations by the flow of time varying or stationary tangent velocity fields. The use of diffeomorphisms provides a rich mathematical setting for elegant and grounded methods for atlas building [Joshi et al., 2004a], group-wise [Bossa et al., 2007], and longitudinal statistical analysis of deformations [Avants et al., 2007, Lorenzi et al., 2011a, Davis et al., 2007, Durrleman et al., 2012].

Diffeomorphic registration was introduced with the large deformation diffeomorphic metric mapping setting (LDDMM) [Trouvé, 1998], which parameterizes the deformations with *time varying* velocity fields, and in [Avants et al., 2008] a robust implementation of the LDDMM based on the local cross correlation criteria was proposed. However, the LDDMM has high computational cost which might prevent the intensive application on large dataset, or on high resolution data.

In order to find an optimal compromise between accuracy and computational efficiency, it was proposed in [Arsigny et al., 2006] to parameterize diffeomorphic transformations with *stationary velocity fields* (SVF). The framework was used in different registration settings [Vercauteren et al., 2008, Bossa et al., 2007, Ashburner, 2007a, Modat et al., 2011], and was applied to several clinical problems [Sweet and Pennec, 2010, Mansi et al., 2011a, Lorenzi et al., 2011a, Seiler et al., 2011a, McLeod et al., 2012, Siless et al., 2012]. In light of these results, the SVF registration might represent a powerful clinical instrument for the evaluation of the morphological changes in organs, due to its high flexibility and efficiency. However, most of the standard SVF based algorithms such as the log-Demons [Vercauteren et al., 2008] are based on the sum of squared differences criteria (SSD), which is not robust to the intensity bias affecting the medical images and might limit the applicability of such a framework in the clinical context.

2.1.3 Consistet Measures of Spatial Changes from Local to Regional Scale

In order to provide a useful measure of anatomical changes for clinically oriented applications, a registration framework should be able to consistently quantify the changes at different spatial scales.

Classically, non-rigid registration was used to provide *local* measures of change at the finer scale (voxels, meshes) to be used in group-wise statistical analyses of morphological differences. Among the many techniques we can find the voxel compression maps (VCM) [Fox et al., 2001], the voxel/tensor-based morphometry based on the Jacobian determinant of the deformation (VBM,TBM) [Ashburner and Friston, 2000, Riddle et al., 2004], the RAVENS maps [Resnik et al., 2000], and the cortical pattern analysis [Thompson et al., 2003]. However, measures at the voxel level are sensitive to biases and very variable across subjects.

For this reason, *global* measures of regional changes are more commonly used in clinical practice, to quantify regional volumes on selected anatomical structures. These measures are usually quantified by segmentation: for instance, the boundary shift of anatomical regions [FreeBorough and Fox, 1997] is currently used to evaluate the longitudinal volume changes in time series of images [Leung et al., 2009] .

Global measures of average volume change can be estimated from local measures by integration of the Jacobian determinant of the deformation in selected regions [Boyes et al., 2006, Camara et al., 2008]. However, the local measure of volume change given by the Jacobian determinant represents only part of the information represented by the vector field. More importantly, the computation of the Jacobian matrix requires the computation of the image derivatives which are practically computed by finite differences on the image grid, and which are highly sensitive to the approximation introduced by the discretization. Finally, experimental evidence showed that the logarithmic transformation of the Jacobian determinant might be more appropriated in morphometric studies, since it provides non-skewed quantities [Leow et al., 2007]. As a drawback, the log-Jacobian determinant does not represent anymore the volume change, and thus lacks of a precise biological interpretation.

Other quantifications of spatial changes might be then considered: as suggested in [Chung et al., 2001], the flux of the deformation across the boundary of a region is a measure of global morphological change that can be used for growth and longitudinal volume change analyses. However, since the flux requires the computation of the vector's normal to the surface, the use of this measure was very limited in the past due to the high sensitivity to segmentation errors.

2.1.4 Paper Organization

The aim of the present work is to propose an effective *symmetric diffeomorphic* registration framework based on SVFs, which could be at the same time *robust* to the intensity biases and *numerically efficient*. Such a framework should provide *consistent measures* of spatial changes from the local to the regional level, which require *numerically stable* methods to compute the Jacobian determinant and the flux of the deformation across surfaces.

In Section 2.2 we introduce the symmetric LCC-Demons, a registration framework based on the log-Demons which implements the symmetric local Correlation Criteria (LCC) as a similarity measure. In Section 2.3 we derive from the resulting SVF a spatially robust and consistent evaluation of the morphological changes from the voxel to the regional level. In fact we show that the SVF framework provides both stable voxel-by-voxel estimations of the Jacobian determinant, and consistent measures of regional changes given by the flux of the deformation across surfaces, which is obtained by the integration of the log-Jacobian determinant. The presented method is validated in section 2.4.3 by comparing our algorithm with state of the art registration algorithms for the accuracy in inter-subject registration, and in section 2.5 for the longitudinal atrophy measurements in Alzheimer's disease. The resulting longitudinal atrophy measures are compared to the ones obtained by the BSI algorithm [FreeBorough and Fox, 1997], a validated measure of brain atrophy currently employed in the clinical setting.

2.2 LCC-Demons: Symmetric Unbiased Diffeomorphic Registration

2.2.1 The log-Demons Algorithm: a Brief Review.

The log-Demons algorithm estimates the diffeomorphic transformation ϕ which minimizes the intensity difference between a fixed image I and a moving image J [Vercauteren et al., 2008]. The deformation ϕ belongs to the subset of diffeomorphisms generated by the flow of SVFs. Such a deformation is parameterized through the Lie group exponential of a SVF $\mathbf{v}$, $\exp(\mathbf{v})$, defined by:

$$\frac{\partial\phi(x,t)}{\partial t} = \mathbf{v}(\phi(x,t)), \tag{2.1}$$

with initial condition $\phi(x,0) = id$. This ODE actually defines a one parameter subgroup, $\phi_t(x) = \phi(x,t)$ since $\phi_{s+t}(x) = \phi(x,s)\circ\phi(x,t) = \phi(x,s+t)$. The transformation is obtained at the parameter value $t = 1$, i.e. $\phi(x) = \phi(x,1)$. The use of SVFs simplifies the LDDMM formulation and leads to a good compromise between theory and efficiency for computationally tractable registrations. For example, the exponential operation is efficiently implemented in the log-Demon's algorithm by taking advantage of the "scaling and squaring" property of the one-parameter subgroups $\exp(\mathbf{v}) = \exp(\mathbf{v}/2)\circ\exp(\mathbf{v}/2)$ [Arsigny et al., 2006]. This allows to compute the final parameterization as the recursive composition of successive exponentials (Algorithm 1).

Algorithm 1 Scaling and Squaring for the Lie group exponential.

```
1. Scaling step.
   Choose $N$ so that $2^{-N}\mathbf{v}$ is "small".
2. Compute a first approximation of $\phi_0 \leftarrow exp(2^{-N}\mathbf{v}) \approx id + 2^{-N}\mathbf{v}$
3. Squaring step.
   For $k = 1$ to $N$ do $\phi_k \leftarrow \phi_{k-1}\circ\phi_{k-1}$
```

In the log-Demons framework the registration of the images F and G is achieved through the alternate minimization of the following energy, which is optimized with respect to the transformation SVF $\mathbf{v}$, and to the auxiliary correspondence field parameterized by a SVF $\mathbf{v_x}$ [Vercauteren et al., 2008]:

$$\begin{aligned} E(\mathbf{v},\mathbf{v_x},I,J) = {} & \frac{1}{\sigma_i^2}\|F - G\circ\exp(\mathbf{v_x})\|^2_{L_2} \\ & + \frac{1}{\sigma_x^2}\|\log(\exp(-\mathbf{v})\circ\exp(\mathbf{v_x}))\|^2_{L_2} + \frac{1}{\sigma_T^2}\mathrm{Reg}(\mathbf{v}). \end{aligned} \tag{2.2}$$

The coupling term $\frac{1}{\sigma_x^2}\|\log(\exp(-\mathbf{v}) \circ \exp(\mathbf{v_x}))\|_{L_2}^2$ is reformulated thanks to the BCH formula for the composition of exponentials [Bossa et al., 2007]: $\log(\exp(-\mathbf{v}) \circ \exp(\mathbf{v_x})) = BCH(-\mathbf{v}, \mathbf{v_x}) = \delta\mathbf{v}$, and in the log-Demons we usually consider the zeroth order approximation $\delta\mathbf{v} = -\mathbf{v} + \mathbf{v_x}$. The minimization of the above energy is alternatively operated with respect to the two variables $\mathbf{v}$ and $\mathbf{v_x}$ in two steps:

- *Minimization step.* Given $\mathbf{v}$, the energy

$$E^{SSD}(\mathbf{v}, \delta\mathbf{v}, F, G) = \frac{1}{\sigma_i^2}\|F - G \circ \exp(\mathbf{v}) \circ \exp(\delta\mathbf{v})\|_{L_2}^2 + \frac{1}{\sigma_x^2}\|\delta\mathbf{v}\|_{L_2}^2, \qquad (2.3)$$

  is optimized for $\delta\mathbf{v}$, and hence for $\mathbf{v_x} = BCH(\mathbf{v}, \delta\mathbf{v})$ to find an un-regularized correspondence $\mathbf{v_x}$ that matches the images F and G. The Gauss-Newton optimization leads to a closed form solution for the update $\delta\mathbf{v}$, which is then efficiently composed with $\mathbf{v}$ thanks to the BCH formula.

- *Regularisation step.* Given $\mathbf{v_x}$, the functional

$$E\text{reg}(\mathbf{v}, \mathbf{v_x}) \;=\; \frac{1}{\sigma_x^2}\|\exp(-\mathbf{v}) \circ \exp(\mathbf{v_x})\|_{L_2}^2 + \frac{1}{\sigma_T^2}\mathrm{Reg}(\mathbf{v}) \qquad (2.4)$$

  is optimized with respect to $\mathbf{v}$. Following [Mansi et al., 2010], we obtain a closed form by convolution for the regularization step. When the criterion Reg is conveniently chosen, the optimal $\mathbf{v}$ is obtained in the Fourier domain leading to the Gaussian smoothing $\mathbf{v} = G_\sigma * \mathbf{v_x}$. which leads to an elastic-like regularization of the velocity field $\mathbf{v_x}$. In addition to this, the standard log-Demons registration implements also a fluid-like regularization of the update field $G_{\sigma_f} * \delta v$, which corresponds to choice of a convenient metric on the space of SVFs.

2.2.2 Symmetric Forces in the log-Demons

In the log-Demons algorithm the correspondence $\mathbf{v_x}$ is unbiased with respect to the choice of fixed and moving image. In fact it is symmetrically computed by minimizing the energy $E_{sym}^{old} = \frac{1}{2}\|F - G \circ \exp(\mathbf{v})\|^2 + \|F \circ \exp(-\mathbf{v}) - G\|^2$. The symmetrization comes straightforwardly from the SVF parameterization of the deformations, and is optimized by averaging the solutions given by the two separate terms. However the strategy requires the separated optimization of both correspondence terms, and might be computationally costly in case of similarity terms more complex than the standard SSD implemented in the log-Demons.

In this paper we propose to symmetrize a given criteria by optimizing in the half-way space, reached by resampling both fixed and moving images. This can be easily formulated within the SVF framework by considering $F \circ \exp(-\frac{\mathbf{v}}{2})$ and $G \circ \exp(\frac{\mathbf{v}}{2})$.

For instance, the classic SSD criteria can be symmetrized in:

$$E^{SSD}_{sym}(\mathbf{v}, F, G) \quad = \|F \circ \exp(-\tfrac{\mathbf{v}}{2}) - G \circ \exp(\tfrac{\mathbf{v}}{2})\|^2_{L_2}.$$

In this case, the Jacobian of the criteria is

$$\mathbf{J} = \frac{1}{2}\left(\nabla F \circ \exp(-\frac{\mathbf{v}}{2}) + \nabla G \circ \exp(\frac{\mathbf{v}}{2})\right),$$

which interestingly is consistent with the one derived for the Demons symmetric update rule proposed in [Vercauteren, 2008].

2.2.3 Symmetric LCC in the log-Demons

In the standard log-Demons algorithm the correspondence field is given by the minimization of the sum of squared difference (SSD) between the intensities of the two images, which is not robust to the local intensity biases. In order to avoid mistaking spurious intensity variations for morphological differences, following [Cachier et al., 2003] we propose to adapt to the log-Demons framework to the local correlation coefficient (LCC). Let $\overline{F} = \int_\Omega \mathbf{G}_\sigma * F_0(x)\, dx$ be the local mean image. The LCC is defined as:

$$\rho(F, G) = \frac{\overline{FG}}{\sqrt{\overline{F^2}\,\overline{G^2}}}.$$

Let consider the symmetric resampling $F' = F \circ \exp(-\frac{\mathbf{v}}{2})$ and $G' = G \circ \exp(\frac{\mathbf{v}}{2})$, and denote

$$\rho(\mathbf{v}, F, G) = \rho(F', G') = \frac{\overline{F \circ \exp\left(-\frac{\mathbf{v}}{2}\right) G \circ \exp\left(\frac{\mathbf{v}}{2}\right)}}{\sqrt{\overline{\left[F \circ \exp\left(-\frac{\mathbf{v}}{2}\right)\right]^2}\;\overline{\left[G \circ \exp\left(\frac{\mathbf{v}}{2}\right)\right]^2}}}.$$

If we replace the SSD in formula (2.3) by the squared LCC, we obtain the new correspondence energy

$$E^{LCC}_{sym}(\delta\mathbf{v}, F', G') = \frac{1}{\sigma_i^2}\rho^2(\delta\mathbf{v}, F', G') + \frac{1}{\sigma_x^2}\|\delta\mathbf{v}\|^2_{L_2}. \tag{2.5}$$

It can be shown (see 2.A) that the optimization of (2.5) with respect to a symmetric update of F' and G' can be computed with a closed form formula:

$$\delta\mathbf{v} = -\frac{2\Lambda}{\|\Lambda\|^2 + \frac{4}{\rho^2}\frac{\sigma_i^2}{\sigma_x^2}}.$$

This way the original log-Demons structure and efficiency are preserved.

2.3 Stable and Consistent Measures of Brain Changes: from Voxel to Regional Level

The quantification of the amount of warping ϕ applied at each voxel by the dense deformation field is usually locally derived from the Jacobian matrix $\mathbf{J} = \nabla\phi$ of the deformation in terms of determinant, log-determinant, trace, and the strain tensor $\mathbf{J}\mathbf{J}^T$. A global index of change can be extracted from the local information by:

- Integration of the Jacobian Determinant on the region of interest. This is an average measure of *volume change*.
- Evaluation of the flux of the deformation field across the surface enclosing the region, i.e. the amount of vectors flowing through the surface during the registration procedure. This value represents the *shift of the boundaries* of the surface required to match the homologous points during the registration process.

If the flux on a specific surface area is known, we can derive the ratio of volume change by comparing the volume enclosed by the shifted surface relative to the original one. However, the direct computation of the flux of a deformation is usually highly sensitive to the segmentation of the boundaries of the surface. This limitation prevented the use of the vector flux in favour of the more robust Jacobian determinant integration, while surrogate measures of the boundary shift were proposed based on the comparison of regional segmentations [FreeBorough and Fox, 1997, Smith et al., 2002].

2.3.1 Flux Across Surfaces From the log-Jacobian Integration

We now build on [Mansi et al., 2010] to show how to consistently derive local and global anatomical measures within the log-Demons framework. From the formula (2.1), the instantaneous variation of the Jacobian determinant of the deformation can be expressed as:

$$\frac{\partial \det(\nabla\phi(x,t))}{\partial t} = \det(\nabla\phi(x,t))\,\mathrm{tr}\left(\nabla\phi(x,t)^{-1}\frac{\partial(\nabla\phi(x,t))}{\partial t}\right).$$

By inverting the order of temporal and spatial derivatives within the trace, and by applying the chain rule we get [Mansi et al., 2010]:

$$\frac{\partial \det(\nabla\phi(x,t))}{\partial t} = \det(\nabla\phi(x,t))\,(\nabla.\mathbf{v}(x)\circ\phi(x,t)).$$

Now, given that $\phi(x,0) = \mathrm{id}$, we have $\log(\det(\nabla\phi(x,0))) = 0$, and we obtain the solution $\log(\det(\nabla\phi(x,t))) = \int_0^t \nabla\cdot\mathbf{v}|_{\phi(x,h)}\,dh$. In particular,

$$\log(\det(\nabla\phi(x,1))) = \int_0^1 \nabla\cdot\mathbf{v}|_{\phi(x,h)}\,dh. \tag{2.6}$$

The above formula states that, under the log-Demons framework, the log-Jacobian determinant of $\phi(x) = \phi(x,1)$ is the integral of the divergence of the velocity field along the path described by the exponential.
Assuming now that Ω is a volume in the domain of the vector field $\phi(x)$, we can integrate (2.6) to obtain:

$$\iiint_\Omega \log(\det(\nabla\phi(x,1)))d\Omega \;=\; \int_0^1 \left(\iiint_\Omega \nabla\cdot\mathbf{v}|_{\phi(x,h)}\, d\Omega\right) dh. \tag{2.7}$$

We recall now the Divergence (or Ostrogradsky's) theorem, which states that for a volume Ω immersed in a vector field $\mathbf{v}$ the following relationship holds:

$$\iiint_\Omega (\nabla\cdot\mathbf{v})\, d\Omega \;=\; \oint_{\partial\Omega} \mathbf{v}\cdot\boldsymbol{n}\, d\partial\Omega,$$

where the second part of the equality represents the flux of the vector fields through the surface $\partial\Omega$. Applying the Divergence Theorem to (2.7) finally gives:

$$\iiint_\Omega \log(\det(\nabla\phi(x,1)))d\Omega \;=\; \int_0^1 \mathrm{flux}_{\partial\Omega}(\mathbf{v}|_{\phi(x,h)})\, dh \tag{2.8}$$

Thus, the integration over the volume of interest of the log-Jacobian determinant of the deformation is equivalent to integrating the flux of the velocity field across the corresponding surface, along the path described by the exponential map.

Formula (2.8) consistently computes the flow of the vector field during the evolution described by the SVF parameterization, and measures the flux of a vector field over a surface (right side of (2.8)) by scalar integration of the log-Jacobian determinant in the enclosed volume (left side of (2.8)). Moving from the surface to the volume integration simplifies and robustifies the measure of the flux by attenuating the segmentation errors (and relative erroneous boundary detection), and allows to deal with uncertainties in the measures, for instance by integration on probabilistic masks. The difference between the Jacobian and the log-Jacobian analysis becomes clear: the former quantifies the volume changes, while the latter the shift of the boundaries (given by the average regional log-Jacobian determinant).

2.3.2 A New Numerical Scheme for Computing the Jacobian

The computation of the Jacobian determinant $\|\nabla\phi\|$ is usually performed by spatial differentiation of the transformation using finite differences (Algorithm 2).

However, the differentiation by finite differences is usually highly sensitive to the spatial noise, and completely depends on the discrete sampling which might create instabilities in case of large deformations, thus leading to incorrect Jacobian determinant estimation. For instance the sampling of the deformation field in the image grid space might introduce an unequal distribution of the vectors around a sink, and therefore introduce spurious folding effects to finally produce negative Jacobian estimations.

Algorithm 2 Classical computation of the Jacobian determinant by finite differences.

```
Given a discrete sampling $\phi$ of the transformation over the
image grid space $\{x_i\}$:
  1. Compute the Jacobian matrix J via finite differences, for instance
     with the forward scheme:
     $J^{\phi}_{k,l}(x) = \frac{\phi_k(x+h\mathbf{e}^l)-\phi_k(x)}{h}$, $h$ scalar.
  2. Compute the determinant of J with the preferred numerical method.
```

The following framework provides a stable and consistent computation of the Jacobian determinant according to the scaling and squaring method for the Lie group exponential. In fact, the (log-)Jacobian can be reliably estimated by finite differences on the *scaled* velocity field $\frac{\mathbf{v}}{2^N}$, and then recursively computed by the chain rule combined to the additive property of the one-parameter subgroups (Algorithm 3).

Algorithm 3 Log-Jacobian determinant by scaling and squaring.

```
Given a deformation $\phi = \exp(\mathbf{v})$ :
  1. Scaling step.
     Choose $N$ so that $2^{-N}\mathbf{v}$ is ”small“
  2. Compute a first approximation:
     $\phi_0 = \exp(2^{-N}\mathbf{v}) \approx id + 2^{-N}\mathbf{v}$ .
     $LJ_0 = \log\left(J(\phi_0)\right)$
         $\approx \log\left(1 + \nabla \cdot (\frac{\mathbf{v}}{2^N})\right) \approx \nabla \cdot (\frac{\mathbf{v}}{2^N})$.
  3. Squaring step.
     For $k = 1$ to $N$ do
     $\phi_k = \phi_{k-1} \circ \phi_{k-1}$,
     $LJ_k = \log(J(\phi_k)) = LJ_{k-1} \circ \phi_{k-1} + LJ_{k-1}$.
```

The presented scheme evaluates the Jacobian determinant accordingly to the exponential path and is consistent with the definition of diffeomorphisms parameterized by the one-parameter subgroup. Moreover, the log-Jacobian determinant is defined in terms of the divergence of the velocity and, by definition, the value of the corresponding Jacobian determinant always remains strictly positive.

2.4 Experiments

2.4.1 Jacobian Determinant: Scaling and Squaring vs Finite Differences

We consider here a practical example with a pair of longitudinal brain images from the ADNI dataset. As can be seen in the detail of Figure 2.1, even after bias

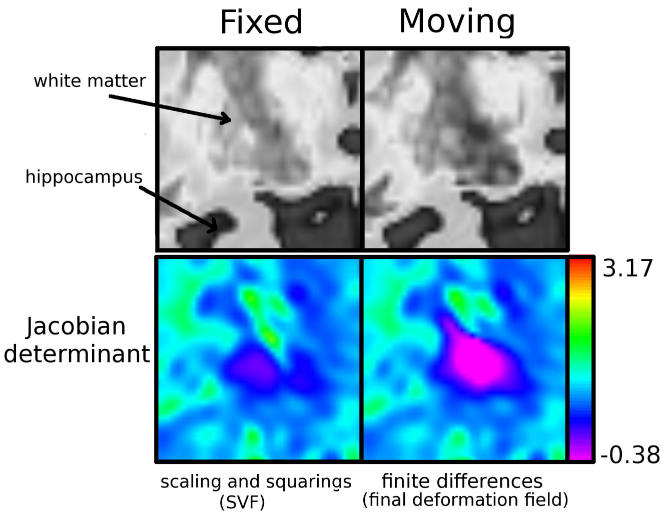

Figure 2.1: Jacobian determinant computation in the SVF setting. Upper row: detail from a pair of anatomical fixed and moving brain images. The SSD criteria of the log-Demons models the general increase of the intensities by estimating a contracting deformation field from the boundaries to the center of the image. Bottom row: corresponding Jacobian determinant maps estimated by the iterative scaling and squaring formula on the SVF (left), and by the standard finite differences on the final deformation field (right). The finite differences lead to negative values for the Jacobian determinant.

correction [Tustison et al., 2010] and histogram equalization, a persistent difference between the two images on the white matter intensities is still appreciable. The intensity shift in the white matter is detected by the SSD criteria of the log-Demons as an anatomical difference which generates a sink at the center of the area. This highly localized large deformation leads finally to negative Jacobian determinants when estimated with the standard finite differences. On the contrary, the Jacobian determinant computed by scaling and squaring is always positive and thus consistent with the log-Demons diffeomorphic transformation.

2.4.2 Robustness to the Intensity Bias: a Controlled Example

We first tested the robustness of the LCC-Demons to the intensity biases on a controlled experiment. We created a realistic simulated anatomical deformation based on the deformation field that matched the baseline scan (I_0) of a patient to its 1-year follow-up of, computed using the log-Demons algorithm. The ventricular expansion was extracted by masking the corresponding SVF $\mathbf{v}$ with a cubic box enclosing the ventricles. The deformations in the remaining areas of the brain were imposed to be negligible random noise. The resulting deformation field $\varphi = \mathrm{Exp}(\mathbf{v})$ was used to warp the baseline scan I_0 to generate the longitudinal image with

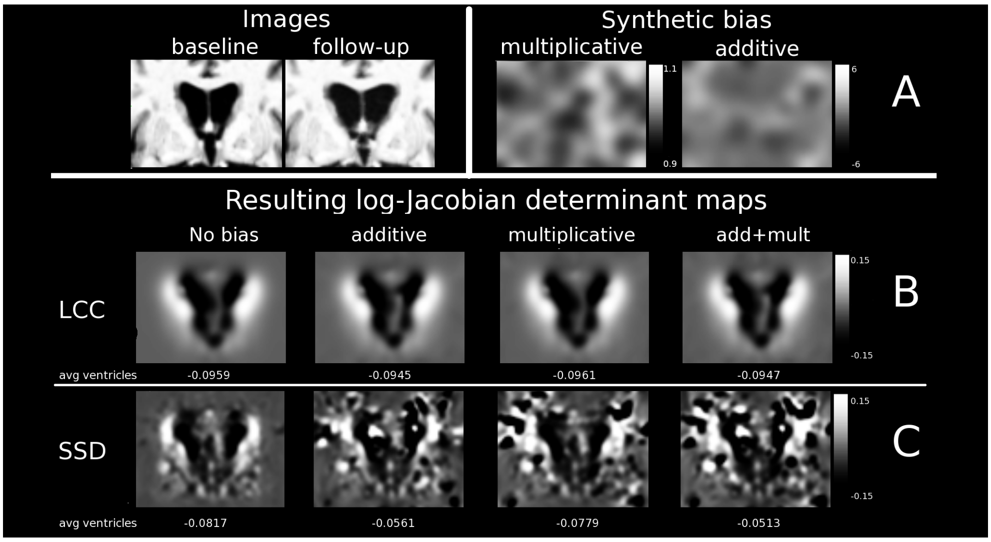

Figure 2.2: Synthetic experiment. A) Left: baseline and simulated follow-up ventricles expansion. Right: synthetic additive and multiplicative bias. Bottom rows: bias effect on the log-Jacobian determinant maps for the deformations estimated by the Demons algorithm with B) LCC and C) SSD similarity criteria. The LCC estimation remains consistent independently from the biases introduced.

increased ventricular expansions. This pair of images was then used as reference to test the robustness of the detection of the longitudinal changes in the ventricular reference region to the bias.

For this purpose, the intensities of the follow-up image were corrupted by introducing spatially smooth random additive (±5% of the mean baseline intensities) and multiplicative noise (range [0.9-1.1]). The changes between baseline and generated follow-up were evaluated with the LCC-Demons and the standard log-Demons as average log-Jacobian determinant values measured in the ventricles mask. The regularization parameters were set for both methods as $\sigma_{fluid} = 0.5$, and $\sigma_{elastic} = 1.5$, while the LCC smoothing parameters was $\sigma_{LCC} = 2$. An histogram matching of the image intensities was applied prior to the standard log-Demons registration.

As can be seen in Figure 2.2, the LCC-Demons estimation remains stable regardless to the level of noise, while the standard log-Demons appears to be highly sensitive. This is reflected by the regional integration of the log-Jacobian map in the ventricles mask: the SSD criteria leads to unstable evaluations while the LCC measures remain consistent.

2.4.3 Registration Accuracy: Evaluation on Public Datasets

In [Klein et al., 2009] the authors benchmarked several registration algorithms on a collection of publicly available brain images, to compare the registration performance on the matching of a set of manually labeled anatomical regions. This work represents a valuable source of information for the comparison of new registration methods, since the detailed description of the registration results is freely available[1]. Interestingly, the authors found that the performance of the registration algorithms was little affected by the choice of subject population, labeling protocol, and type of overlap measure.

In order to test the LCC-Demons we replicated the registration pipeline proposed by [Klein et al., 2009] on the data considered by the authors. In particular, the pipeline was defined by non rigid registration of all the possible pairs of linearly aligned images in the dataset, after an initial affine registration to the MNI reference space, and was applied to the CUMC12, MGH10, LPBA40 and IBSR12 datasets. The registration parameters for the LCC-Demons were: $\sigma_{LCC} = 2$, $\sigma_{elastic} = 1.5$ and $\sigma_{fluid} = 0.5$, with a multi resolution scheme of 30x20x10 iterations (coarser to finer).

The registration accuracy between each source S and target T was evaluated by the measures of target and union overlap, defined for a specific anatomical region r respectively as

$$TO_r = \frac{|S_r \cap T_r|}{|T_r|} \quad \text{and} \quad MO_r = \frac{|S_r \cap T_r|}{|S_r| + |T_r|},$$

where $|\cdot|$ is the regional volume.

In Figure 2.4 we can observe the performance on the CUMC12 dataset in terms of resulting mean target overlap on the 130 labeled regions. The results produced by the LCC-Demons registration are in line with those provided by the state-of-art algorithms, and in particular are consistent with the original ones obtained with the classical Demons registration. For instance in the CUMC12 dataset the LCC-Demons perform significantly better than most of the compared methods, except ART, IRTK, SyN, and SPM Dartel. All the reported mean differences were significant to the standard paired t-test. When tested on the other datasets (Figure 2.5, 2.6, and 2.7), the only algorithms that consistently provided better overlaps were ART, IRTK, and SyN.

We stress that the registration test was here blindly performed with default parameters of the LCC-Demons algorithm, without any dataset specific optimization of the parameters.

The average registration time on the tested data was of 21 minutes (± 1.7) on a Xeon platform 2.66Ghz quad core, 4Gb RAM.

2.5 Measuring the Longitudinal Changes in Alzheimer's Disease

2.5.1 Experimental Data.

Data used in the preparation of this article were obtained from the Alzheimer's Disease Neuroimaging Initiative (ADNI) database (adni.loni.ucla.edu). The ADNI was

---

[1] http://www.mindboggle.info/papers/evaluation_NeuroImage2009.php

launched in 2003 by the National Institute on Aging (NIA), the National Institute of Biomedical Imaging and Bioengineering (NIBIB), the Food and Drug Administration (FDA), private pharmaceutical companies and non-profit organizations, as a $60 million, 5-year public-private partnership. The Principal Investigator of this initiative is Michael W. Weiner, MD, VA Medical Center and University of California - San Francisco. ADNI is the result of efforts of many coinvestigators from a broad range of academic institutions and private corporations, and subjects were recruited from over 50 sites across the U.S. and Canada. For up-to-date information, see www.adni-info.org.

2.5.2 Longitudinal Pre-processing and Registration.

The baseline and one year follow-up brain images were collected from the ADNI dataset for a group of 200 healthy subjects and 141 patients affected by Alzheimer's disease. For each subject, the follow-up images were rigidly aligned to the baseline and the longitudinal changes were evaluated by registration with the LCC-Demons algorithm (smoothing sigma for the criteria $\sigma_{LCC} = 2$,$\sigma_{elastic} = 1.5$, and $\sigma_{fluid} = 0.5$).

2.5.3 Mask Definition for Regional Measures.

In standard deformation based morphometry, the amount of regional brain atrophy is usually quantified by the scalar integration of the average Jacobian determinant map on a pre-defined region of interest (ROI). However, depending on the deformation model, the vector field which encodes the transformation can diffuse through the regional boundaries according to the regularization scheme. In this case, the integration of vector-based quantities (like the Jacobian determinant) on anatomical regions might not be consistently defined and might lead to wrong estimations of the anatomical changes. In order to evaluate the anatomical changes consistently with the deformation model, we propose here to adapt the given anatomical region in order to maximise the vector flux across the boundaries. In [Vasilevskiy and Siddiqi, 2002] it was shown that, given a vector field $\mathbf{v}$ and a surface S, the maximal flux of $\mathbf{v}$ across S is obtained by evolving the region along the direction

$$\frac{\partial S}{\partial t} = (\nabla \cdot \mathbf{v})\boldsymbol{n} \tag{2.9}$$

Thus, given an initial brain mask and a longitudinal deformation, we can continuously deform the mask in order to maximise the flux of the longitudinal deformation through its boundaries, i.e. adapt the mask to the areas of significant longitudinal changes.

In our experiments we computed the gray-white matter tissue mask with an automated procedure based on the FSL package tools for the automatic brain extraction and the tissue class segmentation [Smith, 2002, Patenaude et al., 2011]. The estimated mask was then flowed along the longitudinal deformation according to (2.9)

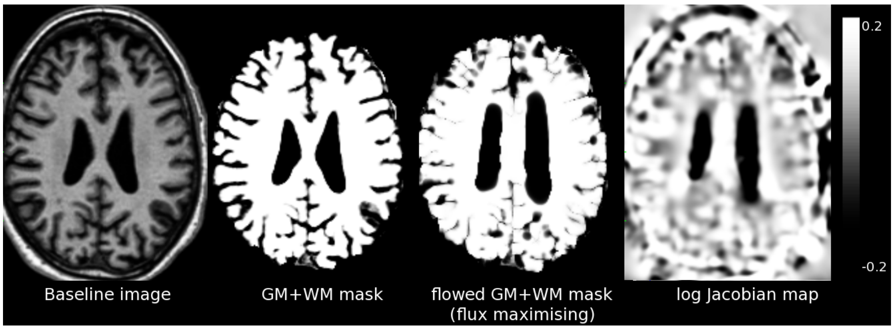

Figure 2.3: Deforming a volumetric mask in order to maximise the flux across the boundaries. From left: reference image, associated brain mask, and the deformed mask which maximises the flux of the longitudinal deformation. The last picture shows the log-Jacobian determinant map of deformation. It can be seen that the deformed mask is adapted to the areas of maximum expansion.

as $M^{i+1} = M^i \circ \frac{\partial S}{\partial t}$ (15 iterations) and then used for the longitudinal quantification (Figure 2.3).

The whole brain changes were defined by the weighted Jacobian determinant, which represents the average volume change within the probabilistic mask, and by the weighted log-Jacobian determinant, which represents the expected flux of the deformation through the region's boundaries. If we approximate the region with a sphere S1 having the same volume, we can compute the *flux-derived volume change* by considering a radial field acting on the sphere S1 and having the same flux. We obtain then a volume change index by comparing the volume of the resulting shifted sphere S2 relatively to S1.

For sake of comparison the measurements were compared to the KNBSI[2] atrophy index [Leung et al., 2009] obtained using our initial brain masks on the same processed data.

2.5.4 Longitudinal Atrophy Estimation.

The average measures for the one-year whole brain changes estimated by the LCC Demons are shown in Table 2.1. The volume changes measured by the Jacobian determinant integration are consistent with those derived from the flux and are respectively of 1.8% per year for the AD group and 1% per year for the healthy subjects. The proposed results are consistent with the KNBSI estimations (last column), obtained on the same data. The sample size analysis provided similar results, with the lowest score given by the flux associated to the deformation (552 subjects). We specify that the KNBSI algorithm was applied here using a different processing protocol than the one proposed in [Leung et al., 2009]. In particular, the affine registration employed here was not symmetric, and there was no manual intervention in

---

[2] KNBSI is available at http://sourceforge.net/projects/bsintegral/

the segmentation of the brain masks. Therefore, the suboptimal processing protocol might explain the worse results in terms of sample size analysis when compared to those reported by the authors. Even though a detailed comparison of the processing procedures is out of the scope of this work, we notice that the methods performed similarly when applied to the same data.

Group	LCC-Demons			KNBSI
	Jacobian	Flux	Flux derived % change	% change
Ctrls	1.011 (0.0102)	0.252 (0.233)	1.09 (1.02)	1.069 (0.925)
AD	1.0186 (0.011)	0.409 (0.239)	1.81 (1.06)	1.714 (0.989)
Sample size (95% CI)	619 (305,1154)	552 (309,1260)	544 (315,1255)	590 (332,1328)

Table 2.1: Longitudinal whole brain changes in Alzheimer's disease and healthy aging measured by the LCC-Demons as the average Jacobian determinant, flux across the surface, and flux derived volume change (standard deviation on parenthesis). Last column: KNBSI atrophy rates obtained on the same data. Bottom row: estimated sample size associated to the measures for detecting a 25% change in the AD trend when controlled to normal aging (80% power, $p<0.05$ [Fox et al., 2000]).

2.6 Conclusions and Perspectives

In this work we proposed an efficient, accurate and robust registration framework for the estimation and quantification of anatomical changes in medical images. We first introduced the LCC-Demons, a diffeomorphic registration algorithm robust to intensity biases, which extends the standard log-Demons algorithm by preserving the simple numerical implementation and the related computational efficiency. Second, we provided a new numerical scheme for the computation of the Jacobian determinant of a deformation parameterized by a stationary velocity field, which prevents the numerical inaccuracies induced by the finite differences, and is consistent with the diffeomorphic parameterization. Finally, we explained the theoretical difference between log-Jacobian and Jacobian analysis of deformation fields, by showing that the surface integral of the flux of a vector field is the regional integration of log-Jacobian determinant associated to the deformations. This contribution shows the complementary information provided by the Jacobian and the log-Jacobian determinant, and their different meaning when used as index of anatomical changes in morphometric studies.

The proposed methods were extensively tested on large publicly available dataset in both inter and intra-subject registration settings, and the results were comparable with those obtained by the most referenced methods. To conclude, the LCC-Demons is a candidate instrument for both research and clinically oriented purposes, as already showed in scientific works based on the presented method [Lorenzi et al., 2012a, Lorenzi et al., 2012e, Lorenzi et al., 2012d].

Acknowledgment

Data collection and sharing for this project was funded by the Alzheimer's Disease Neuroimaging Initiative (ADNI) (National Institutes of Health Grant U01 AG024904). ADNI is funded by the National Institute on Aging, the National Institute of Biomedical Imaging and Bioengineering, and through generous contributions from the following: Abbott; Alzheimer's Association; AlzheimerâĂŹs Drug Discovery Foundation; Amorfix Life Sciences Ltd.; AstraZeneca; Bayer HealthCare; BioClinica, Inc.; Biogen Idec Inc.; Bristol-Myers Squibb Company; Eisai Inc.; Elan Pharmaceuticals Inc.; Eli Lilly and Company; F. Hoffmann-La Roche Ltd and its affiliated company Genentech, Inc.; GE Healthcare; Innogenetics, N.V.; IXICO Ltd.; Janssen Alzheimer Immunotherapy Research & Development, LLC.; Johnson & Johnson Pharmaceutical Research & Development LLC.; Medpace, Inc.; Merck & Co., Inc.; Meso Scale Diagnostics, LLC.; Novartis Pharmaceuticals Corporation; Pfizer Inc.; Servier; Synarc Inc.; and Takeda Pharmaceutical Company. The Canadian Institutes of Health Research is providing funds to support ADNI clinical sites in Canada. The grantee organization is the Northern California Institute for Research and Education, and the study is coordinated by the Alzheimer's Disease Cooperative Study at the University of California, San Diego. ADNI data are disseminated by the Laboratory for Neuro Imaging at the University of California, Los Angeles. This research was also supported by NIH grants P30 AG010129 and K01 AG030514.

2.A Optimization of the LCC-Demons Correspondence

In this section we derive the update formula for the optimization of the LCC symmetric correspondence (2.5).

$$E_{sym}^{LCC}(\delta\mathbf{v}, F, G) = \frac{1}{\sigma_i^2}\rho^2(\delta\mathbf{v}, F, G) + \frac{1}{\sigma_x^2}\|\delta\mathbf{v}\|_{L_2}^2. \tag{2.10}$$

The symmetric LCC correspondence considers the symmetric resampling of the images, and is optimized with respect to the symmetric composition by the update field $\exp(\frac{\delta\mathbf{v}}{\mathbf{2}})$. We have the following Taylor expansion:

$$F^{\frac{\delta\mathbf{v}}{2}} = F \circ \exp(-\frac{\delta\mathbf{v}}{2}) = F - \nabla F^T \cdot \frac{\delta\mathbf{v}}{2} + O(\|\delta\mathbf{v}\|^2),$$

and

$$G^{\frac{\delta\mathbf{v}}{2}} = G \circ \exp(\frac{\delta\mathbf{v}}{2}) = G + \nabla G^T \cdot \frac{\delta\mathbf{v}}{2} + O(\|\delta\mathbf{v}\|^2).$$

The updated factors of the denominator of the local correlation coefficient $\left(\mathbf{G}_\sigma * ([F^{\frac{\delta\mathbf{v}}{2}}]^2)\right)^{-\frac{1}{2}}$, and $\left(\mathbf{G}_\sigma * ([G^{\frac{\delta\mathbf{v}}{2}}]^2)\right)^{-\frac{1}{2}}$ can be approximated by

$$\left(\mathbf{G}_\sigma * ([F^{\frac{\delta\mathbf{v}}{2}}]^2)\right)^{-\frac{1}{2}} \simeq \frac{1}{\sqrt{\mathbf{G}_\sigma * (F^2)}} + \frac{\mathbf{G}_\sigma * (F\nabla F^T \cdot \delta\mathbf{v})}{2\left(\mathbf{G}_\sigma * (F^2)\right)^{\frac{3}{2}}} + O(\|\delta\mathbf{v}\|^2),$$

and

$$\left(\mathbf{G}_\sigma * ([G^{\delta\mathbf{v}}]^2)\right)^{-\frac{1}{2}} \simeq \frac{1}{\sqrt{\mathbf{G}_\sigma * (G^2)}} - \frac{\mathbf{G}_\sigma * (G\nabla G^T \cdot \delta\mathbf{v})}{2\left(\mathbf{G}_\sigma * (G^2)\right)^{\frac{3}{2}}} + O(\|\delta\mathbf{v}\|^2),$$

and the expansion for the LCC term can be written as

$$\begin{aligned}\rho^{\delta\mathbf{v}} &\simeq \rho + \frac{1}{2}\frac{\mathbf{G}_\sigma * (F\nabla G^T \cdot \delta\mathbf{v} - G\nabla F^T \cdot \delta\mathbf{v})}{\sqrt{\mathbf{G}_\sigma * (F^2)\mathbf{G}_\sigma * (G^2)}} \\ &+ \frac{\rho}{2}\left(\frac{\mathbf{G}_\sigma * (F\nabla F^T \cdot \delta\mathbf{v})}{\mathbf{G}_\sigma * (F^2)} - \frac{\mathbf{G}_\sigma * (G\nabla G^T \cdot \delta\mathbf{v})}{\mathbf{G}_\sigma * (G^2)}\right) + O(\|\delta\mathbf{v}\|^2).\end{aligned}$$

With the assumption of a sufficiently smooth update field such that for each image I, $\mathbf{G}_\sigma * (\nabla I^T \cdot \delta\mathbf{v}) \simeq \mathbf{G}_\sigma * (\nabla I^T) \cdot \delta\mathbf{v}$, we finally obtain:

$$\begin{aligned}\rho^{\delta\mathbf{v}} &\simeq \rho + \frac{\rho}{2}\Big(\frac{\mathbf{G}_\sigma * (F\nabla G^T)}{\mathbf{G}_\sigma * (FG)} - \frac{\mathbf{G}_\sigma * (G\nabla F^T)}{\mathbf{G}_\sigma * (FG)} \\ &+ \frac{\mathbf{G}_\sigma * (F\nabla F^T)}{\mathbf{G}_\sigma * (F^2)} - \frac{\mathbf{G}_\sigma * (G\nabla G^T)}{\mathbf{G}_\sigma * (G^2)}\Big)\delta\mathbf{v} + O(\|\delta\mathbf{v}\|^2) \\ &= \rho + \frac{\rho}{2}\Lambda\delta\mathbf{v} + O(\|\delta\mathbf{v}\|^2).\end{aligned}$$

The approximated squared LCC is therefore

$$(\rho^{\delta\mathbf{v}})^2 \simeq \left(\rho + \frac{\rho}{2}\Lambda\delta\mathbf{v}\right)^2 = \rho^2(1 + \frac{1}{2}\Lambda\delta\mathbf{v} + \frac{1}{4}\delta\mathbf{v}^T\Lambda^T\Lambda\delta\mathbf{v}),$$

whose gradient and Hessian are respectively $D((\rho^{\delta\mathbf{v}})^2) = \frac{\rho^2}{2}\Lambda$, and $H((\rho^{\delta\mathbf{v}})^2) = \frac{\rho^2}{4}\Lambda^T\Lambda$. To optimal of 5.1 is then given by the equation:

$$\left(H((\rho^{\delta\mathbf{v}})^2) + \frac{\sigma_i^2}{\sigma_x^2}\mathrm{Id}\right)\delta\mathbf{v} = -D((\rho^{\delta\mathbf{v}})^2),$$

whose solution is

$$\delta\mathbf{v} = -\frac{2\Lambda}{\|\Lambda\|^2 + \frac{4}{\rho^2}\frac{\sigma_i^2}{\sigma_x^2}},$$

thanks to the Sherman Morrison formula [Vercauteren, 2008].

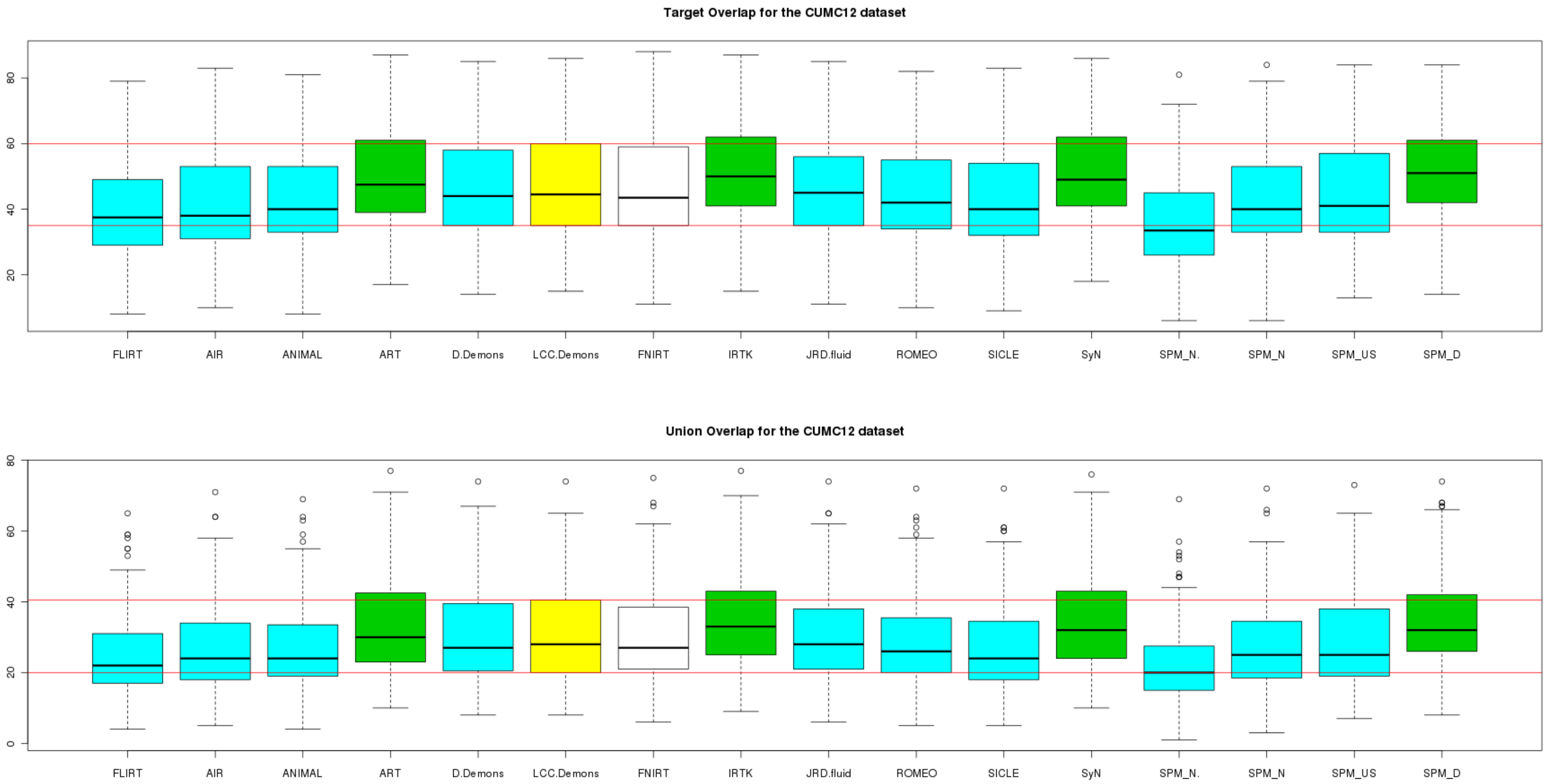

Figure 2.4: Inter-subject registration on the CUMC12 dataset: target and union overlap on the labeled regions. Yellow: LCC-Demons. Blue: significantly lower overlaps. Green: significantly higher overlaps. White: no significant difference ($p<0.05$, paired t-test on the labeled regions). Red lines: upper and lower quartiles of the LCC-Demons overlaps.

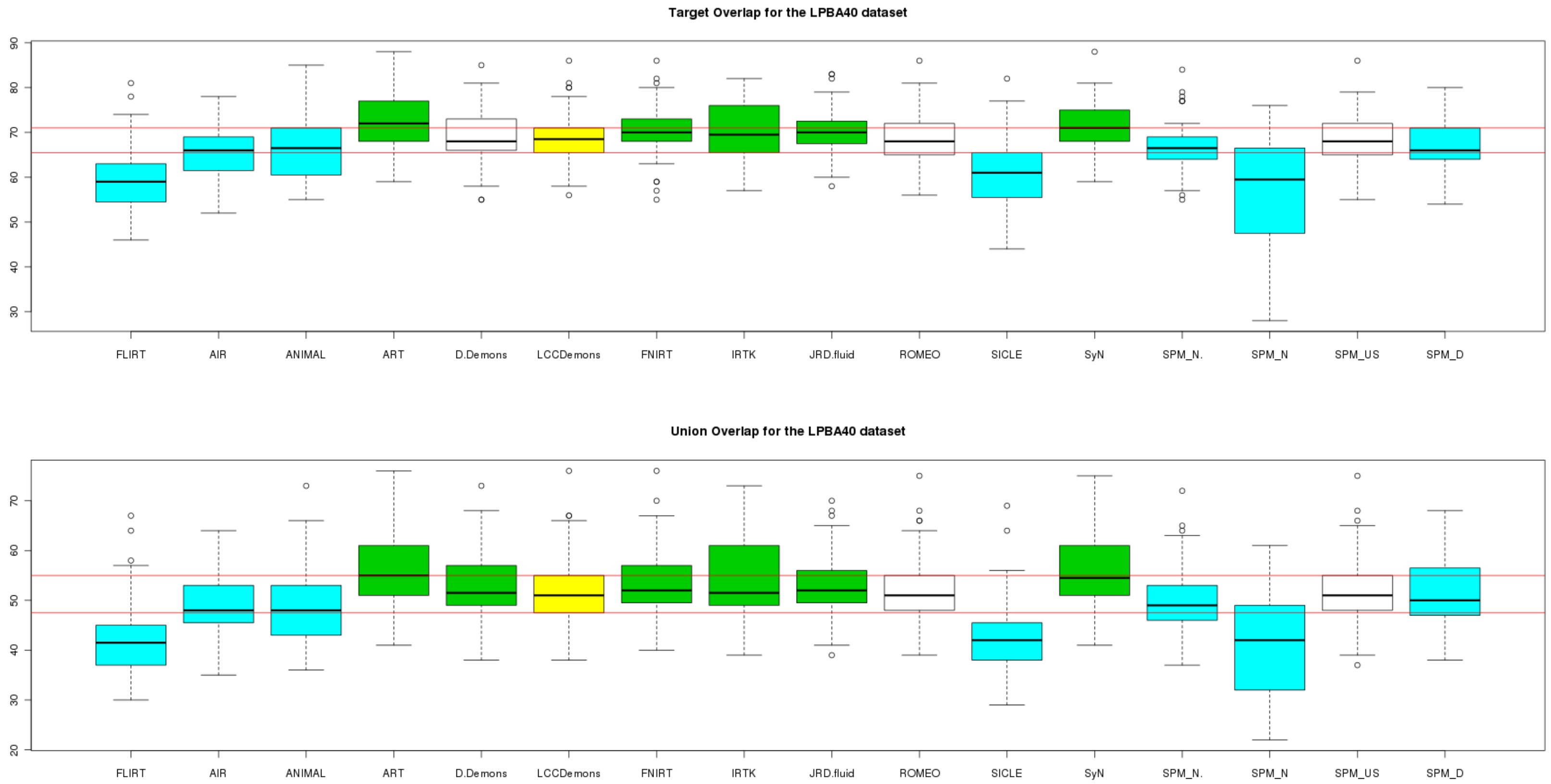

Figure 2.5: Inter-subject registration on the LPBA40 dataset: target and union overlap on the labeled regions. Yellow: LCC-Demons. Blue: significantly lower overlaps. Green: significantly higher overlaps. White: no significant difference ($p<0.05$, paired t-test on the labeled regions). Red lines: upper and lower quartiles of the LCC-Demons overlaps.

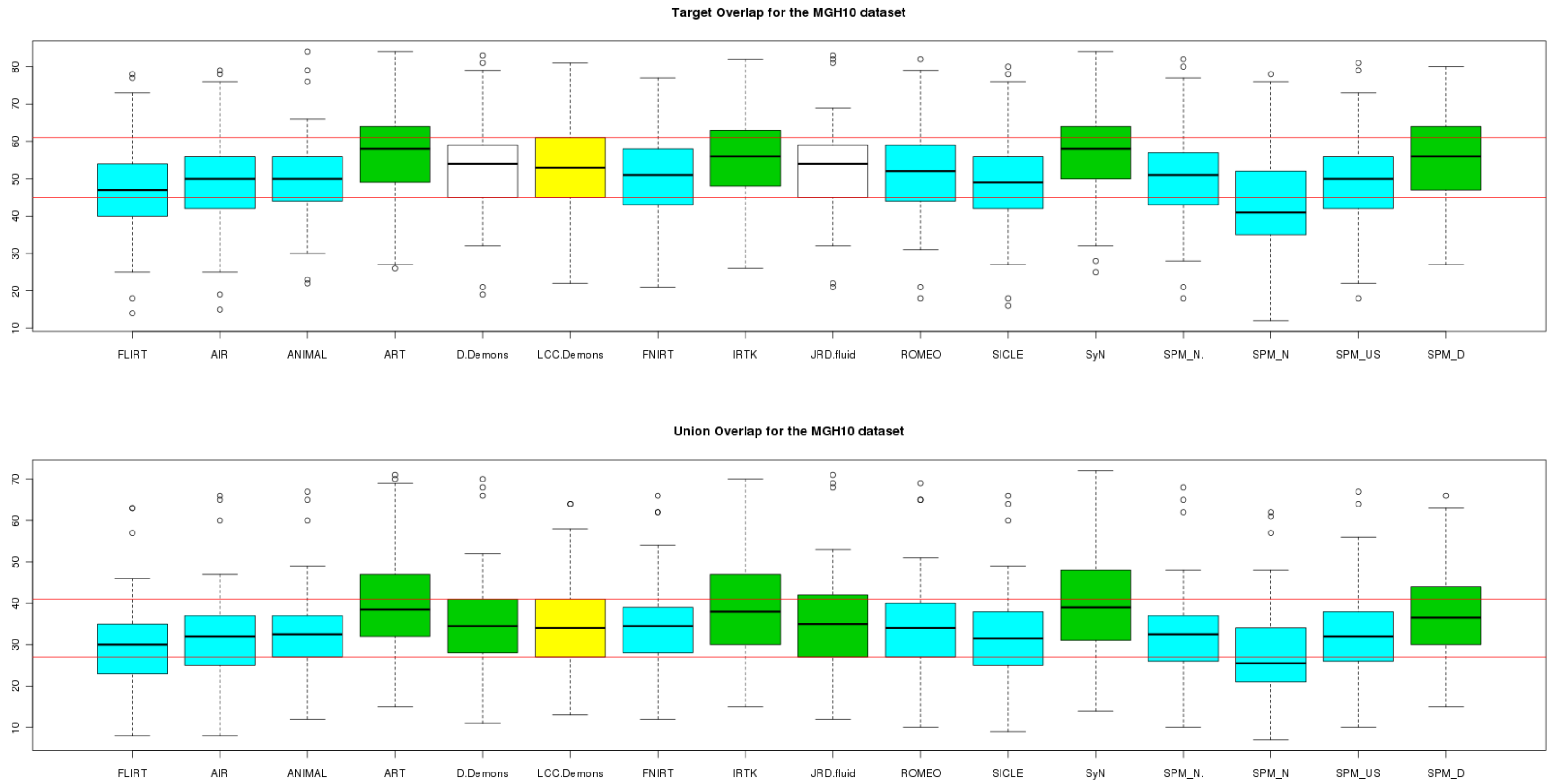

Figure 2.6: Inter-subject registration on the MGH10 dataset: target and union overlap on the labeled regions. Yellow: LCC-Demons. Blue: significantly lower overlaps. Green: significantly higher overlaps. White: no significant difference ($p<0.05$, paired t-test on the labeled regions). Red lines: upper and lower quartiles of the LCC-Demons overlaps.

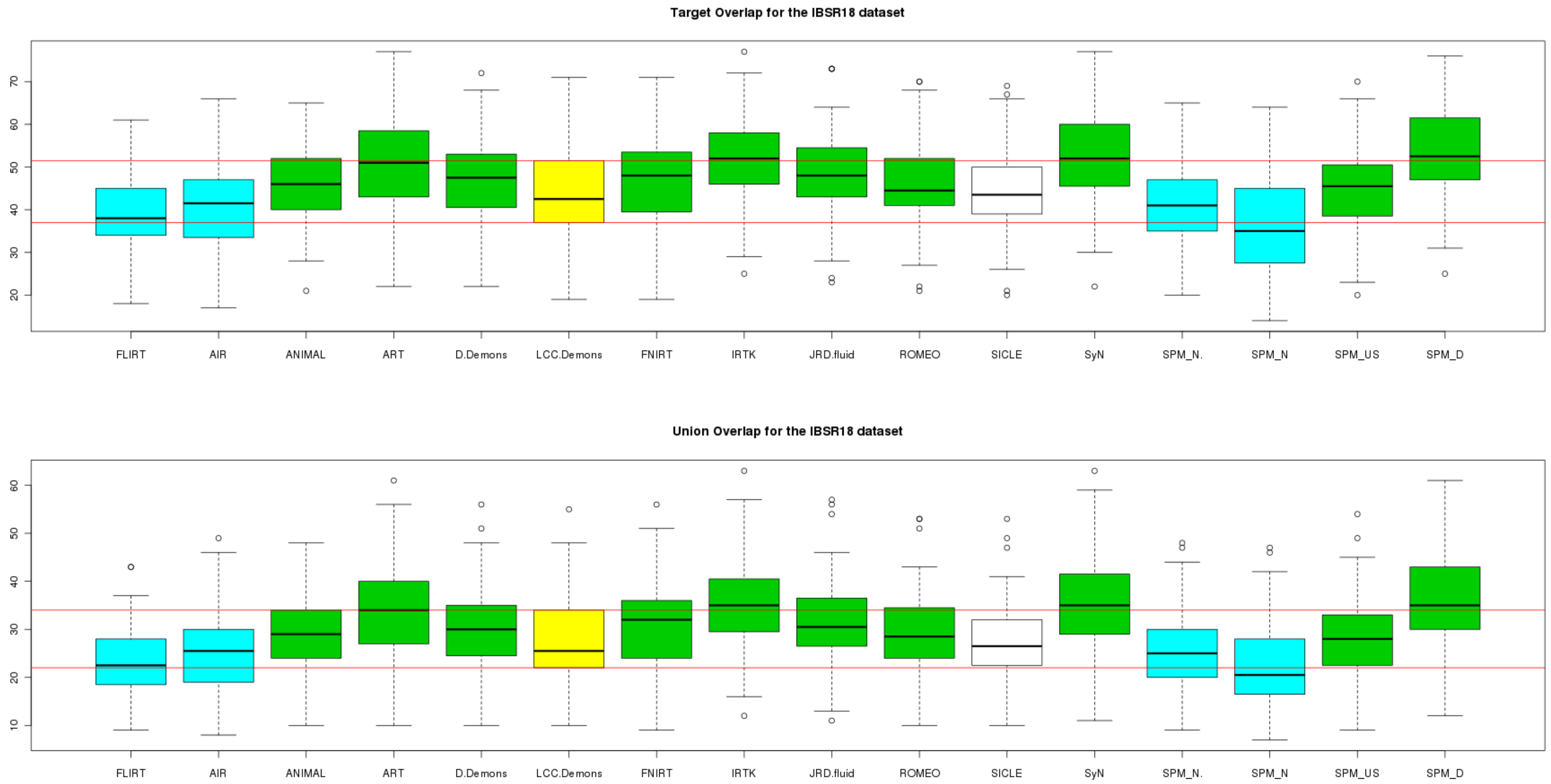

Figure 2.7: Inter-subject registration on the IBSR18 dataset: target and union overlap on the labeled regions. Yellow: LCC-Demons. Blue: significantly lower overlaps. Green: significantly higher overlaps. White: no significant difference ($p<0.05$, paired t-test on the labeled regions). Red lines: upper and lower quartiles of the LCC-Demons overlaps.

CHAPTER 3

Ladders for the parallel transport of deformations in time series of images

---

Contents

In Chapter 2 we introduced the tool for measuring the anatomical changes in cross-sectional and longitudinal studies. This chapter provides a computational method for transporting the estimated longitudinal atrophy trajectories along inter-subject deformations. It will be soon submitted to the SIAM Journal on Imaging Sciences (SIIMS) and is based on the conference paper [Lorenzi et al., 2011b].

Based on:

[Lorenzi et al., 2011b] M. Lorenzi, N. Ayache, X. Pennec. Schild's Ladder for the parallel transport of deformations in time series of images *Proceedings in Information Processing on Medical Imaging - IPMI*, 463–474, 2011.

Additional material available in [Lorenzi et al., 2012c].

Follow-up imaging studies require the evaluation of the anatomical changes over time for specific clinical groups. The longitudinal changes for a specific subject can be evaluated through the non-rigid registration of successive anatomical images. However, to perform a longitudinal group-wise analysis, the subject-specific longitudinal trajectories of anatomical points need to be transported in a common reference frame. In this work, we propose an effective method based on the Schild's Ladder for transporting longitudinal deformations in time series of images in a common space using diffeomorphic registration. We illustrate the computational advantages and demonstrate the numerical accuracy of this very simple method by comparing with standard methods of transport on simulated images with progressing brain atrophy. Finally, its application to the clinical problem of the measurement of the longitudinal progression in Alzheimer's disease suggests that an important gain in sensitivity could be expected on group-wise comparisons.

3.1 Introduction

One of the main objectives in the field of computational anatomy concerns the modeling of the dynamics occurring in specific clinical groups. This is motivated by the need to generalize the characteristics observed in the single patients, through group-wise statistics. The aim of the Template-based analysis is therefore to describe the subject-specific characteristics in a normalized reference frame by transporting the individual geometries in a common space. Different normalization methods can be used for static observations, depending on the complexity of the feature of interest: resampling for scalar values, reorientation for vectors, and more advanced methods for tensors, like Preservation of the Principal Directions (PPD) or the Finite Strain (FS) [Alexander et al., 2001].

3.1.1 Transport of Longitudinal Trajectories

The problem of modeling dynamic quantities, such as the changes measured in time series of images, is a more complex issue. Ideally, when transporting from a subject to the template space, we should preserve the geometrical properties of the initial trajectory while adapting to the new coordinate system. Therefore, we are interested in the behaviour of the transported dynamics, especially regarding the ability to preserve the original amount of expansion/contraction in homologous regions. A key issue is the different nature of the changes occurring at the intra-subject level, which reflects the biological phenomena of interest, and the changes across different subjects. In fact, the inter-subject variability is a scale of magnitude higher than the more subtle subject-specific variations: the way we mix these two levels has a deep impact on the sensitivity of the resulting normalized measures. Thus, in order to preserve and accurately quantify the dynamics in the template space, a rigorous and reliable procedure need to be defined.

Different approaches for the transport of measures of change have been proposed, depending on the type of measure of change that is considered (time series of Jacobian images, the time-varying initial momentum, displacement fields as a function of time, etc.). A simple method of transport consists in *reorienting* the longitudinal inter-subject displacement *vector field* by the Jacobian matrix of the subject-to-template mapping. A drawback of this method, as stated before, is that the longitudinal deformation is fully combined to the inter-subject one. The method proposed by [Rao et al., 2004] uses the *transformation conjugation* (change of coordinate system) from the group theory in order to compose the longitudinal inter-subject deformation with the subject-to-template one. As pointed out in [Bossa et al., 2010], this practice could potentially introduce variations in the transported deformation and relies on the inverse consistency of the estimated deformations, which can raise problems for large deformations. The *parallel transport* of relational measures was introduced in [Younes, 2007a] in the context of the Large Deformation Diffeomorphic Metric Mapping (LDDMM) [Miller et al., 2002]. The notion of parallel transport proposed here consists in translating a vector *along a geodesic* while preserving the parallelism according to the space geometry. This framework allows to transport the geodesic diffeomorphic registration for both point supported data and images, and it was applied to study the hippocampal shape changes in Alzheimer's disease [Qiu et al., 2008a, Qiu et al., 2009] . Although it represents a rigorous implementation of the parallel transport it is limited to the transport along geodesics of the right invariant metric on diffeomorphisms, and it comes to the price of a computationally intense scheme. This is a limitation which could prevent the application to large datasets with multiple time series of images, which are now becoming more easily available to the imaging community (for example the ADNI).

In tensor based morphometry, the transport is used to normalize in a common reference frame the degree of changes in specific regions, such as the hippocampal volume loss in the brain. For this purpose, it is also possible to directly normalize the measures of change by interpolating the Jacobian determinant scalar map of the intra-subject longitudinal change into the template reference [Bossa et al., 2010]. However, the Jacobian determinant represents only one of the several features of interest in morphometric studies (like full Jacobian matrices, tensors or the flux [Chung et al., 2001], [Lorenzi et al., 2010a]). Moreover, transporting the original deformation trajectory allows multivariate group analysis like evaluation of mean deformations, PCA, etc.

The aim of the present paper is to propose an effective computational method for the parallel transport of longitudinal trajectories of deformations. After introducing in Section 2 the "Schild's Ladder", a general parallel transport technique defined in the past century in the field of general relativity, we propose the "Pole Ladder", an optimized transport scheme for the efficient transport of longitudinal trajectories of deformations vectors along any piecewise geodesic. The effectiveness of the scheme is tested in both synthetic and real data, with an application to the modeling of the longitudinal progression of atrophy in Alzheimer's disease.

3.2 Ladders for the Parallel Transport of Tangent Vectors.

3.2.1 The Schild's Ladder

The Schild's Ladder was introduced in the last century in the field of the general relativity after the physicist Alfred Schild [KSchild, 1970, Misner et al., 1973]. It provides a straightforward method to compute a first order approximation of the parallel transport of a vector along a curve using geodesics only, and without requiring the knowledge of the tangent structure of the space. Let M a manifold and C a curve parametrized by the parameter τ with $\frac{\partial C}{\partial \tau}|_{T_0} = \mathbf{u}$, and $\mathbf{A} \in T_{P_0}M$, a tangent vector on the curve at the point $P_0 = C(0)$. Let P_1 be a point on the curve relatively close to P_0, i.e. separated by a sufficiently small parameter value τ.

The Schild's Ladder computes the parallel transport of $\mathbf{A}$ along the curve C as follows:

1. Define a *curve* on the manifold parametrized by a parameter σ passing through the point P_0 with tangent vector $\frac{\partial}{\partial \sigma}|_{P_0} = \mathbf{A}$. Chose a point P_2 on the curve separated by P_0 by the value of the parameters σ. The values of the parameters σ and τ should be chosen in order to construct the Schild's Ladder within a single coordinate neighborhood.

2. Let l be the *geodesic* connecting $P_2 = l(0)$ and $P_1 = l(\lambda)$, we chose the "middle point" $P_3 = l(\lambda/2)$. Now, let us define the *geodesic* r connecting the starting point P_0 and P_3 parametrized by ρ such that $P_3 = r(\rho)$. Extending the geodesic at the parameter 2ρ we reach the point P_4. We can now pick a *curve* connecting P_1 and P_4. The vector A' tangent to the curve at the point $P1$ is the parallel translation of A along C.

3. If the distance between the points P_0 and P_1 is large, the above construction can be iterated for a sufficient number of small steps.

The geometrical approximation of the Schild's ladder resides in the assumption that all the geometrical information of the space are encoded by the geodesics. Although the geodesics on the manifold are not sufficient to recover all the information about the space properties, such as the connection, it has been shown that the Schild's Ladder describes the parallel transport with respect to the symmetric part of the connection of the space [Kheyfets et al., 2000]. An intuitive proof is that the construction of the above diagram is commutative and can be symmetrized with respect to the points P_1 and P_2. If the original connection is symmetric, then this procedure provides a correct linear approximation of the parallel transport of vectors.

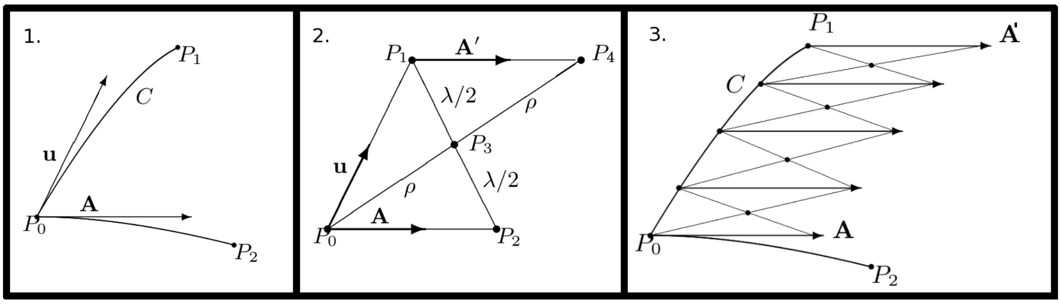

Figure 3.1: The Schild' ladder parallel transports a vector $\mathbf{A}$ along the curve C by iterative construction of geodesic parallelograms.

3.2.2 The Pole Ladder

We propose here a different construction for the parallel transport of vectors on geodesics parallelograms. If the curve C is geodesic, then it can be itself one of the diagonals and the Schild's ladder can therefore be adapted by requiring the computation of only one new diagonal of the parallelogram. We define in this way a different ladder scheme, that we call here "Pole ladder".

We shall prove that the Pole ladder is actually a parallel transport. By considering the diagram in Figure 3.2, if C has parameter μ then the geodesic equation for the transport of the tangent vector $\mathbf{v}_p$ along C is $\frac{\partial \mathbf{v_P}}{\partial \mu} + \Gamma^k_{ij}\mathbf{v}^i_P\mathbf{v}^j_P = 0$. In a sufficiently small neighborhood the relationships can be linearized to give

$$\mathbf{v}^k_P \quad = \quad \mathbf{v}^k_M + \Gamma^k_{ij}\mathbf{v}^i_P\mathbf{v}^j_P,$$

and

$$x^k_M \quad = \quad x^k_{P_0} + \mathbf{v}^k_M + \Gamma^k_{ij}\mathbf{v}^i_P\mathbf{v}^j_P.$$

In the same way we have $x^k_M = x^k_{P_1} + \mathbf{u}^k_M + \Gamma^k_{ij}\mathbf{u}^i_P\mathbf{u}^j_P$.

Therefore

$$\mathbf{A} = x^k_{P_1} - x^k_{P_0} = \mathbf{u}^k_M - \mathbf{v}^k_M + \Gamma^k_{ij}\alpha^{ij}$$

with $\alpha^{ij} = (\mathbf{v}^i_P - \mathbf{u}^i_P)(\mathbf{v}^j_P - \mathbf{u}^j_P) = \mathbf{A}^i\mathbf{A}^j$. Since $\mathbf{v}^k_M = (x_{Q_0} - x_M)^k$ and $\mathbf{u}^k_M = (x_{Q_1} - x_M)^k$ we finally have

$$\mathbf{A}'^k = -\left(\mathbf{A}^k + \Gamma^k_{ij}\mathbf{A}^i\mathbf{A}^j\right).$$

3.3 Application to Images

Let I_i $(i = 1 \dots n)$ be a time series of images with the baseline I_0 as reference. Consider a template image T_0, the aim of the procedure is to compute the image T_i

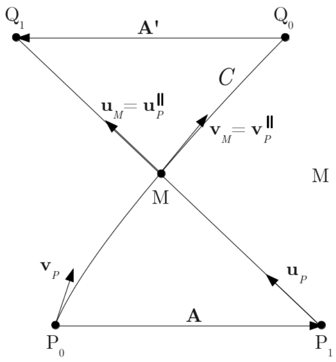

Figure 3.2: The Pole ladder parallel transports the vector **A** along the geodesic C. Differently from the Schild's ladder it requires to compute only one diagonal geodesic.

in order to define the transport of the sequence $I_0, \ldots, I_i$ in the reference of T_0. In the sequel, we focus on the transport of a single image I_1.

To apply the ladders in the context of the images, we define the paths in the space of images by action from the space of diffeomorphism. Let $\mathbb{I} = \{f : \mathbb{R}^3 \to \mathbb{R}\}$ the image space and let us define the action $* : M \times \mathbb{I} \to \mathbb{I}$ given by $(\varphi, I) \mapsto \varphi * I = I \circ \varphi^{-1}$, where M is the space of the diffeomorphisms. If the distance between two images in the image space is defined in terms of diffeomorphisms [Younes, 2007a], then the geodesics in the image space are defined by the action of the geodesic paths in the space of the diffeomorphisms.

3.3.1 Schild's Ladder for Images

The Schild's Ladder can be naturally translated in the image context (Algorithm 4), by requiring the computation of the two diagonal geodesics l and r (Subsection 3.2.1).

Algorithm 4 Schild's ladder for the transport of a longitudinal deformation.

```
1. Compute the geodesic $l(\lambda)$ in the space $\mathbb{I}$ connecting $I_1$ and $T_0$
   such that $l(0) = I_1$, and $l(1) = T_0$.
2. Define the half-space image $l(1/2) = I_{\frac{1}{2}}$.
3. Compute the geodesic $r(\rho)$ connecting $I_0$ and $I_{\frac{1}{2}}$
   such that $r(0) = I_0$ and $r(1) = I_{\frac{1}{2}}$.
4. Define the transported follow-up image as $T_1 = r(2) = h(2) * I_0$.
5. The transported deformation is given by registering the images $T_0$ and $T_1$.
```

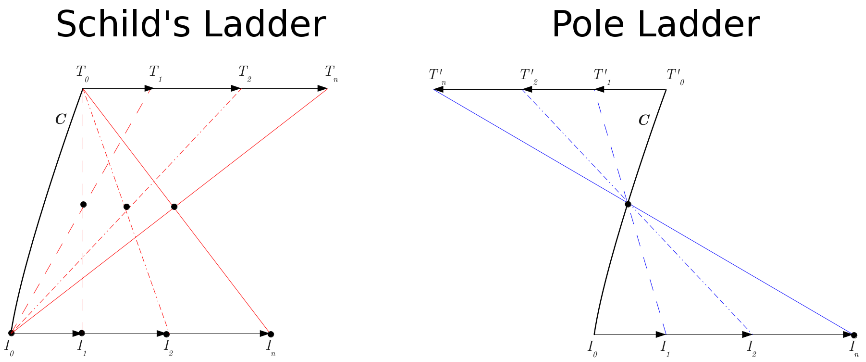

Figure 3.3: Geometrical schemes in the Schild's ladder and in the Pole ladder. By using the curve C as diagonal, the Pole ladder requires half times the number of geodesics needed by the Schild's ladder.

3.3.2 Pole Ladder for Images

The Pole ladder is similar to the Schild's one, with the difference of explicitly using as a diagonal the geodesic C which connects I_0 and T_0. This is an interesting property since, given C, it requires the computation of only one additional geodesic, thus the transport of time series of images is based on the same baseline-to-reference curve C (Figure 3.3).

Algorithm 5 Pole ladder for the transport of a longitudinal deformation.

```
1. Compute the geodesic $C(\mu)$ in the space $\mathbb{I}$ connecting $I_0$ and $T_0$
   such that $C(0) = I_0$ and $C(1) = T'_0$.
2. Define the half-space image $C(1/2) = I'_{\frac{1}{2}}$.
3. Compute the geodesic $g(\eta)$ connecting $I_1$ and $I'_{\frac{1}{2}}$
   such that $g(0) = I_1$ and $g(1) = I'_{\frac{1}{2}}$.
4. Define the transported follow-up image as $T'_1 = g(2)$
5. Compute the path $p(t)$ such that $p(0) = T_0$ and $p(1) = T'_1$.
   The transported deformation is given by registering $p(0) = T_0$ to $p(-1)$.
```

For this reason, while in [Lorenzi et al., 2011b] we proposed an efficient implementation of the Schild's ladder, the following section focuses on the similar implementation of the Pole ladder for the transport of deformation trajectories.

3.3.3 Effective Pole Ladder by Using One Parameter Subgroups

Despite its straightforward formulation, the application of the Pole ladder to the image space requires multiple evaluations of geodesics in the space of diffeomorphisms and a consequent high cost in terms of computation time and resources.

Moreover, it assumes an exact matching, which is bound to lead to important numerical problems. For instance, the definition of $I_{\frac{1}{2}}$ using the forward deformation on I_0 or the backward from T_0 lead to very different results. We propose to reformulate the above scheme in a computationally efficient and numerically stable framework using only transformations.

We use the setting of the SVFs (SVF) diffeomorphic registration as provided for example by the log-Demons [Vercauteren et al., 2008], or the LCCDemons (Chapter 2) algorithms. In particular we base the ladder on the path defined by the Lie group exponential of vectors. The fact that the one-parameter subgroup is a geodesic will be justified in the next chapter. We note that the SVF is a valid approximation of a small step of a time-varying velocity field diffeomorphism. Given a pairs of images I_i, $i \in \{0, 1\}$, the SVF framework parametrizes the diffeomorphism φ required to match the reference I_0 to the moving image I_1 by a SVF u. The velocity field u is an element of the Lie Algebra $\mathbf{G}$ of the Lie group of diffeomorphisms M, i.e. an element of the tangent space at the identity $T_{id}M$. The diffeomorphism φ belongs to the one parameter subgroup generated by u and is parametrized by the Lie group exponential operator $\varphi = \exp(u)$. We can therefore define the paths in the space of the diffeomorphisms from the one parameter subgroup parametrization $l(\lambda) = \exp(\lambda \cdot u)$ and by consequence the paths in the image space.

However, the ladders in the image space requires a number of interpolations and exponentiations, which could introduce biases due to the numerical approximations. Moreover the registration is constrained to be smooth and it is therefore impossible to reach a perfect match of corresponding intensities in the registered images. We however take advantage of the symmetry of the construction in order to be robust to the changes introduced by the registration.

1. Let $I_1 = \exp(u) * I_0$.
2. Compute $v = argmin_{v \in \mathbb{G}} E\left(T_0 \circ \exp(-v/2), I_0 \circ \exp(v/2)\right)$, where E is a generic registration energy functional to be minimized.

   The half space image $I_{\frac{1}{2}}$ can be defined in terms of $v/2$ as $\exp(-v/2) * T_0$ or $\exp(v/2) * I_0$. While from the theoretical point of view the two images are identical, the choice of one of them, or even their mean, introduces a bias in the construction. The definition of the half step image can be bypassed by relying on the symmetric construction of the parallelogram (Figure 3.4).
3. The transformation from I_1 to $I_{\frac{1}{2}}$ is $\rho = \exp(v/2) \circ \exp(-u)$ and the symmetry leads to

$$\exp\left(\Pi(u)\right) \quad = \quad \exp(v/2) \circ \exp(u) \circ \exp(-v/2).$$

The transport of the deformation $\varphi = \exp(u)$ can be therefore obtained through the conjugate action operated by the deformation parametrized by $v/2$.

Since the direct computation of the conjugate by composition is potentially biased by the discrete approximation, we propose two different schemes to correctly evaluate the transport directly in the Lie Algebra.

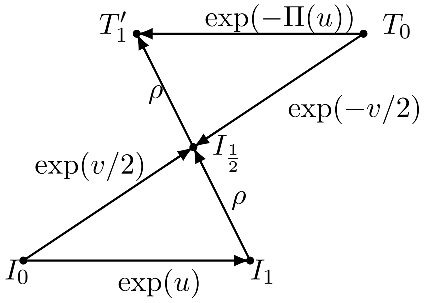

Figure 3.4: Pole Ladder with the one parameter subgroups. The transport $\exp(\Pi(u))$ is the deformation $\exp(v/2) \circ \exp(u) \circ \exp(-v/2)$

3.3.4 BCH Formula for the Conjugate Action

The Baker Campbell Hausdorff (BCH) formula was introduced in the SVF diffeomorphic registration in [Bossa et al., 2007] and provides an explicit way to compose diffeomorphisms by operating in the associated Lie Algebra. More specifically, if v, u are SVFs, then $\exp(v) \circ \exp(u) = \exp(w)$ with $w = BCH(v,u) = v + u + \frac{1}{2}[v,u] + \frac{1}{12}[v,[v,u]] - \frac{1}{12}[u,[v,u]] + \ldots$. In particular, for small u, the computation can be truncated to any order to obtain a valid approximation for the composition of diffeomorphisms. Applying the truncate BCH to the conjugate action leads to

$$\Pi_{BCH}(u) \quad \simeq \quad u + [v/2, u] + \frac{1}{2}[v/2,[v/2,u]]. \tag{3.1}$$

In fact, let consider the following second order truncation of the BCH formula

$$BCH((v/2,u) \simeq v/2 + u + \frac{1}{2}[v/2,u] + \frac{1}{12}[v/2,[v/2,u]] - \frac{1}{12}[u,[v/2,u]].$$

The composition

$$\Pi_{BCH}(u) = BCH\left(v/2, BCH(u,-v/2)\right)$$

writes as

$$\begin{aligned}\Pi(u)^v \quad = \quad & \underbrace{v/2 + BCH(u,-v/2)}_{A} + \underbrace{\frac{1}{2}[v/2, BCH(u,-v/2)]}_{B} \\ & + \underbrace{\frac{1}{12}[v/2,[v/2,BCH(u,-v/2)]]}_{C} - \underbrace{\frac{1}{12}[BCH(u,-v/2),[v/2,BCH(u,-v/2)]]}_{D}.\end{aligned}$$

The second order truncation of the four terms is:

$$\begin{array}{rcl} A & \simeq & u + \frac{1}{2}[u, -v/2] + \frac{1}{12}[u, [u, -v/2]] - \frac{1}{12}[-v/2, [u, -v/2]] \\ B & \simeq & \frac{1}{2}[v/2, u] + \frac{1}{4}[v/2, [u, -v/2]] \\ C & \simeq & \frac{1}{12}[v/2, [v/2, u]] \\ D & \simeq & -\frac{1}{12}[u, [v/2, u]] + \frac{1}{12}[v/2, [v/2, u]] \end{array}$$

From the additive and anticommutative properties of the Lie bracket, adding the four terms leads to (3.1).

To provide a sufficiently small vector for the computation of the conjugate we can take advantage of the properties of the one-parameter subgroups to observe that

$$\begin{array}{rl} & \exp(v) \circ \exp(u) \circ \exp(-v) = \\ = & \exp(\frac{v}{n}) \circ \ldots \circ \exp(\frac{v}{n}) \circ \exp(u) \circ \exp(-\frac{v}{n}) \circ \ldots \circ \exp(-\frac{v}{n}) \end{array}$$

The conjugation can then be iteratively computed in the following way:

1. find n such that v/n is small.
2. compute $w = u + [\frac{v}{n}, u] + \frac{1}{2}[\frac{v}{n}, [\frac{v}{n}, u]]$
3. Let $u = w$
4. Iterate the above construction (n steps).

Using the BCH formula allows to perform the transport directly in the Lie algebra and avoids exponentiation and the interpolations, thus reducing the bias introduced by the numerical approximations. Moreover, this methods preserves the original "Ladder" formulation, operated along the path described by $\exp(tv)$. However, it requires a number of iterations to be computed.

3.3.5 Conjugate Action from the Exponential Map

We can provide an alternative and direct formula to compute the transport by conjugate action from the definition of the exponential:

$$\exp(u) = \lim_{n \to \infty} \left(\mathrm{Id} + \frac{u}{n} \right)^n .$$

We can then write:

$$\exp(\Pi_{conj}(u)) \quad = \quad \lim_{n \to \infty} \left(\exp(v/2) \circ \left(\mathrm{Id} + \frac{u}{n} \right) \circ \exp(-v/2) \right)^n .$$

Let $y = \exp(-v/2)(x)$ and $\phi(x) = \exp(v/2)(x)$, then

$$\begin{aligned}
\exp(\Pi_{conj}(u)) &= \lim_{n\to\infty} \left(\phi\left(y + \frac{u(y)}{n}\right)\right)^n = \\
&= \lim_{n\to\infty} \left(\mathrm{Id} + \frac{1}{n}\left(\mathrm{D}(\phi(y))|_{\phi^{-1}(x)} \cdot u \circ \phi^{-1}(x) + o(\|u\|^2)\right)\right)^n .
\end{aligned}$$

By the definition of the exponential map, we obtain then a first order approximation for the transported vector given by

$$\Pi_{conj}(u) = \mathrm{D}\left(\exp(v/2)\right)|_{\exp(-v/2)} \cdot u \circ \exp(-v/2).$$

We note that $\mathrm{D}\left(\exp(v/2)\right)|_{\exp(-v/2)} = \mathrm{D}\left(\exp(-v/2)\right)^{-1}$. This method provides a closed form formula which enables to compute the transport by reorienting the field $u \circ \exp(-v/2)$ by the matrix field $\mathrm{D}\left(\exp(v/2)\right)$ resampled by $\exp(-v/2)$, or equivalently, by the matrix field $\mathrm{D}\left(\exp(-v/2)\right)^{-1}$. The second formula requires however the inversion of a matrix which is an operation potentially more unstable. In the following, the transport $\Pi_{conj}(u)$ is evaluated through the resampling by linear interpolation of the matrix $\mathrm{D}\left(\exp(v/2)\right)$.

From a theoretical point of view the results obtained from the two methods are equivalent in the continuous domain

$$\Pi_{conj}(u) = u + D(v/2) \cdot u - Du \cdot v/2 + O(\|v\|^2) \simeq \Pi_{BCH}(u)$$

3.4 Experiments on Synthetic and Real Data

3.4.1 Comparison of Different Transport Methods

We created a series of realistic simulated deformations based on the deformation field that matches the baseline scan (I_0) of a patient from the ADNI dataset to the 1-year follow-up of the same patient, computed using the LCC-Demons Algorithm (Chapter 2). The ventricular expansion was extracted by masking the corresponding SVF v for a mask including the ventricles. The deformations in the remaining areas of the brain were imposed to be negligible multivariate Gaussian noise. The SVF v was then increasingly scaled ($v_i = f_i v$, with $f_i = 0.5, 1, 2, 3$) and the resulting deformations fields $\varphi_i = \exp(v_i)$ were used to warp the baseline scan I_0 to generate a longitudinal progression of serial images I_i with increasing ventricular expansions.

The longitudinal progression was then transported in a new reference space given by the images of five other patients (target space T_0^k, $k = 1, \ldots, 5$) along the deformation ψ_T^k using different methods:

- Schild's and Pole Ladders (BCH scheme),
- Conjugate Action: $Ad_{\psi_T^k}(\varphi_i) = \psi_T^{k(-1)} \circ \varphi_i \circ \psi_T^k$,

	SVF (u)	Transformation ($\varphi = \exp(u)$)	Scalar Measure (J, log J)
Interpolation of Scalar	No	No	Yes
Conjugate Action	No	Yes	Yes
Schild's Ladder	Yes	Yes	Yes
Pole Ladder	Yes	Yes	Yes
Reorientation	Yes	Yes	Yes

Table 3.1: Different methods of transport and transported features. From the SVF we can infer transformations from which we can extract scalar measures, while the reverse is not possible.

- reorientation of the SVF v_i by the Jacobian Matrix of the deformation ψ_T^k: $J_{\psi_T^k} v_i$.

As summarized in Table 3.1, not all the methods operate on the same features and a direct comparison is not always possible. To test the accuracy of the transport, the different methods were quantitatively compared on the scalar measures representing the amount of change induced in the ventricles. The ventricles masks were segmented for I_0 and T_0^k using a semi-automated method [Yushkevich et al., 2006]. The analyzed features were the average Jacobian and log-Jacobian determinant of the transported deformation, representing respectively the average volume change of the ventricles and the flux of the deformation across the ventricles boundaries (boundary shift) (Chapter 2).

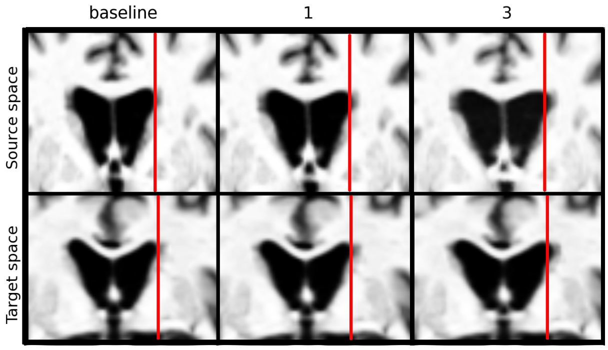

Figure 3.5: Transport of time series of images. Top row: original longitudinal trajectory for the ventricular expansion at the different scaling factors. Bottom row: transported longitudinal sequence in the target space.

3.4.2 Results

In Figure 3.5, we see an example of synthetic time series of images transported by the Schild's Ladder. The series is consistent with the original trajectory of ventricular expansion while adapting to the new reference.

Figure 3.6 compares the log-Jacobian scalar image derived from the different methods for a sample subject. The Conjugate method and the Reorientation led to more noisy maps, while for the Pole and Schild's Ladder (BCH scheme) the resulting Jacobian map adapts to the new reference space while remaining sufficiently smooth, coherently with the simple scalar interpolation in the target space of the original log-Jacobian map.

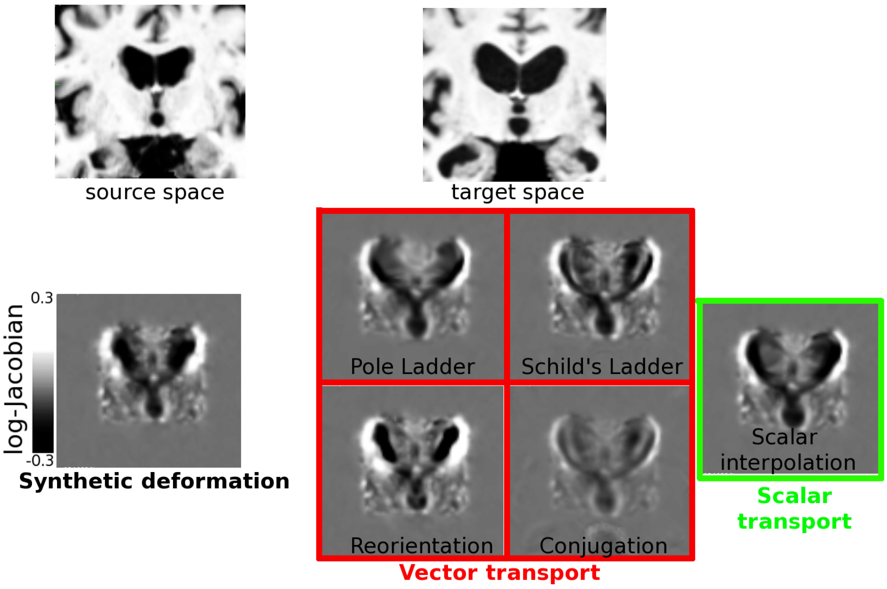

Figure 3.6: Log-Jacobian maps of the transported deformation field from the source space I_0 to a patient's target space. Left: log-Jacobian map corresponding to the synthetic intra-subject deformation φ_1 in the source space. Right: log-Jacobian maps of the deformation in the target space transported thanks to: Pole Ladder, Schils's Ladder, Reorientation, Conjugation, and scalar interpolation of the original log-Jacobian map. Schild's and Pole ladders provide stable results which are consistent with the simple scalar transport.

Table 3.2 shows the amount of changes measured with the different methods. We note that the Pole Ladder provides in most of the cases results similar to those obtained by the simple scalar interpolation, and generally very close to the ones measured in the original reference.

3.4.3 One Year Follow-up Changes on Alzheimer's Disease

Images corresponding to the baseline I_0 and the one-year follow-up I_1 scans were selected for 135 subjects affected by Alzheimer's disease from the ADNI database.

	Jacobian determinant			
Scaling factor	0.5	1	2	3
Source Space	1.052	1.074	1.091	1.106
Schild's Ladder (BCH)	1.062 (.8e-2)	1.094 (1e-2)	1.119 (1.3e-2)	1.13 (1.8e-2)
Pole Ladder (BCH)	1.052 (1e-2)	1.063 (1.2e-2)	1.075 (1.3e-2)	1.086 (1.3e-2)
Reorientation	1.038 (.6e-2)	1.039 (1e-2)	1.033 (1.5e-2)	1.02 (2.1e-2)
Conjugate Action	1.026 (.2e-2)	1.038 (.3e-2)	1.049 (.4e-2)	1.063 (.4e-2)
Scalar Interpolation	1.054 (.59e-2)	1.077 (1.12e-2)	1.092 (1.7e-2)	1.100 (2.4e-2)
	log Jacobian determinant			
Scaling factor	0.5	1	2	3
Source Space	.419	.63	.834	1.03
Schild's Ladder (BCH)	.49 (5e-2)	.8 (6.1e-2)	1.14 (5.4e-2)	1.47 (5.7e-2)
Pole Ladder (BCH)	.37 (9.4e-2)	.56 (14e-2)	.75 (18e-2)	.93 (23e-2)
Reorientation	.5 (8.9e-2)	.76 (13e-2)	1.02 (19e-2)	1.26 (21e-2)
Conjugate Action	.21 (0.5e-2)	.32 (1.2e-2)	.43 (2e-2)	.38 (29e-2)
Scalar Interpolation	.44 (9.5e-2)	.66 (17e-2)	.86 (26e-2)	1.03 (36e-2)

Table 3.2: Average measures (standard deviation) of ventricular changes associated to the initial longitudinal deformations in the source space (first row), and to the deformations transported with the different methods in the target spaces. The Pole Ladder performs similarly to the scalar interpolation while transporting in addition the full SVF.

For each subject i, the pairs of scans were rigidly aligned. The baseline was linearly registered to a reference template and the parameters of the transformation were applied to I_1^i. Finally, for each subject, the longitudinal changes were measured by non-rigid registration using the LCC-Demons algorithm.

The resulting deformation fields $\varphi_i = \exp(v_i)$ were transported with the Pole Ladder (BCH scheme) in the template reference along the subject-to-template deformation. The group-wise longitudinal progression was modeled as the mean of the transported SVFs v_i. The areas of significant longitudinal changes were investigated by one-sample t-test on the group of log-Jacobian scalar maps corresponding to the transported deformations, in order to detect the areas of measured expansion/contraction significantly different from zero.

For sake of comparison, the one sample t-statistic was tested on the subject specific longitudinal log-Jacobian scalar maps transported into the template space along the subject-to-template deformation.

3.4.4 Results

Figure 3.7 shows a detail from the mean SVF from the transported one-year longitudinal trajectories. The field flows outward from the ventricles to indicate a pronounced enlargement. Moreover, we notice an expansion in the temporal horns of the ventricles as well as a consistent contracting flow in the temporal areas. The same effect can be statistically quantified by evaluating the areas where the log-Jacobian maps are statistically different from zero. The areas of significant expansion are located around the ventricles and spread in the CSF areas, while a significant contraction is appreciable in the temporal lobes, hippocampi, parahippocampal gyrus and in the posterior cingulate. The statistical result is in agreement with the one provided by the simple scalar interpolation of the longitudinal subject specific log-Jacobian maps. In fact we do not experience any substantial loss of localisation power by transporting SVFs instead of scalar log-Jacobian maps. However by parallel transporting we preserve also the multidimensional information of the SVFs that, as experienced in chapter 5, potentially leads to more powerful voxel-by-voxel comparisons than the ones obtained with univariate tests on scalars.

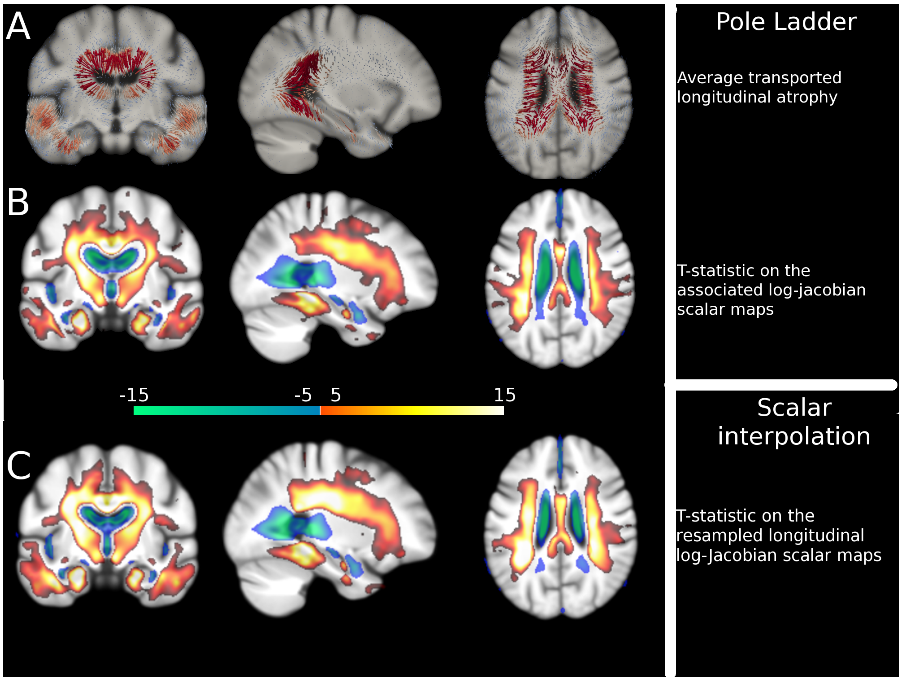

Figure 3.7: One year structural changes for 135 Alzheimer's patients. A) Mean of the longitudinal SVFs transported in the template space with the Pole Ladder. We notice the lateral expansion of the ventricles and the contraction in the temporal areas. B) T-statistic for the correspondent log-Jacobian values significantly different from 0 ($p < 0.001$ FDR corrected). C) T-statistic for longitudinal log-Jacobian scalar maps resampled from the subject to the template space. Blue color: significant expansion, Red color: significant contraction.

3.5 Conclusions and Perspectives

In this study we proposed a novel framework for the transport of longitudinal deformations in a reference space from time series of images. The mathematical formulation was combined with an effective computational scheme in order to provide a reliable and numerically stable solution for the transport of vector fields. The availability of multivariate features in a common space could provide novel information for the understanding of biological processes. Moreover, although designed for transporting vector quantities, the method showed also good results in transporting scalar measures, by preserving smoothness of the corresponding spatial maps and providing accurate numerical evaluations. This is an interesting feature which could increase the power in TBM-like group-wise statistical analysis as well as opening the way to reliable multivariate group-wise analysis. The high spatial resolution of the statistical results on the experiment on the real data suggests a high precision of the procedure in transporting the different subject-specific trajectories. As a perspective, the association of the proposed transport methods with specific frameworks for the estimation of longitudinal trajectories might allow to consistently model the longitudinal changes in clinical populations by including multiple time points, and to compare the progression of different clinical groups on a multidimensional basis (Chapters 5, 6).

Chapter 4

Geodesics, parallel transport & one-parameter subgroups for diffeomorphic image registration

---

Contents

The methods introduced in chapter 3 rely on the rich mathematical setting of the diffeomorphic registration. Here we investigate the theoretical background of diffeomorphic registration and its practical translation to the image registration context. This chapter was accepted for publication on IJCV [Lorenzi and Pennec, 2012].

Computational anatomy aims at developing models to understand the anatomical variability of organs and tissues. A widely used and validated instrument for comparing the anatomy in medical images is non-linear diffeomorphic registration which is based on a rich mathematical background. For instance, the "large deformation diffeomorphic metric mapping" (LDDMM) framework defines a Riemannian setting by providing a right invariant metric on the tangent spaces, and solves the registration problem by computing geodesics parametrized by time-varying velocity fields. A simpler alternative based on Stationary Velocity Fields (SVF) has been proposed, using the one-parameter subgroups from Lie groups theory. In spite of its better computational efficiency, the geometrical setting of the SVF is more vague, especially regarding the relationship between one-parameter subgroups and geodesics. In this work, we detail the properties of finite dimensional Lie groups that highlight the geometric foundations of one-parameter subgroups. We show that one can define a proper underlying geometric structure (an affine manifold) based on the canonical Cartan connections, for which one-parameter subgroups and their translations are geodesics. This geometric structure is perfectly compatible with all the group operations (left, right composition and inversion), contrarily to left- (or right-) invariant Riemannian metrics. Moreover, we derive closed-form expressions for the parallel transport. Then, we investigate the generalization of such properties to infinite dimensional Lie groups. We suggest that some of the theoretical objections might actually be ruled out by the practical implementation of both the LDDMM and the SVF frameworks for image registration. This leads us to a more practical study comparing the parameterization (initial velocity field) of metric and Cartan geodesics in the specific optimization context of longitudinal and inter-subject image registration. Our experimental results suggests that stationarity is a good approximation for longitudinal deformations, while metric geodesics notably differ from stationary ones for inter-subject registration, which involves much larger and non-physical deformations. Then, we turn to the practical comparison of five parallel transport techniques along one-parameter subgroups. Our results point out the fundamental role played by the numerical implementation, which may hide the theoretical differences between the different schemes. Interestingly, even if the parallel transport generally depend on the path used, an experiment comparing the Cartan parallel transport along the one-parameter subgroup and the LDDMM (metric) geodesics from inter-subject registration suggests that our parallel transport methods are not so sensitive to the

path.

4.1 Introduction

One of the main objectives of computational anatomy is to develop suitable statistical models on several subjects for the study of the anatomical variability of organs and tissues. In particular, longitudinal observations from time series of images are an important source of information for understanding the developmental processes and the dynamics of pathologies. Thus, a reliable method for comparing different longitudinal trajectories is required, in order to develop population-based longitudinal models.

Non-rigid registration is an instrument for the detection of anatomical changes on medical images, and it has been widely applied on different clinical contexts for the definition of population-based anatomical atlases [Thompson et al., 2003, Mansi et al., 2011b, Durrleman et al., 2011]. However, in case of longitudinal data, the optimal method for comparing *deformation trajectories* across different subjects is still unknown. In fact, the methods for integrating the subtle inter-subject changes into the group-wise analysis have an important impact on the accuracy and reliability of the subsequent statistical results. The aim is to preserve as much as possible the biological informations carried on by the different subjects, while allowing a precise comparison in a common geometrical space.

Among the different techniques proposed for the comparison of longitudinal trajectories [Rao et al., 2004, Bossa et al., 2010, Durrleman et al., 2009], the *parallel transport* represents a promising method which relies on a solid mathematical background. Basically, it consists in transporting the infinitesimal deformation vector across different points by preserving its properties with respect to the space geometry, such as the parallelism.

Parallel transport has been introduced in medical imaging within the LDDMM setting [Younes, 2007b, Younes et al., 2008]. LDDMM solves the image registration problem by using a Riemannian framework in which the deformations are parametrized as *diffeomorphisms* living in a suitable space, once provided an opportune right-invariant metric [Miller et al., 2002]. The registration problem is solved by computing the deformation that best matches the images with a penalization on the energy of the trajectory in the space of diffeomorphisms. The solution is given by the endpoint of a geodesic parametrized by a time-varying velocity field. This endpoint can also be parametrized by the Riemannian exponential map of the initial velocity field (or its metric dual, the momentum). The setting allows the computation of the parallel transport along geodesics at the cost of a computationally intensive scheme, and this limitation often prevents the application on high resolution images or large datasets. Moreover, this assumes that both longitudinal deformations and inter-subject transformations live in the same space of diffeomorphisms, which may have very different characteristics.

A simplified solution to the diffeomorphic registration problem was introduced with the stationary velocity field (SVF) setting [Arsigny et al., 2006]. In this case, the diffeomorphisms are one-parameter subgroups parameterized by *stationary* velocity fields through the Lie group exponential. This restriction allows an efficient numerical scheme for the computation of the deformation but it does apparently not rely on any geometric assumption on the underlying space. This implies that some important mathematical properties are not guaranteed, for instance whether the one-parameter subgroups are still geodesics or if the space is complete. In spite of this lack of knowledge, the framework was found very efficient and reliable in many application in different contexts [Mansi et al., 2011a, Lorenzi et al., 2011a, Seiler et al., 2011b]. For instance, a framework based on the Schild's Ladder has been proposed for the evaluation of the parallel transport with the SVF in [Lorenzi et al., 2011b].

In this paper we investigate the relationship between Lie groups and affine geometry and we highlight many interesting properties that provide the SVF setting with part of the geometrical solidity required. In Section 4.2 we present the relevant properties of the finite dimensional Lie groups and the relationship with the Riemannian setting for the definition of the geodesics and the parallel transport. Section 4.3 is dedicated to a discussion on the extension of the Lie group theory in the infinite dimensional case. In Section 4.4, we study the differences between the registration based on the one-parameter subgroups and on the Riemannian metric on specific registration problems. Finally, Section 4.5 focuses on the evaluation of Cartan's parallel transport of deformation vectors in the image registration context.

4.2 Differential Geometry on Lie Group

This section references the conceptual basis for the definition of the parallel transport along the one-parameter subgroups. Many details on differential geometry an Lie groups can be found in classical books like [Gallot et al., 1993, do Carmo, 1992, Helgason, 1978]. However, most results of this section are more easily found in the more modern (and quite comprehensive) presentation of differential geometry and Lie groups of Postnikov [Postnikov, 2001].

4.2.1 Basics of Lie Groups

A Lie group $\mathbb{G}$ is a smooth manifold provided with an identity element id, a smooth associative composition rule $(g,h) \in \mathbb{G} \times \mathbb{G} \mapsto gh \in \mathbb{G}$ and a smooth inversion rule $g \mapsto g^{-1}$ which are both compatible with the differential manifold structure. As such, we have a tangent space $T_g\mathbb{G}$ at each point $g \in \mathbb{G}$. A vector field $\mathbf{X}$ is a smooth function that maps a tangent vector $\mathbf{X}|_g$ to each point g of the manifold. The set of vector fields (the tangent bundle) is denoted $T\mathbb{G}$. Vector fields can be viewed as the directional (or Lie) derivative of a scalar function ϕ along the vector field at each point: $\partial_{\mathbf{X}}\phi|_g = \frac{\partial\phi(g+t\mathbf{X}|_g)}{dt}$. Composing directional derivatives $\partial_{\mathbf{X}}\partial_{\mathbf{Y}}\phi$ leads in general to a second order derivation. However, we can remove the second order terms by subtracting $\partial_{\mathbf{Y}}\partial_{\mathbf{X}}\phi$ (this can be checked by writing these expression in a local coordinate system). We obtain the Lie bracket that acts as an internal multiplication in the algebra of vector fields:

$$[\mathbf{X}, \mathbf{Y}](\phi) = \partial_{\mathbf{X}} \partial_{\mathbf{Y}} \phi - \partial_{\mathbf{Y}} \partial_{\mathbf{X}} \phi.$$

Given a group element $a \in \mathbb{G}$, we call left translation L_a the composition with the fixed element a on the left: $La : g \in \mathbb{G} \mapsto ag \in \mathbb{G}$. The differential DL_a of the left translation maps the tangent space $T_g\mathbb{G}$ to the tangent space $T_{ag}\mathbb{G}$. We say that a vector field $\mathbf{X} \in T(\mathbb{G})$ is left invariant if it remains unchanged under the action of the left translation: $DL_a \mathbf{X}_g = \mathbf{X}|_{ag}$. The sub-algebra of left-invariant vector fields is closed under the Lie bracket and is called the Lie algebra $\mathfrak{g}$ of the Lie group. Since a left-invariant vector field is uniquely determined by its value at identity through the one-to-one map $\tilde{\mathbf{X}}|_g = DL_g X$, the Lie algebra can be identified to the tangent space at the identity $T_{id}\mathbb{G}$. One should notice that any smooth vector field can be written as a linear combination of left-invariant vector fields with smooth *functional* coefficients.

Left-invariant vector fields are *complete* in the sense that their flow φ_t is defined for all time. Moreover, this flow is such that $\varphi_t(g) = g\varphi_t(id)$ by left invariance. The map $X \mapsto \varphi_1(id)$ of $\mathfrak{g}$ into $\mathbb{G}$ is called *Lie group exponential* and denoted by exp. In particular, the group exponential defines the *one-parameter subgroup* associated to the vector X and has the following properties:

- $\varphi_t(id) = \exp(tX)$, for each $t \in \mathbb{R}$;
- $\exp((t+s)X) = \exp(tX)\exp(sX)$, for each $t, s \in \mathbb{R}$.

In finite dimension, it can be shown that the Lie group exponential is a diffeomorphism from a neighborhood of 0 in $\mathfrak{g}$ to a neighborhood of id in $\mathbf{G}$.

For each tangent vector $X \in \mathfrak{g}$, the one parameter subgroup $\exp(tX)$ is a curve that starts from identity with this tangent vector. One could question if this curve could be seen as a geodesic like in Riemannian manifolds. To answer this question, we first need to define what are geodesics. In a Euclidean space, straight lines are curves which have the same tangent vector at all times. In a manifold, tangent vectors at different times belong to different tangent spaces. When one wants to compare tangent vectors at different points, one needs to define a specific mapping between their tangent spaces: this is the notion of parallel transport. There is generally no way to define globally a linear operator $\Pi_g^h : T_g\mathbb{G} \to T_h\mathbb{G}$ which is consistent with composition (i.e. $\Pi_g^h \circ \Pi_f^g = \Pi_f^h$). However, specifying the parallel transport for infinitesimal displacements allows integrating along a path, thus resulting into a parallel transport that depend on the path. This specification of the parallel transport for infinitesimal displacements is called the (affine) connection.

4.2.2 Affine Connection Spaces

An *affine connection* on $\mathbb{G}$ is an operator which assigns to each $\mathbf{X} \in T(\mathbb{G})$ a linear mapping $\nabla_{\mathbf{X}} : T(\mathbb{G}) \to T(\mathbb{G})$ such that, for each vector field $\mathbf{X}, \mathbf{Y} \in T(\mathbb{G})$, and smooth function $f, g \in C^{\infty}(\mathbb{G}, \mathbb{R})$

$$\begin{aligned} \nabla_{f\mathbf{X}+g\mathbf{Y}} &= f\nabla_{\mathbf{X}} + g\nabla_{\mathbf{Y}} \quad \text{(Linearity);} && (4.1) \\ \nabla_{\mathbf{X}}(f\mathbf{Y}) &= f\nabla_{\mathbf{X}}(\mathbf{Y}) + (\mathbf{X}f)\mathbf{Y} \quad \text{(Leibniz rule).} && (4.2) \end{aligned}$$

The *affine connection* is therefore a derivation on the tangent space which infinitesimally maps tangent vectors from one tangent plane to another. Once the manifold provided with a connection, it is possible to generalize to the manifolds the notion of "straight lines": a vector field $\mathbf{X}$ is *parallel transported* along a curve $\gamma(t)$ if $\nabla_{\dot{\gamma}(t)}\mathbf{X} = 0$ for each t. Thus, a path $\gamma(t)$ on $\mathbf{G}$ is said to be straight or *geodesic* if $\nabla_{\dot{\gamma}}\dot{\gamma} = 0$.

In a local coordinate system, the geodesic equation is a second order differential equation. Thus, given a point $p \in \mathbb{G}$ and a vector $X \in T_p\mathbb{G}$, there exist a unique geodesic $\gamma(t, p, X)$ such that at the instant $t = 0$ passes through p with velocity X [Postnikov, 2001]. We define therefore the *Affine exponential* as the application $exp : \mathbb{G} \times T(\mathbb{G}) \to \mathbb{G}$ given by $exp_p(X) = \gamma(1, p, X)$.

If, as in the Euclidean case, we want to associate to the straight lines the property of minimizing the distance between points, we need to provide the group $\mathbb{G}$ with a Riemannian manifold structure, i.e. with a metric operator g on the tangent space. In this case there is a unique connection, called *Levi-Civita connection*, which, for each $\mathbf{X}, \mathbf{Y}, \mathbf{Z} \in T(\mathbb{G})$:

- Preserves the metric, i.e. the parallel transport along any curve connecting f to g is an isometry:

$$g(\mathbf{X}, \mathbf{Y})_g = g(\Pi_g^f \mathbf{X}, \Pi_g^f \mathbf{Y})_f.$$

- Is torsion free:

$$\nabla_{\mathbf{X}}\mathbf{Y} - \nabla_{\mathbf{Y}}\mathbf{X} = [\mathbf{X}, \mathbf{Y}],$$

  thus the parallel transport is symmetric with respect to the Lie bracket.

By choosing the Levi-Civita connection of a given Riemannian metric, the affine geodesics are the length minimizing paths (i.e. classical Riemannian geodesics). However, given a general affine connection, there may not exist any Riemannian metric for which affine geodesics are length minimizing.

4.2.3 From Affine Geodesic to One-Parameter Subgroups

Given an affine connection ∇ and a vector X on $T_{id}\mathbb{G}$, we can therefore define two curves on $\mathbb{G}$ passing through id and having X as tangent vector, one given by the Lie group exponential exp and the other given by the affine exponential exp_{id}. When do they coincide?

The connection ∇ on $\mathbb{G}$ is *left-invariant* if, for each left translation L_a ($a \in \mathbb{G}$) and any vector fields $\mathbf{X}$ and $\mathbf{Y}$, we have $\nabla_{DL_a\mathbf{X}}(DL_a\mathbf{Y}) = DL_a\nabla_{\mathbf{X}}(\mathbf{Y})$. Using two left invariant vector fields $\tilde{\mathbf{X}}, \tilde{\mathbf{Y}} \in g$ generated by the tangent vectors $X, Y \in T_{id}\mathbb{G}$, we see that $\nabla_{\tilde{\mathbf{X}}}\tilde{\mathbf{Y}}$ is itself a left-invariant vector field generated by its value at identity. Since a connection is completely determined by its action on the left-invariant vector fields (we can recover the connection on arbitrary vector fields using Eq. (4.1,4.2) from their decomposition on the Lie Algebra), we conclude that each left-invariant connection ∇ is uniquely determined by a product α (symmetric bilinear operator) on $T_{id}\mathbb{G}$ through

$$\alpha(X, Y) = \nabla_{\tilde{\mathbf{X}}}\tilde{\mathbf{Y}}\Big|_{id}.$$

Notice that such a product can be uniquely decomposed into a commutative part $\alpha' = \frac{1}{2}(\alpha(X,Y) + \alpha(Y,X))$ and a skew symmetric part $\alpha'' = \frac{1}{2}(\alpha(X,Y) - \alpha(Y,X))$. The symmetric part specifies the geodesics (i.e. the parallel transport of a vector along its own direction) while the skew-symmetric part specifies the torsion which governs the parallel transport of a vector along a different direction (the rotation around the direction of the curve if we have a metric connection with torsion).

Following [Postnikov, 2001], a left-invariant connection ∇ on a Lie group $\mathbb{G}$ is a *Cartan connection* if, for any tangent vector X at the identity, the one-parameter subgroups and the affine geodesics coincide, i.e. $\exp(tX) = exp(t, id, X)$. We can see that a Cartan connection satisfies $\alpha(X, X) = 0$ or, equivalently, is purely skew-symmetric.

The one-dimensional family of connections generated by $\alpha(X, Y) = \lambda[X, Y]$ obviously satisfy this skew-symmetry condition. Moreover, the connections of this family are also invariant by right translation [Pennec and Arsigny, 2012], thus invariant by inversion also since they are already left invariant. This make them particularly interesting since they are fully compatible with all the group operations.

Among this family, three connections have special curvature or symmetric properties and are called the canonical Cartan-Schouten connections [Cartan and Schouten, 1926]. The zero curvature connections given by $\lambda = 0, 1$ (with torsion $T = -[\tilde{\mathbf{X}}, \tilde{\mathbf{Y}}]$ and $T = [\tilde{\mathbf{X}}, \tilde{\mathbf{Y}}]$ respectively on left invariant vector fields) are called *left* and *right* Cartan connections. The choice of $\lambda = 1/2$ leads to average the left and right Cartan connections. It is called the *symmetric* (or *mean*) Cartan connection. It is torsion-free, but has curvature $R(\tilde{\mathbf{X}}, \tilde{\mathbf{Y}})\tilde{\mathbf{Z}} = -\frac{1}{4}\left[[\tilde{\mathbf{X}}, \tilde{\mathbf{Y}}], \tilde{\mathbf{Z}}\right]$.

As a summary, the three canonical Cartan connections of a Lie group are (for two left-invariant vector fields):

$$\begin{aligned}
&\nabla_{\tilde{\mathbf{X}}}\tilde{\mathbf{Y}} = 0 && \text{Left (Torsion, Flat);}\\
&\nabla_{\tilde{\mathbf{X}}}\tilde{\mathbf{Y}} = \frac{1}{2}\left[\tilde{\mathbf{X}}, \tilde{\mathbf{Y}}\right] && \text{Symmetric (Torsion-Free, Curved);}\\
&\nabla_{\tilde{\mathbf{X}}}\tilde{\mathbf{Y}} = \left[\tilde{\mathbf{X}}, \tilde{\mathbf{Y}}\right] && \text{Right (Torsion, Flat).}
\end{aligned}$$

Since the three canonical Cartan connections only differ by torsion, they share the same affine geodesics which are the left and right translations of one parameter subgroups. In the following, we call them *group geodesics*. However, the parallel transport of general vectors along these group geodesics is specific to each connection as we will see below.

4.2.4 Left and Right Invariant Riemannian Metrics on Lie Groups

Given a metric $< X, Y >$ on the tangent space at identity of a group, one can propagate this metric to all tangent spaces using left (resp. right) translation to obtain a left- (resp. right-) invariant Riemannian metric on the group. In the left-invariant case we have $< DL_a X, DL_a Y >_a = < X, Y >$ and one can show [Kolev, 2007] that the Levi-Civita connection is the left-invariant connection generated by the product

$$\alpha(X, Y) = \frac{1}{2}[X, Y] - \frac{1}{2}(ad^*(X, Y) + ad^*(Y, X)),$$

if the operator ad^* verifying $< ad^*(Y, X), Z > = < [X, Z], Y >$ for all $X, Y, Z \in g$ is well defined. A similar formula can be established for right-invariant metrics using the algebra of right-invariant vector fields.

We clearly see that this left-invariant Levi-Civita connection has a symmetric part which make it differ from the Cartan symmetric connection $\alpha(X, Y) = \frac{1}{2}[X, Y]$. In fact, the quantity $ad^*(X, X)$ specifies the rate at which a left invariant geodesic and a one parameter subgroup starting from the identity with the same tangent vector X deviates from each-other. More generally, the condition $ad^*(X, X) = 0$ for all $X \in g$ turns out to be a necessary and sufficient condition to have a bi-invariant metric [Postnikov, 2001]. It is important to notice that geodesics of the left- and right-invariant metrics differ in general as there do not exists bi-invariant metrics even for simple groups like the Euclidean motions [Pennec and Arsigny, 2012]. However, right invariant geodesics can be obtained from the left invariant one through inversion: if $\phi(t)$ is a left invariant geodesic joining identity to the transformation ϕ_1, then $\phi^{-1}(t)$ is a right-invariant geodesic joining identity to ϕ_1^{-1}.

4.2.5 Parallel Transport on Cartan Connections

For the left Cartan connection, the unique fields that are covariantly constant are the *left-invariant* vector fields, and the parallel transport is induced by the differential of the left translation [Postnikov, 2001], i.e. $\Pi^L : T_p\mathbb{G} \rightarrow T_q\mathbb{G}$ is defined as

$$\Pi^L(X) \quad = \quad DL_{qp^{-1}} X. \tag{4.3}$$

One can see that the parallel transport is actually independent of the path, which is due to the fact that the curvature is null: we are in a space with absolute parallelism. Similarly, the *right-invariant* vector fields are covariantly constant with respect to the right invariant connection only. As above, the parallel transport is given by the differential of the right translation

$$\Pi^R(X) = DR_{p^{-1}q} X, \tag{4.4}$$

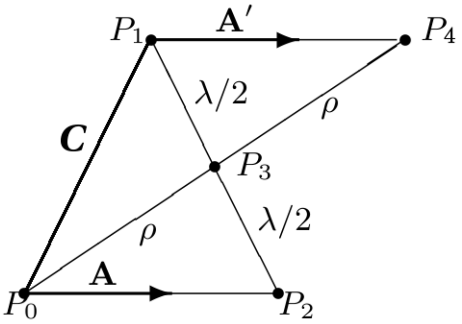

Figure 4.1: The Schild's Ladder. Given a curve C, the vector $\mathbf{A}$ on P_0 is transported to P_1 in two steps: 1) compute the *geodesic* connecting P_2 and P_1 and define the mid-point P_3, 2) compute the geodesic from P_0 to P_3 and prolongate twice to reach P_4. The tangent vector $\mathbf{A}'$ to the curve connecting P_1 and P_4 is the parallel transport of $\mathbf{A}$.

and we have an absolute parallelism as well.

Finally, the parallel transport for the symmetric Cartan connection is given by the infinitesimal alternation of the left and right transports. However, as there is curvature, it depends on the path: it can be shown [Helgason, 1978] that the parallel transport of X along the geodesic $\exp(tY)$ is:

$$\Pi^S(X) = DL_{\exp(\frac{1}{2}Y)} DR_{\exp(\frac{1}{2}Y)} X. \tag{4.5}$$

4.2.6 The Schild's Ladder: a Parallel Transport Scheme for Symmetric Connections

A more general method for parallel transport was introduced in [Misner et al., 1973] after Schild's similar constructions [KSchild, 1970]. The Schild's Ladder infinitesimally transports a vector along a given curve through the construction of geodesic parallelograms (Figure 4.1). Since this scheme relies only on geodesics, it is only valid for symmetric connections with no torsion [Kheyfets et al., 2000], in which case it provides a first order approximation of the parallel transport. Although the Schild's Ladder was known in gravitation theory for 40 years, it was apparently not used in practice as a computational tool before it was turned into an algorithm for the parallel transport of deformation vectors in [Lorenzi et al., 2011b].

4.3 A Glimpse of Lie Group Theory in Infinite Dimension

In the previous Section, we derived the equivalence of one-parameter subgroups and the affine geodesics of the canonical Cartan connections in a finite dimensional Lie group. In order to use such a framework for diffeomorphisms, we have to generalize the theory to infinite dimensions. However, defining infinite dimensional Lie groups is raising much more difficulties. This is in fact the reason why Lie himself restricted to finite dimensions. The theory was developed since the 70ies and is now an active field of research. We refer the reader to the recent books [Khesin and Wendt, 2009, Younes, 2010] for more details on this theory and to [Schmid, 2004] for a good overview of the problems and applications.

4.3.1 Infinite Dimensional Lie Groups

The basic construction scheme is to consider an infinite dimensional manifold endowed with smooth group operations. Such a Lie group is locally diffeomorphic to an infinite-dimensional vector space which can be a Fréchet space (a locally convex space which is complete with respect to a translation invariant distance), a Banach space (where the distance comes from a norm) or a Hilbert space (where the norm is derived from a scalar product). We talk about Fréchet, Banach or Hilbert Lie groups, respectively. Extending differential calculus from R^n to Banach and Hilbert spaces is straightforward, but this is not so simple for Fréchet spaces. In particular, the dual of a Fréchet space need not be Fréchet, which means that some extra care must be taken when defining differential forms. Moreover, some important theorems such as the inverse function theorem hold for Banach spaces but not necessarily for Fréchet spaces.

For instance, the set $\text{Diff}^k(\mathcal{M})$ of C^k diffeomorphisms of a compact manifold $\mathcal{M}$ is a Banach manifold and the set of Sobolev H^s diffeomorphisms $\text{Diff}^s(\mathcal{M})$ is a Hilbert manifold (if $s > dim\mathcal{M}/2$). However, these are no-classical "Lie groups" since one looses derivatives when differentiating the composition and inversion maps. To obtain the complete smoothness of the composition and inversion maps, one has to go to infinity, but the Banach structure is lost in the process [Schmid, 2004, p.12] and we are left with $\text{Diff}^\infty(\mathcal{M})$ being only a Fréchet Lie group. Some additional structure can be obtained by considering the sequence of $\text{Diff}^k(\mathcal{M})$ spaces as a succession of dense inclusions as k goes to infinity: this the Inverse Limit of Banach (ILB)-Lie group setting. Likewise, the succession of dense inclusions of Sobolev H^s diffeomorphisms give rise to the Inverse Limit of Hilbert (ILH)-Lie group setting.

4.3.2 General Groups of Diffeomorphisms

As the diffeomorphisms groups considered are Fréchet but not Banach, the usual setting of infinite dimensional Lie groups is the general framework of Fréchet manifolds. This implies that many of the important properties which are true in finite dimension do not hold any more for general infinite dimensional Lie groups [Schmid, 2010].

First, there is no implicit or inverse function theorem (except Nash-Moser type theorems.) This implies for instance that the log-map (the inverse of the exponential map) may not be smooth even if the differential of the exponential map is the identity.

Second, the exponential map is not in general a diffeomorphism from a neighborhood of zero in the Lie algebra onto a neighborhood of the identity in the group. This means that it cannot be used as a local chart to work on the manifold. For instance in $\mathrm{Diff}^s(\mathcal{M})$, in every neighborhood of the identity there exists diffeomorphisms which are not the exponential of an H^s vector field. A classical example of the non-surjectivity of the exponential map is the following function in $\mathrm{Diff}(\mathbb{S}^1)$ [Milnor, 1984]:

$$f_{n,\varepsilon}(\theta) \quad = \quad \theta + \pi/n + \varepsilon \sin^2(n\theta). \tag{4.6}$$

This function can be chosen as close as we want to the identity by opportunely dimensioning ε and θ. However, it can be shown that it cannot be reached by any one-parameter subgroup, and therefore the Lie group exponential is not a local diffeomorphisms of $\mathrm{Diff}(\mathbb{S}^1)$.

This example is quite instructive and shows that this theoretical problem might actually be a very practical advantage: the norm of the k-th derivative of $f_{n,\varepsilon}$ is exploding when k is going to infinity, which shows that we would rather want to exclude this type of diffeomorphisms from the group under consideration.

4.3.3 Theoretical Background of Diffeomorphic Image Registration

In the Large Deformation Diffeomoprhic Metric Mapping (LDDMM) framework [Younes, 2010], a different construction is leading to a more restricted subgroup of diffeomorphisms which is more rational from the computational point of view. One first chooses a Hilbert norm on the Lie Algebra which turn it into an admissible Hilbert space. Admissible means that it can be embedded into the space of vector fields which are bounded and vanishing at infinity, as well as all the first order derivatives. Typically, this is a Sobolev norm of a sufficiently high order. Then, one restricts to the subgroup of diffeomorphisms generated by the flow of integrable sequences of such vector fields for a finite time. To provide this group with a Riemannian structure, a right invariant metric is chosen. The reason for choosing right translation is that it is simply a composition which does not involve a differential operator as for the left translation. On can show that the group provided with this right-invariant metric is a complete metric space: the choice of the norm on the Lie algebra is specifying the subgroup of diffeomorphisms which are reachable, i.e. which are at a finite distance.

4.3.4 The Stationary Velocity Fields (SVF) framework

In [Arsigny et al., 2006], Arsigny proposed to parameterize deformations by the exponential (i.e. the flow) of stationary velocity fields [Arsigny et al., 2006]. The fact that the flow in an autonomous ODE allows us to generalize efficient algorithms such as the scaling and squaring algorithm: given an initial approximation $\exp(\delta Y) = id + \delta Y$, the exponential of a SVF Y can be efficiently and simply computed by recursive compositions:

$$\exp(Y) = \exp\left(\frac{Y}{2}\right) \circ \exp\left(\frac{Y}{2}\right) = \left(\exp\left(\frac{Y}{2^n}\right)\right)^{2^n}.$$

A second algorithm is at the heart of the efficiency of the optimization algorithms with SVFs: the Baker-Campbell-Hausdorff (BCH) formula [Bossa et al., 2007] tells us how to approximate the log of the composition:

$$\begin{aligned} BCH(X, \delta Y) &= \log(\exp(X) \circ \exp(\delta Y)) \\ &= X + \delta Y + \frac{1}{2}[X, \delta Y] + \frac{1}{12}[X, [X, \delta Y]] + \dots . \end{aligned}$$

In order to have a well-posed space of deformations, we need to specify on which space is modeled the Lie algebra, as previously. This is the role of the regularization term of the SVF registration algorithms [Vercauteren et al., 2008, Hernandez et al., 2009] or of the spline parameterization of the SVF in [Ashburner, 2007b, Modat et al., 2011]: this restricts the Lie algebra to the sub-algebra of sufficiently regular velocity fields. The subgroup of diffeomorphisms considered is then generated by the flow of these stationary velocity fields and their finite composition. So far, the theoretical framework is very similar to the LDDMM setting and we can see that the diffeomorphisms generated by the one-parameter subgroups (the exponential of SVFs) all belong to the group considered in the LDDMM setting, provided that we model the Lie algebra on the same admissible Hilbert space. As in finite dimension, the affine geodesics of the Cartan connections (group geodesics) are metric-free (the Hilbert metric is only used to specify the space on which is modeled the Lie Algebra) and generally differ from the Riemannian geodesics of LDDMM.

When modeling the Lie algebra on a reproducing kernel Hilbert space (RKHS) with a real analytic kernel (typically a Gaussian Kernel), the Lie algebra is stable under the bracket, which is necessary for the classical Lie group theory. If we could show that the adjoint operator is uniformly bounded with a sufficiently small bound, then we would expect the BCH series to be convergent. Having such a BCH-Lie group would already be sufficient to justify the optimization steps performed in the SVF registration framework.

However, it is well known that the subgroup of diffeomorphisms generated by this Lie algebra is significantly larger than what is covered by the group exponential. Indeed, although our affine connection space is geodesically complete (all geodesics can be continued for all time without hitting a boundary), there is no Hopf-Rinow theorem which state that any two points can be joined by a geodesic (metric completeness). Thus, in general, not all the elements of the group $\mathbb{G}$ may be reached by the one-parameter subgroups. An example in finite dimension is given by $SL(2)$.

However, this might not necessarily results into a problem in the image registration context since we are not interested in recovering "all" the possible diffeomorphisms, but only those which lead to admissible anatomical transformations. For instance, the diffeomorphism on the circle defined above at Eq. (4.6) cannot be reached by any one-parameter subgroup of $\mathbb{S}^1$. However, since

$$\lim_{k\to\infty} \|f_{n,\varepsilon}\|_{H^k} \to \infty,$$

this function is not well behaved from the regularity point of view, which is a critical feature when dealing with image registration.

In practice, we have a spatial discretization of the SVF (and of the deformations) on a grid, and the temporal discretization of the time varying velocity fields by a fixed number of time steps. This intrinsically limits the frequency of the deformation below a kind of "Nyquist" threshold, which prevents these diffeomorphisms to be reached anyway both by the SVF and by the "discrete" LDDMM frameworks. Therefore, it seems more importance to understand the impact of using stationary velocity fields in registration from the *practical* point of view, than from the theoretical point of view, because we will have *in fine* to deal with the unavoidable numerical implementation and relative approximation issues.

4.4 Practical Differences between Metric and Group Geodesics in Registration

In this Section, we investigate the practical differences between metric and group geodesics, by applying the SVF and LDDMM image registration settings on common data. In this case, we are interested in the differences between the estimated diffeomorphisms and the related tangent parametrization.

We investigate two different scenarios: *longitudinal* and *inter-subject* registration problems. In the former case the registration aims at retrieving the small differences occurring on the same subject after two subsequent imaging session, most likely due to precise biological processes. In the latter case, the differences are given by the large variability among different subjects, with potential structural and topological changes. In this case, even if there might not exist real one-to-one correspondences, the diffeomorphic constraint is important in term of smoothness and reliability of the represented deformation. In the following the SVF and LDDMM settings will be provided by the log-Demons and the AtlasWerk registration algorithms.

4.4.1 Log-Demons

The symmetric log-domain diffeomorphic Demons (or log-Demons) [Vercauteren et al., 2008] estimates a diffeomorphic deformation parametrized by a SVF. The log-Demons alternates the estimation of unconstrained correspondences (encoded through the exponential of a SVF v_c) that optimize the image similarity measure, and the estimation of the transformation parameters (a SVF v) that best explains the correspondence field using a penalized least-squares approach. The regularity criterion is an infinite order differential quadratic forms (Q_k) of the velocity field [Cachier and Ayache, 2004],

$$\begin{aligned} Reg(v) &= \|v_c - v\|^2 + \sum_{k=1}^{\infty} \frac{Q_k(v)}{\sigma_t^{2k}} \\ &\simeq \|v_c - v\|^2 + \frac{\sigma^2}{2}\|\nabla v\|^2 + \frac{\sigma^4}{4}\|\nabla^2 v\|^2 + \ldots, \end{aligned}$$

where we chose $\sigma_t^2 = 2/\sigma^2$ so that the optimum is explicitly obtained through a Gaussian convolution of smoothing parameter σ [Mansi et al., 2011a]. The Lie group exponential is efficiently implemented by the scaling and squaring computational scheme. An additional (so-called fluid) regularization step is often performed when updating the correspondences in addition to the above elastic-like penalization.

In the following experiments we used the regularization parameters $\sigma_{fluid} = 0.5$ and $\sigma_{el} = 1.5$, maximum update step length $\sigma_x = 2$ voxels, with a multi-resolution scheme of 100 and 50 iterations at coarser and finer level respectively. This choice leads to a reasonable compromise between image matching and smoothness of the deformation in both longitudinal and inter-subject settings, as already tested in several previous experiments. The average computational time for the registration of a couple of brain images (image resolution 182x218x182, voxel size 1x1x1) is 25 minutes on a AMD Opteron dual core 2000Mhz.

4.4.2 AtlasWerks

The AtlasWerks suite [Atlaswerks, 2007] is an implemention of the Large Deformation Diffeomorphic Metric Mapping (LDDMM) framework. The algorithm minimizes the sum of an image similarity metric and an elastic regularization term which measures the energy of the trajectory deforming one image into the other. This formulation ensures that the optimum trajectory is a geodesic evolution equation, which means that the path is completely defined by the initial tangent vector or, equivalently, by the initial momentum [Joshi and Miller, 2000, Joshi et al., 2004b]. The energy of the geodesic is measured by the norm of the initial vector $\|v_0\|^2 = \|\mathbf{L}v_0\|^2_{L_2}$ (or equivalently by its integral along the geodesic path). The differential operator $\mathbf{L} = \gamma - \alpha\nabla^2 - \beta\nabla(\nabla\cdot)$ is controlled by three parameters α, β and γ responsible respectively for the smoothness and the compressibility of the deformation, and trade-off between matching and regularity terms. This energy corresponds to a Sobolev H^2 norm on the Lie Algebra, which is weaker than the one imposed by the log-Demons regularization: roughly, the normalized weight α/γ of the first order term could be compared to the weight $\sigma^2/2$ of the log-Demons while β/γ should be compare to zero. The same comparison is also valid for the second order term.

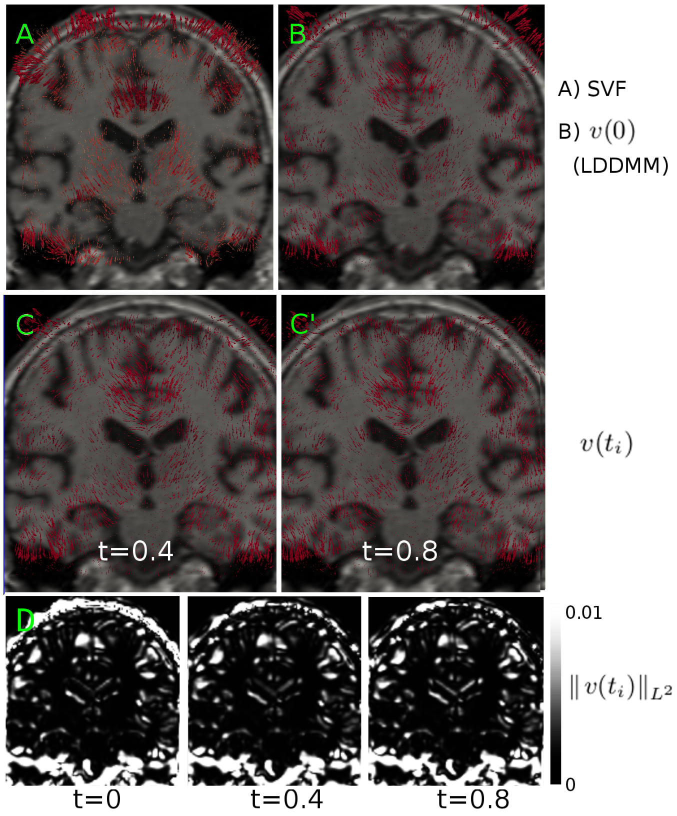

Figure 4.2: Intra-subject registration. Tangent representation for the intra-subject longitudinal deformation estimated by A) the SVF, and B) the LDDMM (initial tangent vector $v(0)$) settings. C,C') LDDMM time varying velocity field $v(t_i)$ at time points $t_i = 0.4$ and 0.8, and D) associated magnitude measured by the L^2 norm.

Higher order terms are not penalized by AtlasWerks while they are increasingly penalized with the log-Demons.

The AtlasWerks suite requires to set-up different registration parameters and, in order to obtain results compatible with those given by the Demons registration, we finally chose the ones which lead to the maximum SSD similarity with the Demons results (not shown). Therefore, the following experiments were performed by setting the fluid registration parameters as follow: $\alpha = 1.5, \beta = 0.01, \gamma = 3$ and $\sigma = 15$, with a multi-resolution scheme of 100 and 50 iterations and the geodesic path computed on 5 time points. These parameters seems of the same order than the log-Demons one ($\alpha/\gamma = 0.5$ versus $\sigma^2/2 = 1$, $\beta/\gamma = 0.003$ versus 0). In the following experiments on brain images the average computational time was of 150 minutes.

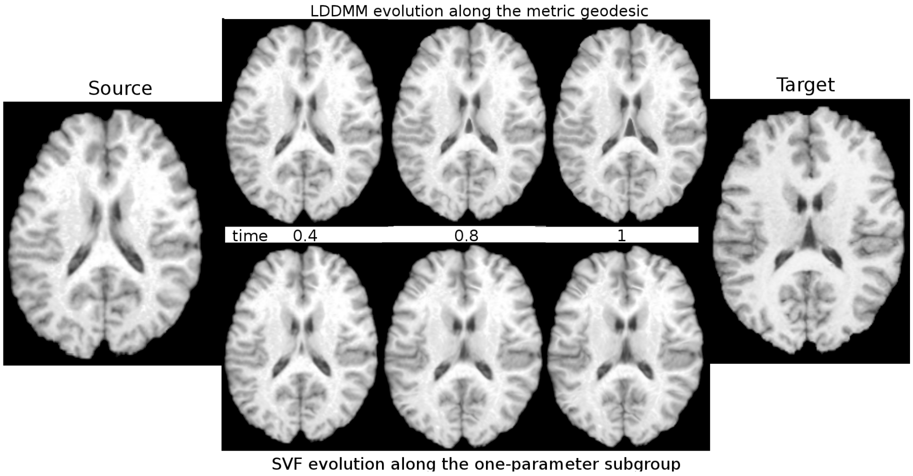

Figure 4.3: Deformation trajectory for the inter-subject warp estimated by the LDDMM (top sequence), and the SVF (bottom sequence).

4.4.3 Longitudinal Registration

We chose the one year follow-up brain images from 5 subjects affected by Alzheimer's disease from a clinical study presented elsewhere [Galluzzi et al., 2009]. The MR images were acquired with a 1.0 Tesla Philips Gyroscan. The T1-weighted scan was acquired in the sagittal plane with a gradient echo techniques as follows: TR= 20 ms, TE= 5 ms, flip angle= 30°, field of view= 220 mm, acquisition matrix= 256x256, slice thickness= 1.3 mm. After a standard preprocessing pipeline consisting in affine registration and histogram matching, the images were diffeomorphically registered with the LDDMM and the SVF algorithms.

In Figure 4.2, top row, we can see an example of the different tangent representations for the estimated deformations. The two methods retrieve similar deformation patterns, both mapping to the cortical areas, hippocampus and white matter.

In this example related to small longitudinal changes, the time-varying representation does not exhibit relevant changes in time concerning the direction of the deformation vectors (Figure 4.2, row C,C'), and the magnitude (Table 4.2), here evaluated as the L^2 norm of the velocity fields. In fact, as shown in Figure 4.2, row D, and in Table 4.2, the variation of the time-varying velocity fields are minimal in terms of location and magnitude of the forces.

In Table 4.1 we can see that both Demons and LDDMM provide similar results for the matching in terms of the SSD. Interestingly, the similarity between the deformed images obtained with the two registration methods is higher than the similarity of the deformed images with the target. This example suggests that, in the small deformation setting, both stationary and time-varying parameterizations lead to similar results, and that the LDDMM velocity field stays barely constant during the evolution.

4.4.4 Inter-subject Registration

In this experiment, the two methods were employed to register a set of 10 T1 brain scans from the LPBA40 dataset of the Laboratory of Neuro Imaging (LONI) at UCLA[1][Shattuck et al., 2008]. A reference subject was chosen among the dataset, and the other brain images underwent affine registration and histogram matching prior to non-rigid registration with the SVF and the LDDMM frameworks.

In Figure 4.4 we can observe an example of the estimated tangent representation of the deformations. Contrarily to the intra-subject case, the variation in orientation and magnitude of the time-varying velocity fields is here more pronounced (rows C-C', D), and the same result is quantified by the increased non-stationarity of the LDDMM velocities (Table 4.2). Moreover, the velocity field appears more localized

---

[1] http://www.loni.ucla.edu/Atlases/LPBA40

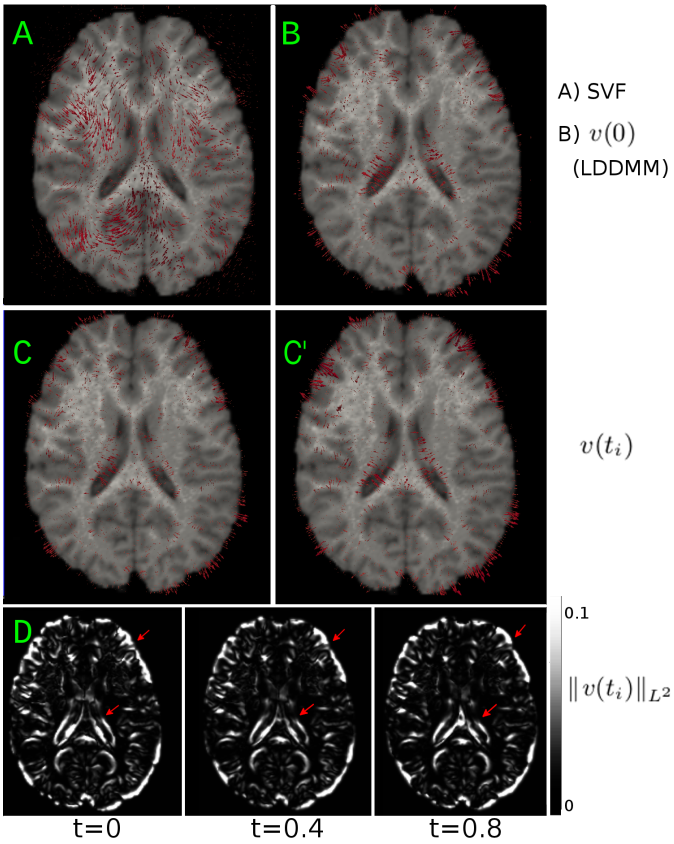

Figure 4.4: Inter-subject registration. Tangent representation for the inter-subject deformation estimated by A) the SVF, and B) the LDDMM (initial tangent vector $v(0)$) settings. C,C') LDDMM time varying velocity field $v(t_i)$ at time points $t_i = 0.4$ and 0.8, and D) associated magnitude measured by the L^2 norm. We notice the variation in magnitude and location of the time varying velocity.

than for the SVF. This could come from the regularization of the higher differential terms in the log-Demons for the SVF. However, we also know that the optimal momentum for LDDMM has to be aligned with the gradient of the image and is thus localized on the edges. This second reason is probably more important although it remains to be quantified.

Table 4.3 (first row) shows the average L^2 distance between the displacement fields obtained with the two different frameworks. As already described before, the SVF and LDDMM displacements are closer in the longitudinal setting than in inter-subject. Figure 4.3 shows the estimated evolution from the source to the target image under the two registration settings. As can be seen for instance for the deformation on the ventricles, the two methods perform here differently. However, as in the experiments on the longitudinal registration, the two methods provide similar results in terms of resulting SSD (Table 4.1).

Clearly these experiments do not aim to provide comparisons in terms of accuracy and precision which notably depend on the opportune tuning of the registration parameters. However it is interesting to notice the very similar result for the intensity matching in spite of the rather different parameterizations estimated by the two methods.

Table 4.1: Average SSD (standard deviation) for the different tests in the longitudinal and the inter-subject registration settings. The SVF method performs very similarly to the LDDMM, as also shown by the low SSD between the resulting warped images (Row 2). Moreover, the exponential given by the "scaling and squaring" numerical scheme of the initial LDDMM tangent vector generally provides lower matchings with the target images, tough the resulting warped images are still consistent with the LDDMM ones, especially in the longitudinal setting (Rows 4-5).

	Longitudinal	Inter-Subject
SVF-Target	256(37)	355(39)
SVF-LDDMM	139(102)	122(70)
LDDMM-Target	284(90)	372(35)
ScSq-LDDMM	162(105)	368(62)
ScSq-Target	514(111)	950(98)

4.4.5 Lie Group vs Riemannian Exponential of the Same Initial Vector Field

Finally, we investigated the practical differences between the Lie group exponential and the Riemannian one, by comparing the relative results in terms of vector field exponentiation. For this purpose, the Lie group exponential implemented by the scaling and squaring algorithm was applied on the initial vector field $v(0)$ provided by the LDDMM, and the resulting warped image was compared to the LDDMM

Table 4.2: Evaluation of the non-stationarity of the LDDMM velocity fields. Average (standard deviation) change in the L^2 norm $\frac{\int_\Omega \|v(0)-v(t)\|^2_{L^2}}{\int_\Omega \|v(0)\|^2_{L^2}}$ for the sampled LDDMM time varying velocity fields in the inter-subject and longitudinal settings. As qualitatively shown in Figure 4.2 and 4.4, the LDDM evolution is more stationary in the longitudinal setting.

Relative distance from $v(0)$		
	Longitudinal setting	Inter-Subject setting
$v(0.2)$	0.026 (0.020)	0.007 (0.013)
$v(0.4)$	0.077 (0.088)	0.046 (0.027)
$v(0.6)$	0.13 (0.125)	0.283 (0.213)
$v(0.8)$	0.208 (0.160)	1.6 (1.23)

Table 4.3: Differences between LDDM and SVF displacements. Relative average L^2 distance (standard deviation) $\frac{\int_\Omega \|\varphi_{LDDMM}-\varphi_{SVF}\|^2_{L^2}}{\int_\Omega \|\varphi_{LDDMM}|^2_{L^2}}$ between the displacement fields obtained in the different settings: inter-subject vs longitudinal registration, and Lie group vs Riemannian exponentials on the LDDMM initial tangent vector. As for the SSD on the resampled images (Table 4.1), the SVF method performs more similarly to the LDDMM in the longitudinal setting. Moreover, in this setting the "scaling and squaring" Lie group exponential is closer to the Riemannian one.

	Longitudinal	Inter-Subject
SVF-LDDMM	674 (4.66)	5692 (1322)
ScSq-LDDMM	1.93 (1.63)	39.3 (58.8)

one, which is obtained from the geodesic evolution equation.

Figure 4.5 shows the result for both intra and inter-subject registration. In the longitudinal case (top row), the Lie group exponential generates results close to the LDDMM ones, as shown by the low intensity differences between the respective warped images. This is confirmed at the group level (Table 4.1), where the average SSD between the two exponential methods is lower than the one resulting from the LDDMM registration (162 vs 284), even though the Lie group exponential led to increased average intensity mismatch with respect to the target(514). In the inter-subject case the differences are more pronounced (Figure 4.5, bottom row): the Lie group exponential of the initial tangent vector produces a deformation that differs from the the original LDDMM one (for instance in the ventricles and around the cortex). This is reflected at the group level by the resulting similarities (Table 4.1), where the average SSD between the exponential methods is comparable to the one of the inter-subject registration LDDMMM-Target (368 vs 372), and the mismatch Lie Group Exponential-Target is sensitively higher (950). The result is confirmed

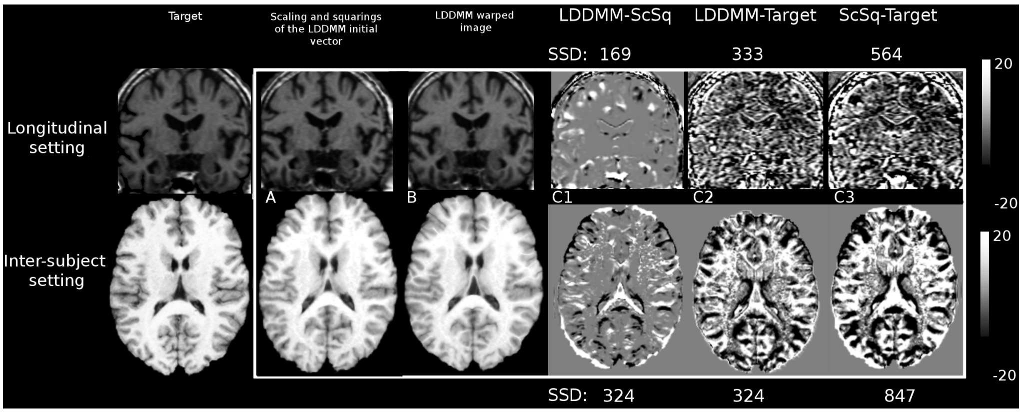

Figure 4.5: Lie group exponential (scaling and squaring) applied to the LDDMM initial vector for the intra and the inter-subject registration. From left to right: Target image, A) resulting warped source image with the scaling and squaring, B) warped source imaged with the LDDMM, and differences between C1) LDDMM and Scaling and Squaring warped images, C2) LDDMM warped and target images and C3) scaling and squaring warped and target images. We note that although the scaling and squaring provides worse matching with respect to the target, the resulting warped image is still close to the LDDMM one.

when considering the relative difference between the L^2 norm of the displacements given by two exponentials (Table 4.3).

This experiment is a supporting argument for the stationary nature of the longitudinal deformations, where the scaling and squaring of the tangent vector lead to a satisfactory description of the morphological changes. Thus, for small deformations, the metric geodesics seems to correspond to the one-parameter subgroups. A rather different scenario is given by the inter-subject registration problem, where the evolution of the momentum for the geodesic evolution cannot be neglected and produces a different representation of the deformation from the one from the one-parameter subgroup.

4.5 Cartan Parallel Transport along Group Geodesics in Practice

In group of diffeomorphisms, the left and right translations are respectively $L_g \exp(X) = g \circ \exp(X)$, and $R_g \exp(X) = \exp(X) \circ g$. Their first order Taylor expansion leads to

$$DL_g(X) = Dg \cdot X \qquad DR_g(X) = X \circ g,$$

where $Dg(x) = \partial g(x)/\partial x$ is the usual Jacobian matrix. We can therefore provide an *explicit closed form formula* for the parallel transport with respect to the canonical

Cartan connections. In particular, if X is a vector field to be transported along the one-parameter subgroup $\exp(tY)$ we have:

$$\begin{aligned}
\Pi^L_Y(X) &= D\exp(Y)\cdot X, && (4.7)\\
\Pi^R_Y(X) &= X\circ\exp(Y), && (4.8)\\
\Pi^S_Y(X) &= D\exp(\frac{Y}{2})\cdot\left(X\circ\exp(\frac{Y}{2})\right). && (4.9)
\end{aligned}$$

4.5.1 Computing the Jacobian of the Deformation

From the computational point of view, we notice that among the three transport methods, Π^R requires the simple resampling of the velocity field by the transformation, while both Π^L and Π^S involve the computation of the Jacobian matrix of the exponential. The presence of these first order differential terms is raising numerical accuracy problems when the Jacobian matrix is computed by finite differences of the displacement field sampled on the image grid. In the case of large deformations, the displacement field is undergoing high frequency changes and its sampling in the finite difference scheme is notably error prone.

We can alleviate this numerical problem by taking advantage of the properties of the one-parameter subgroups. Rather than computing directly the Jacobian $D\exp(Y)$ using finite differences on the final displacement field, we can derive a recursive scheme from the following property:

$$\exp\left(\frac{nY}{N}\right) = \exp\left(\frac{(n-1)Y}{N}\right)\circ\exp\left(\frac{Y}{N}\right)$$

Starting from the approximation $D\exp(Y/N)\simeq \mathrm{Id}+\frac{1}{N}DY$ for a suitable scaling factor N, we have the recursive formula (for $n=2$ to N):

$$D\exp\left(\frac{nY}{N}\right) = D\exp\left(\frac{(n-1)Y}{N}\right)\Big|_{\exp(\frac{Y}{N})}\cdot D\exp\left(\frac{Y}{N}\right) \qquad (4.10)$$

Thanks to this recursive scheme, the Jacobian is computed by finite differences on a low frequency displacement field, which sampling does not raise numerical issues, and the matrix valued image of Jacobian matrices is recursively resampled and multiplied along the one-parameter subgroup. Thus, the scheme avoids the sampling of a high frequency field, at the cost of multiple interpolations. Here, interpolating derivatives (Jacobian matrices) instead of displacements is giving a very important gain in numerical accuracy. Although the smoothness of the interpolation scheme (trilinear, spline, etc.) may be thought of as having an important impact on the final computational accuracy, we use simple trilinear interpolation in the sequel.

4.5.2 Schild's Ladder Implementation for SVF

The Schild's Ladder scheme was introduced in the SVF setting in [Lorenzi et al., 2011b] to parallel transport longitudinal trajectories along inter-subject deformations. When applied to the symmetric Cartan connection, we can take advantage of the symmetry properties of the parallelogram to replace the computation of the geodesics with the composition of group exponentials, and the initial tangent vector of the resulting geodesic can be efficiently approximated with the BCH formula. This leads to a computationally efficient and numerically stable method where the parallel transport of a vector X along the trajectory $\exp(tY)$ is

$$\Pi^{Y}_{Schild}(X) = X + t[Y,X] + \frac{t^2}{2}[Y,[Y,X]] + O(t^3),$$

with $[Y,X] = DY \cdot X - DX \cdot Y$. Notice that here we take the spatial gradient of the SVFs Y and X while the previous transport schemes differentiate the exponential $\exp(Y)$. This might make an important numerical difference.

4.5.3 Synthetic Experiment on a Simplified Geometry

Morphometric studies often investigate pathological phenomena described by the loss of matter, which is modeled by compressible deformations and quantified by scalar indices of volume change, such as the Jacobian determinant or its logarithm. Therefore it is important to preserve these measures when normalizing to a reference space in group-wise studies of deformation trajectories. In this section we propose a simple example aimed at testing the ability of the proposed Cartan parallel transport techniques to preserve the atrophy trajectory simulated on a simplified geometry.

A synthetic progression of longitudinal atrophy was simulated on a 3D gray matter sphere S_0 enclosing a white/black matter region. The atrophy was simulated by decreasing the gray layer thickness on four subsequent time points to generate the sequence S_i, $i = 1 \dots 4$ (Figure 4.7). The longitudinal trajectories of deformation fields $\exp(X^i)$ were then evaluated by registering the images to the baseline with

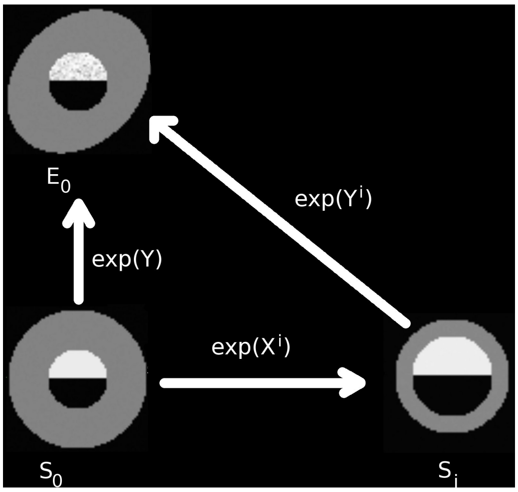

Figure 4.6: Synthetic example: Intra and inter-subject variations from the sphere source space to the ellipsoid target space with related deformations.

Table 4.4: Average measures of changes on the gray matter layer. Top-row (Source Space): changes measured on the reference sphere at each time point $1-4$. Bottom-rows: changes measured from the transported longitudinal deformations on the ellipsoid. For the conjugate action it was not possible to compute the L^2 Norm of the associated stationary velocity field, since it acts on deformation fields.

	L^2 Norm				log Jacobian			
	1	2	3	4	1	2	3	4
Source Space	2.97	9.85	22.68	44.62	-4.77	-9.54	-14.76	-19.14
Π^L	3.02	9.57	22.14	42.32	-5	-9.82	-14.88	-20.43
Π^R	**2.94**	**10**	**22.81**	**44.58**	-4.70	**-9.36**	-14.51	-19.18
Π^S	3.3	11.17	25.7	50.37	-5.74	-11.2	-17.13	-23.65
Schild's Ladder	3.65	10.74	24.3	51.49	**-4.83**	-9.86	**-14.65**	**-19.11**
Conjugate	/	/	/	/	-2.6	-5.5	-9.18	-13.93

	Jacobian				Elastic energy			
	1	2	3	4	1	2	3	4
Source Space	0.68	0.47	0.35	0.37	3.47	3.93	4.5	5.23
Π^L	**0.69**	0.51	0.43	0.45	3.51	4.01	4.67	5.53
Π^R	**0.69**	**0.49**	**0.36**	**0.37**	**3.49**	**3.9**	**4.44**	**5.15**
Π^S	0.67	0.50	0.42	0.48	3.58	4.2	4.99	6.05
Schild's Ladder	0.71	0.51	0.45	0.49	3.57	4.14	4.84	6.21
Conjugate	0.8	0.63	0.47	0.32	3.43	3.83	4.36	5.04

the log-Demons algorithm [Vercauteren et al., 2008]. The sequence of deformations $\exp(X^i)$ was then transported on a target ellipsoidal geometry E_0 along the inter-subject deformation $\exp(Y)$ such that $\exp(Y) * S_0 = E_0$ (Figure 4.6). The transport methods that we tested were:

- Right Cartan connection (right translation) Π^R;
- Left Cartan connection (left translation) Π^L and Cartan symmetric connection Π^S implemented with the recursive scheme;
- Conjugate action
  $Conj(\exp(X^i)) = \exp(Y)\exp(X^i)\exp(Y)^{-1}$;
- the Schild's Ladder, which operates along the "diagonal" inter-subject deformations $\exp(Y^i)$ such that $\exp(Y^i) * S_i = E_0$ (Figure 4.6)

The methods were quantitatively assessed by evaluating the features of interest in the ellipsoidal gray layer: the average L^2 norm of the transported SVF, the Jacobian determinant, log-Jacobian determinant and elastic energy of the associated deformation fields. Since we are interested in preserving the interesting features of the transported trajectories, the transported quantities were compared to the original values in the reference sphere space. Moreover, the stability of the methods was tested by checking the scalar spatial maps associated to the features (this involves resampling).

Table 4.4 shows the accuracy of the transport methods in the preservation of the measure of changes in the gray matter layer. Among the different methods, the transport Π^R was the most accurate in preserving the average measures, while the Schild's Ladder performed better on the log-Jacobian.

From the inspection of the related scalar log-Jacobian maps (Figure 4.7), the transport Π^L is the less stable and leads to noisy maps. Moreover, we notice that the areas of expansions does not fit the boundary of the ellipsoid. On the other hand, the transport Π^R leads to smooth maps of changes, consistent with the target geometry, while the transport Π^S lies "in between", as one could reasonably expect. The Schild's Ladder leads to smooth maps as well, although the inner spherical shape seems corrupted for higher deformations. This could explain the lower performance on the quantitative measurements for the time points 3 and 4. Finally, the log-Jacobian maps associated to the conjugate actions are smooth but fail to preserve the target ellipsoidal geometry, especially for the higher deformations.

4.5.4 Real Longitudinal Changes in Alzheimer's Disease

In this section the parallel transports Π^L,Π^R, Π^S, and the Schild's Ladder were applied to an example of real longitudinal brain atrophy. Baseline and follow-up scans from a subject affected by Alzheimer's disease were registered with the Symmetric log-Demons algorithm. Further details on the image acquisition protocol are given in section 4.4.3. The longitudinal atrophy encoded by the SVF was then transported along the inter-subject registration on a different reference anatomical space (Figure 4.8).

As in the synthetic experiment, all the above methods provide results that are consistent with the original trajectory. As already seen in the synthetic case, the transport Π^L seems to introduce some noise which lead to increased velocities (for instance in the posterior cingulate and on the left side of the cortex), which indicates that numerical issues still play a central role. Interestingly, we notice in the posterior part of the ventricles in the source space a rotational movement pointing to the medial axis of the brain which is captured by Π^L, Π^S, and by the Schild's Ladder, but which seems missing in Π^R. This observation suggests that the simple resampling of the vector field might provide only a partial representation of the deformation, and is potentially missing some features of interest for a subsequent analysis.

4.5.5 Cartan Parallel Transport Along Metric vs Group Geodesics

Finally, we investigate the differences in transporting a longitudinal trajectory along different paths, namely the LDDMM metric geodesics and the one-parameter subgroups that best register two images. We restrict our study to the parallel transport of the Cartan connections. The LDDMM parallel transport could be computed by the equations of Jacobi fields [Younes, 2007b] or could be approximated using the

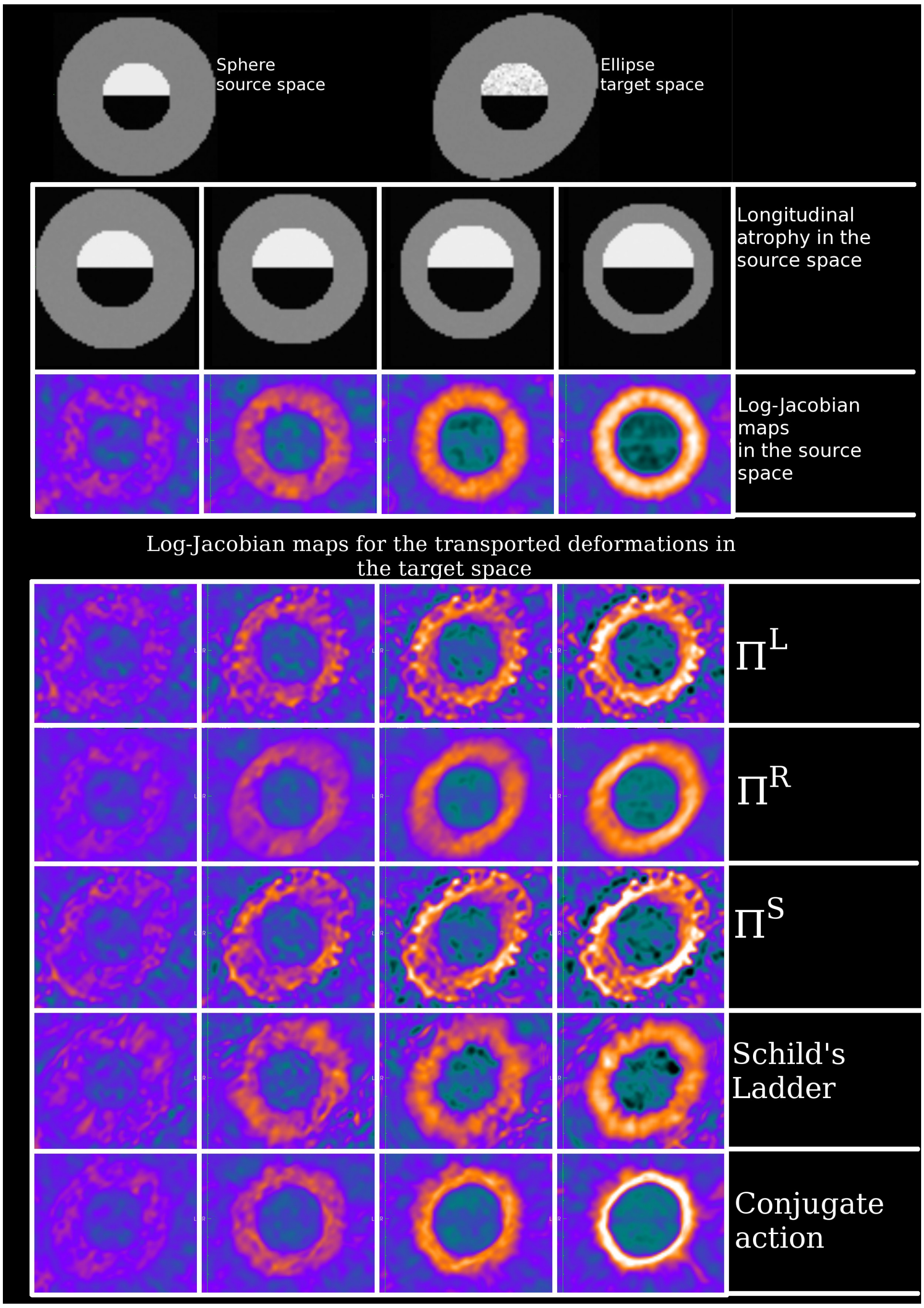

Figure 4.7: Top row: Spherical source and ellipsoidal target geometrical references. From top to bottom: Longitudinal atrophy sequence in the spherical space, associated log-Jacobian determinant scalar maps, and log-Jacobian determinant maps associated to the different methods of transport.

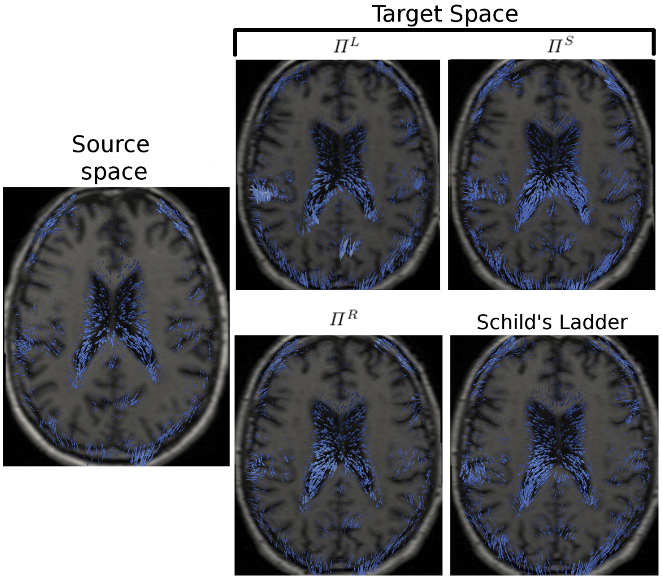

Figure 4.8: Parallel transport of longitudinal atrophy. Longitudinal ventricular expansion in the source space and related parallel transport given by the different methods.

Schild's ladder algorithm by explicitly computing metric geodesics at each step of the ladder. However, the computational complexity is much worse because the simplifications used for the group exponential with the BCH in [Lorenzi et al., 2011b] are not valid any more for Riemannian geodesics. Thus, we focus here on the comparison of the different type of Cartan parallel transport along group and metric geodesics without comparing LDDMM versus Cartan parallel transports.

From the geometrical point of view, parallel transporting a vector along different trajectories generally leads to different parallel vectors (Figure 4.9). However, the similarity of the deformation trajectories evaluated by different methods could lead to according results. Moreover, the practical application to the image registration might hide the effect of these theoretical issues. Evaluating the impact of the choice of the trajectory is therefore of interest to understand the effect of different parameterizations and to generalize the transport schemes to diverse registration settings.

We use here the Synthetic example of the Paragraph 4.5.3. The spherical source space was registered to the target ellipse with the Demons and the AtlasWerks methods. The related tangent parameterization define two different paths in the space of diffeomorphisms, respectively the one-parameter subgroup associated to the SVF, and the metric geodesic associated to the time varying velocity field $v(t)$. In the LDDMM case, the time-varying trajectory is sampled in time to give a series of n stationary vectors $v_i = v(t_i), i = 1, \dots, n$, and the final deformation φ is generated from the composition:

$$\varphi \;=\; \exp(\frac{v_{n-1}}{n}) \circ \exp(\frac{v_{n-2}}{n}) \ldots \circ \exp(\frac{v_0}{n})$$

Therefore we decompose here the time varying process into successive stationary ones, in order to apply the same methods derived from the Lie group theory. Thus, the parallel transport methods illustrated in the previous section can be applied on each trajectory v_i to iteratively transport a longitudinal trajectory along the metric geodesic.

Figure 4.10 shows the resulting vectors transported from the sphere to the ellipse space along the SVF one-parameter subgroup and the LDDMM metric geodesic: transporting along the different paths does not seems to introduce relevant differences. We notice that the right transport Π^R and the Schild's Ladder provide the most consistent and robust results. The left (Π^L) and the symmetric (Π^S) transports appear to be more sensitive to the very high Jacobian matrix variations of the LDDMM trajectory, though they are still consistent with respect to the deformation pattern. The "concentration" of the transported vector field at the high momentum places along the LDDMM trajectory could be interesting for statistical studies but might also disperse more easily the information even in case of very small inter-subject matching errors.

This very simple experiment shows that the SVF tools can also be used in different settings such as with LDDMM, where geodesics can be approximated by a sequence of stationary approximations. Moreover, the similarity of the transport on the different paths suggests that the parallel transport is more influenced by the type of parallel transport than by the inter-subject registration method. It would be quite interesting to verify if this still holds for the LDDMM transport. In all cases, the numerics behind the parallel transport scheme seems to be a key issue.

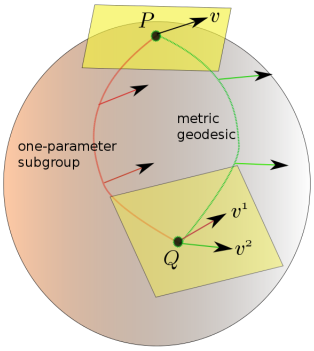

Figure 4.9: The parallel transport of the vector v closely depends on the chosen trajectory, and generally transporting along different curves lead to different parallel vectors.

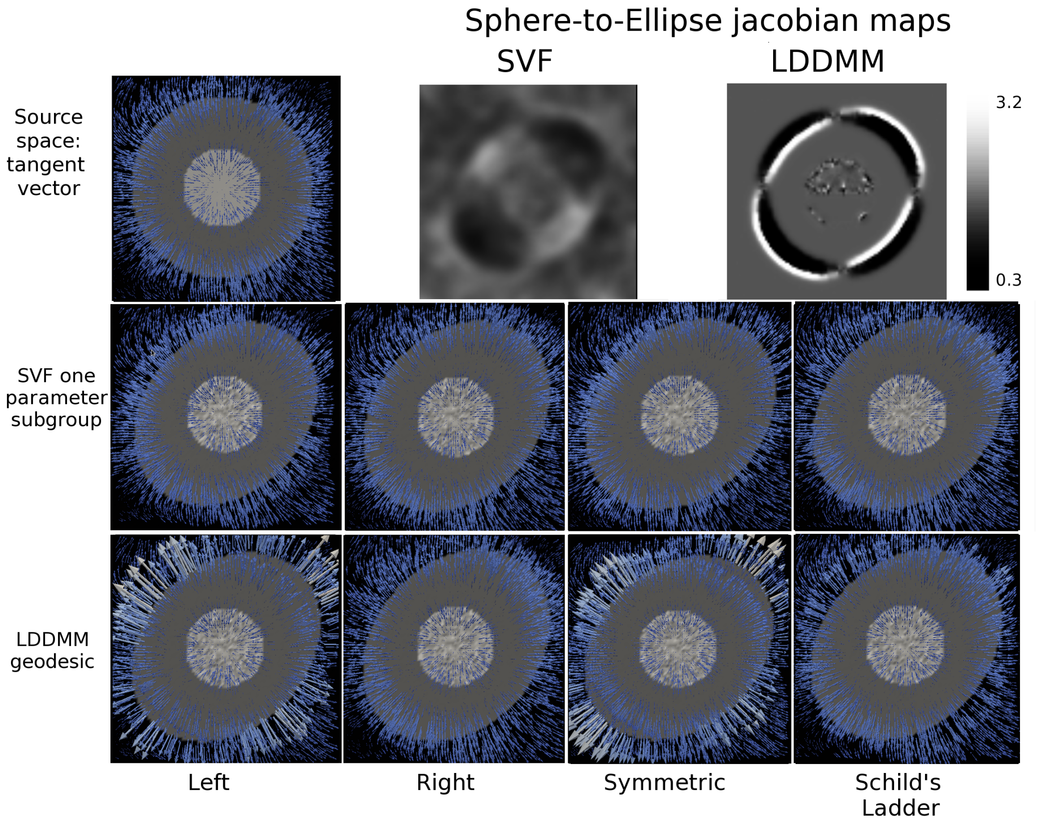

Figure 4.10: Parallel transport of the longitudinal trajectory on the sphere to the ellipse target space along the trajectories defined by the SVF one-parameters subgroup and the LDDMM metric geodesic. The Schild's Ladder and the Right Cartan connection lead to the more consistent results in term of the resulting transported vectors.

4.6 Conclusions and Perspectives

This study investigates the theoretical background which underlies diffeomorphic registration based on stationary velocity fields. We illustrate the use of Lie group concepts to derive effective and efficient solutions for computational anatomy. We showed that the one-parameter subgroups (and their left and right translations) are geodesics of the a family of connections called Cartan connections. This mathematical setting is completely consistent with the Lie group operations (left and right composition, inversion) and leads to a closed form solution for the parallel transport. Moreover, the geodesics of the Cartan connections are "metric-free", and the parallel transport is not related to the preservation of metric properties. This affine geometric mathematical setting differs from invariant Riemannian manifolds used for instance in LDDMM, for which the choice of left or right invariance, as well as the choice of the metric, lead to different geodesics. Among the three canonical (right, left and symmetric) Cartan connections, the transport with the right one was the smoother, due to the simple computational requirements. However, this connection is related to a specific geometry where the group is flat (no curvature), but has torsion. From a theoretical point of view, it is widely accepted in other domains (e.g. general relativity and gravitation) that working with a symmetric connection is preferable than working in a space with torsion. However, we believe that it would worth verifying by experiments on real data that the symmetric Cartan connection indeed leads to a better description of the groupwise anatomy than non-symmetric ones. Such test could be performed on disease classification experiments for instance, where the statistical power of the separation would designate the optimal parallel transport method.

The experimental results highlight also the trade-off between the choice of proper mathematical constructions and the related numerical implementation issues. For instance, the left and symmetric Cartan transports could benefit from more robust numerical schemes for the computation of the differential quantities like the Jacobian matrix, which could lead to more stable and accurate results. On the registration side, our experiments showed that the SVF and LDDMM settings performed very similarly in the longitudinal case. This result suggests that, when dealing with small deformations, stationary and time varying parametrization lead to negligible discrepancies. Moreover, even in case of the inter-subject registration, the different parametrization performed similarly for the resulting intensity matching. It seems therefore that the choice of the admissible transformations is decisively circumscribed by the smoothness constraints and by the numerical implementation, which limit the set of possible anatomical deformations that can be retrieved by a registration algorithm.

We should note that the above conclusions come from a precise choice of the registration parameters (fluid/elastic regularization, incompressibility, ...), and we cannot exclude that a different tuning might lead to a different scenario. However, the choice made here was motivated by the search of an optimal compromise between registration accuracy and smoothness of the deformations and, among the several configurations tested, the proposed was the most suitable one. Moreover, given the lack of a ground truth for the inter-subject registration problem, the reliable comparison of different registration techniques can be assessed only by statistical measures on large datasets, which goes beyond the scope of the presented study.

Part II

Modeling the Longitudinal Atrophy Progression in the Brain: from Normal Aging to AD

Chapter 5

Longitudinal Analysis of Deformation Trajectories: Modeling the Differential Atrophy in Clinical Populations.

Contents

This chapter builds upon the previous methodological contributions to define a hierarchical framework for the group-wise analysis of time series of images. It was presented as a conference paper in [Lorenzi et al., 2011a]. The registration algorithm proposed here is a preliminar implementation of the local correlation criteria in the log-Demons as proposed in Pascal Cachier's PhD thesis [Cachier, 2002].

Mapping the effects of different clinical conditions on the evolution of the brain structural changes is of central interest in the field of neuroimaging. A reliable description of the cross-sectional longitudinal changes requires the consistent integration of intra and inter-subject variability in order to detect the subtle modifications in populations. In computational anatomy, the changes in the brain are often measured

by deformation fields obtained through non rigid registration, and the stationary velocity field (SVF) parametrization provides a computationally efficient registration scheme. The aim of this study is to extend this framework into an efficient and robust multilevel one for accurately modeling the longitudinal changes in populations. This setting is used to investigate the subtle effects of the positivity of the CSF $A\beta_{1-42}$ *levels on brain atrophy in healthy aging. Thanks to the higher sensitivity of our framework, we obtain statistically significant results that highlight the relationship between brain damage and positivity to the marker of Alzheimer's disease and suggest the presence of a presymptomatic pattern of the disease progression.*

5.1 Introduction

The ability to map the different areas involved in the neurodegenerative processes is of primary importance for the formulation of new clinical hypotheses on the pathological mechanisms. Moreover, the availability of a longitudinal model of the disease progression would provide a reliable standard for diagnostic purposes. The problem is particularly relevant in the field of Alzheimer's disease (AD) which is characterized by the progressive abnormal configuration of the biochemical, functional and structural markers in the brain which may occur up to decades before the clinical assessment [Frisoni et al., 2010]. Among the earliest potential markers, the pathological configuration of the CSF $\mathrm{A}\beta_{1-42}$ was shown to be associated with a general increased predisposition to clinical conversion to AD. It is therefore of great interest to model the subtle differential evolution from normal aging of the brain changes in subjects who are not affected by the disease but present lower $\mathrm{A}\beta_{1-42}$ levels. For this purpose, robust, sensitive, accurate and reproducible modeling techniques are required.

The non-rigid registration is a candidate instrument to quantify the structural differences between brain images and the new generation registration algorithms provide diffeomorphic registration [Vercauteren et al., 2008, Miller et al., 2002]. Among them, the log-Demons algorithm provides an accurate and computationally efficient approach, by using stationary velocity fields (SVF) as parametrization of the deformations.

The analysis of longitudinal data requires to go one step further and to integrate the temporal dimension into the registration procedure. The main complexity of the problem lies in the different levels of variation introduced by the different nature of the small intra (*longitudinal*) and large inter-subject (*cross-sectional*) changes: the measurements from time series of a specific subject must be normalized into a comprehensive spatio-temporal atlas. Although different approaches have been proposed in the past for the group-wise analysis of longitudinal dataset [Avants et al., 2007, Younes et al., 2008], a consensus on the optimal strategy to handle the different levels of information is still missing, for instance for the choice of the different metrics for intra and inter subject normalization.

We believe that the reliable quantification of the group-wise longitudinal changes should independently address the different sources of variability with proper methods, and consistently integrate the different levels into a general framework. In previous works the SVF setting was shown to provide:

1. An *efficient* pairwise-registration scheme with log-Demons [Vercauteren et al., 2008];
2. A *straightforward* way to model the subject-specific deformation trend from time series with a spatio/temporal regularization procedure [Lorenzi et al., 2010a];
3. A *stable* way to transport the subject-specific trends in the atlas geometry using the parallel transport given by the Schild's Ladder procedure [Lorenzi et al., 2011b].

The goal of this paper is 1) to combine these previous contributions in a robust, efficient and precise tool for modeling group-wise deformation, and 2) to use the framework to analyze and model the subtle effects of the CSF $A\beta_{1-42}$ levels on longitudinal brain atrophy in healthy elders.

5.2 Modeling Changes in Time Series of Images with the SVF Framework

We assume that the subject specific evolutions are random realizations of an underlying ideal population trend. The hierarchical generative model is therefore composed of the following levels:

1. We model the *population trend* as the deformation $\mu^G(t)$ of a template T_0 over time. The (spatially normalized) deformation trend of subject K in the template space is assumed to be a random realization of a Gaussian process $\mu^K(t) = \mu^G(t) + \varepsilon_K$. It is the goal of step 4 to estimate the population trend $\mu^G(t)$ from the spatially normalized subject's longitudinal trends.
2. To account for the spatial variability of the anatomy across the population, the subjects specific coordinate system is defined by a spatial changes of coordinates $\phi^{K(-1)}$ from the template to the subject. The *subject specific* deformation trend $\mathbf{v}^K(t)$ is then modeled as the parallel transport of the spatially normalized subject's longitudinal trend $\mu^K(t)$ along the template-to-subject spatial change of coordinates $\phi^{K(-1)}$. Step 3 is taking care of solving the reverse problem in a discrete time setting.
3. Subject specific longitudinal trends are then sampled in time (modeling the discrete acquisition times) and a deformation noise accounting for the influence of random confounding factors (hydratation, vasodilation, etc) is added independently at each time point to obtain the *subject-specific* deformation $\mathbf{v}_i^K = \mathbf{v}^K(t_i) + \varepsilon_i$ at time point t_i. Step 2 aims at solving the inverse problem.

4. Last but not least, the subject time series of images is generated by deforming the subject baseline image I_0^K with an acquisition noise on intensities: $I_i^K = \exp(\mathbf{v}_i^K) * I_0^K + \varepsilon_i^I$. Step 1 is solving the inverse problem using non-linear registration.

Let us now address the inverse problem: estimating the population trend from the time series of patient images. We detail below step by step the solution we propose to solve each level of the generative model (in the reverse order).

5.2.1 Step 1: Robust Pairwise Registration with the og-Demons Algorithm

For each subject K, the longitudinal changes along the time series of images I_i^K, $i = 0, \ldots, n$ acquired at time $t_0 = 0, \ldots, t_n$, are evaluated by non rigid registration with respect to the reference time point, here the baseline I_0^K.
The log-Demons algorithm aims at matching the images I_0 and I_i by looking for the deformation φ which maximises their similarity. The deformation φ belongs to the one-parameter subgroup generated by an optimal vector field $\mathbf{v}$, and the parametrisation is defined by the group exponential map $\varphi = \exp(\mathbf{v})$ [Arsigny et al., 2006].
In the standard log-Demons algorithm the "unregularized" correspondence field $\mathbf{v_x}$ is given by the minimization of the sum of squared differences (SSD) between the intensities of the two images, which is not robust to the intensity biases. In order not to mistake spurious intensity variations for morphological differences, we first propose to resort to the local correlation coefficient, introduced in [Cachier et al., 2003]:

$$E(I_0, I_i, \mathbf{v_x}, \mathbf{v}) = \min_{(a,b)} \int G_{\sigma_S} * \|(a(x) \cdot I_0(x) + b(x)) - I_i(x) \circ \exp(\mathbf{v_x})(x)\|^2 + \\ + \frac{1}{\sigma_x^2} \| \log(\exp(-\mathbf{v})(x) \circ \exp(\mathbf{v_x})(x)) \|_{L_2}^2 \qquad (5.1)$$

The spatially varying coefficients $a(x), b(x)$ account for the additive and multiplicative biases for the intensities. Moreover the bias estimation is local, thanks to the Gaussian weights on the error norm. In practice, the standard correspondence energy of the log-Demons is replaced by $E(I_0, I_i, \mathbf{v_x}, \mathbf{v})$, while preserving the remaining structure of the algorithm. As proposed in [Cachier et al., 2003], the minimization of (5.1) is operated through a two step procedure: a first step evaluates the optimal scaling factors a and b voxel-wise, that are then reintroduced for the optimization of $\mathbf{v}_x$ through a Gauss-Newton scheme. Experiments on both synthetic and real data showed that the local similarity criteria allows to robustly compute deformations in presence of bias and generally provides smoother estimation of the anatomical differences (data not shown due to space constraints). The important robustness improvements came at the price of a reasonable increase of the computational time (around 25 minutes on a Pentium Intel Core Duo 2.4Ghz for registering images with resolution 182x182x218, voxel size 1x1x1) .

5.2.2 Step 2: Modeling the Subject Specific Longitudinal Trends

In order to obtain smoother estimations of the subject specific trajectory and to reduce the intra-subject variability given by possible confounding factors, the Step 2 consists in introducing a temporal correlation into the estimated serial deformations through a 4D registration scheme [Lorenzi et al., 2010a]. The procedure is particularly indicated here, since we are going to investigate the subtle morphological changes occurring in the brain of cognitively healthy subjects, and we do not expect to model sharp variations or sudden modification of the longitudinal series. The subject specific trend $\bar{\mathbf{v}}^K(t) = L(\mathbf{v}_i^K, t_i, t)$ is estimated with a linear model in time from the time series of static velocity fields $\mathbf{v}_i^K$ evaluated in the Step 1 for the pairs I_0^K, I_i^K. We note that given the small number of time points (around 4 for the ADNI dataset), and the basic assumption of mild brain changes, a linear SVF model (which is a non-linear deformation model) represents a reasonable choice for the present analysis. The $4D$ registration integrates the $\bar{\mathbf{v}}^K(t)$ in a new registration step in order to provide a temporal prior for finally estimate the spatio-temporal regularized sequence of the static velocity fields $\mathbf{v}_i'^K$.

The solution at each time point t_i is represented by the weighted average between the temporal prior $\bar{\mathbf{v}}^K(t_i)$ and the spatial correspondence $\mathbf{v}_\mathbf{x}$ provided by the similarity measure. Previous experiments showed that the 2:1 trade-off between spatial and temporal weights defines sufficiently smooth trajectories while not biasing the changes towards a completely linear model.

5.2.3 Step 3: Transporting the Subjects Trajectories in the Atlas Geometry.

In order to compare the longitudinal trajectories between the different subjects and to perform statistical analysis, we need to transport the series of velocity fields $\mathbf{v}_i'^K$ in a common reference. For this purpose, we base the transport on the Schild's Ladder method [Lorenzi et al., 2011b]. The method relies on the technique introduced in the field of theoretical physics for computing the parallel transport of tangent vectors on a general manifold without requiring the knowledge of the global geometrical properties of the space. It is based on the construction of a "geodesic parallelogram" for transporting vectors along *any* curve (and not just the geodesics of a specific choice of metric)[1]. More precisely, the parallel transport of the trajectory $\mathbf{v}_i'^K$ from Step 2 along the curve $\phi^K = \exp(t\mathrm{u}^K)$ connecting I_0^K and T_0 is the field $\mathbf{v}_i^{*K} = \Pi^{\phi^K}(\mathbf{v}_i'^K) \simeq \mathbf{v}_i'^K + [\mathrm{u}^K, \mathbf{v}_i'^K] + \frac{1}{2}[\mathrm{u}^K, [\mathrm{u}^K, \mathbf{v}_i'^K]] + o(t^3)$.

5.2.4 Step 4: Longitudinal Group-wise Modeling

The transported time series of SVF $v_i^{*K} = \Pi^{\phi^K}(\mathbf{v}_i'^K)$ belonging to different subjects can now be easily compared in the reference space T_0. In order to develop a group-wise model for the trajectories, we propose here a random effect analysis based on the longitudinal transported trends. Let $\mu^K(t) = L(\mathbf{v}_i^{*K}, t_i, t)$ be the spatially

---

[1] In the case of SVF, the geodesic parallelogram is based on the one-parameter subgroups whicht are the geodesics of the Cartan connections [Postnikov, 2001].

normalized subject trend modeled in the reference space with a linear model in time[2]. The different subject trends $\mu^K(t)$ characterize the trajectories across the populations and by comparing them it is possible to provide a description of the group-wise evolutions. In the following, the different evolutions across the groups (say $+$ and -) will be statistically assessed on the group-wise mean deformation trends $\mu^+(t)$ and $\mu^-(t)$. However, the visual differences between the trends will be illustrated by applying the longitudinal evolutions to the template image: $T^+(t) = \exp(\mu^+(t)) * T_0$ and $T^-(t) = \exp(\mu^-(t)) * T_0$.

5.3 Effects of Aβ_{1-42} Positivity on Healthy Aging

The T1 weighted longitudinal scans (baseline, 6, 12, 24 and 36 months) were selected for 98 healthy subjects from the ADNI dataset [Mueller et al., 2005]. Two subgroups were then defined based on the positivity to the Aβ_{1-42} marker defined by values below the threshold of 192 pg/ml and resulted in 41 subjects Aβ_{1-42} positives and 57 negatives (Aβ^+_{1-42} and Aβ^-_{1-42}). The two groups were similar at baseline for gender (% of women: 45 % for Aβ^+_{1-42} , 51 % for Aβ^-_{1-42}), age (75±5, 75±5) and education (15.8±3.17, 15.5±2.7). For each subject, the time series of images were aligned through an unbiased procedure consisting on the iterative rigid registration to the median image computed voxel-wise. The final median image was linearly registered to the MNI132 template and the affine transformation was then applied to the series.

The 4D registration algorithm was applied to the longitudinal series of each subject, with $\sigma_S = 10mm$ for the local similarity criteria, $\sigma_{fluid} = 0.5mm$ and $\sigma_{elastic} = 1mm$ for the regularization. The Schild's Ladder was used to transport the longitudinal trajectories from the subject to an unbiased population-based Template T, computed as in [Guimond et al., 2000] (Inter-subject registrations were also computed with the log-demons algorithm).

The mean trends μ^- of the Aβ^-_{1-42} and μ^+ of the Aβ^+_{1-42} groups were computed from the estimated subject-specific trends. Their difference was assessed on a voxel-by-voxel basis by a multivariate analysis based on the Hotelling's two-sample T^2 statistic (Figure 5.2C). The statistical significance was assessed after correction for multiple comparisons by means of permutation test (1000 permutations). Moreover, the trends allowed to compute the mean evolutions for the Template space and to qualitatively assess the differential progression between the two groups (Figure 5.2A/B). Finally, a region of interest (ROI) based analysis was performed on the average log-Jacobian values of the estimated trajectories in selected areas of the Template space, segmented through an automated procedure(Ventricles, Hippocampus, Amygdalae, Caudate and Thalamus) [Patenaude et al., 2011].

---

[2] We notice that the model fitted in the log-domain does not imply a linear trend for the parametrized deformations.

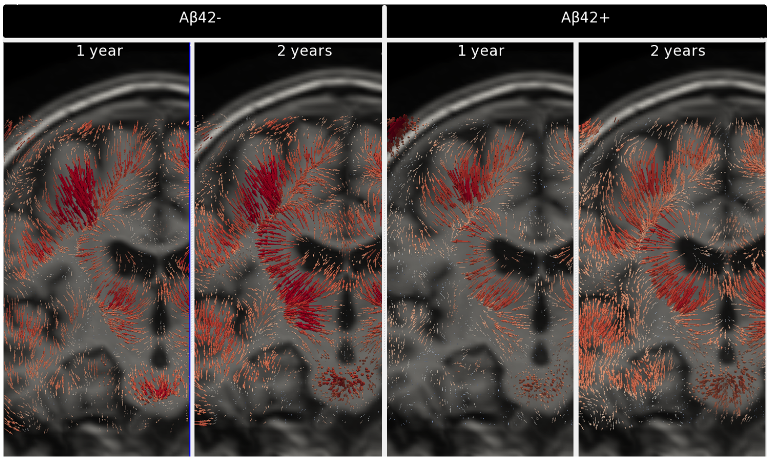

Figure 5.1: Average SVF from baseline for the $A\beta^{-}_{1-42}$ (left) and $A\beta^{+}_{1-42}$ (right) groups. For both groups the average forces increase longitudinally, but we can notice an acceleration for the changes across the hippocampus and the temporal regions for the $A\beta^{+}_{1-42}$ group.

5.4 Results and Perspectives

Figure 5.1 shows the average SVF estimated for the two groups from baseline. Although the two groups show a similar pattern for the ventricular expansion, the $A\beta^{+}_{1-42}$ shows an increased flow of vectors across the temporal regions and hippocampus. Figure 5.2A highlights the modeled longitudinal changes from baseline for the $A\beta^{-}_{1-42}$ group. The aging effect can be appreciated in the ventricular expansion and in the spread cortical changes. The *additional* changes due to the positivity to the marker $A\beta_{1-42}$ are displayed in Figure 5.2B. The positivity to $A\beta_{1-42}$ is characterized by an increased longitudinal changes located in the temporal areas and by the ventricles expansion. We notice that the average progression built from the estimated SVF allowed to generate not only a summary of the observation, but also to extrapolate the expected evolution 2 years after the end of the study. The multivariate statistical assessment of the differences between the evolution of the two groups is shown in Figure 5.2C. It involves hippocampi, ventricles and the temporal regions. Interestingly, the voxel-by-voxel statistical analysis on the associated log-Jacobian scalar maps showed similar patterns but failed to reach the statistical significance after the correction for multiple comparisons. This suggests a higher sensitivity of the analysis when performed on the multivariate SVF $\mathbf{v}$ rather than on scalar higher order quantities such $\mathbf{det}(\nabla\mathbf{v})$. Supplementary material can be found in http://www.inria.fr/sophia/members/Marco.Lorenzi/SVF_Framework. The regional differences were confirmed by the ROI based analysis, where significant differences for the volume change/year were found in the ventricles (3.84% for $A\beta^{-}_{1-42}$, 6.72% for $A\beta^{+}_{1-42}$, p=0.009) and in the hippocampus (0.14%, 0.24%, p= 0.014) while no significant differences were detected in the other regions.

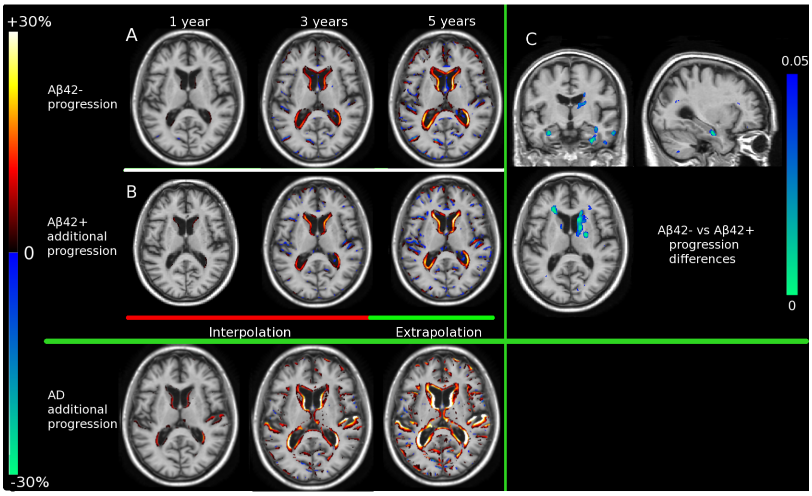

Figure 5.2: Modeled longitudinal annual % intensity changes for the Aβ^{-}_{1-42} group with respect to the baseline, and for B) the Aβ^{+}_{1-42} group with respect to the Aβ^{-}_{1-42} longitudinal progression. In C) are shown the areas of statistically significant difference between the trends of the Aβ^{-}_{1-42} and the Aβ^{+}_{1-42} groups (colors: significant p-values, $p<0.05$ corrected). Supplementary bottom row: modeled additional loss with respect to the Aβ^{-}_{1-42} progression for an AD group from the ADNI dataset. We can notice the analogies between the Aβ^{+}_{1-42} trend and the real pathological evolution.

5.5 Conclusions and Perspectives

The present work introduces a consistent and effective framework for the analysis of longitudinal data of 3D MRI images. As result, it allowed to model the subtle changes which differentiate the longitudinal evolution of healthy people with abnormal Aβ_{1-42} level from those in the normal range, and which is represented by increased ventricular expansion and spread matter loss in the temporal regions [Fjell et al., 2010, Schott et al., 2010, Tosun et al., 2010]). The resulting trajectories incorporate a wide range of informations (velocities, deformations, volume changes, . . .) which could provide new insights for the understanding of the biological phenomenas, like modeling and describing the pathological evolutions (such as in Figure 5.2). For instance, the extrapolation result is an appealing feature in epidemiology as it enables previsions that could motivate clinical hypothesis, as in the presented work. Moreover, the soundness of the extrapolated data indicate the stability and the robustness of the proposed method.

Part III

Discovery and Quantification of the Longitudinal Atrohpy

Chapter 6

Regional flux analysis of longitudinal atrophy in Alzheimer's disease.

Contents

This chapter was presented as conference paper in [Lorenzi et al., 2012d]. Here we introduce a novel framework for the consistent extraction of longitudinal atrophy patterns and the statistically powered quantification of anatomical changes based on the Helmholtz decomposition of vector fields.

The longitudinal analysis of the brain morphology in Alzheimer's disease(AD) is fundamental for understanding *and* quantifying *the dynamics of the pathology. This study provides a new measure of the brain longitudinal changes based on the Helmholtz decomposition of deformation fields. We used the scalar pressure map associated to the irrotational component in order to identify a consistent group-wise set of areas of maximal volume change. The atrophy was then quantified in these areas for each subject by the probabilistic integration of the flux of the longitudinal deformations across the boundaries. The presented framework unifies voxel-based and regional approaches, and robustly describes the longitudinal atrophy at group level as a*

spatial process governed by consistently defined regions. Our experiments showed that the resulting regional flux analysis is able to detect *the differential atrophy patterns across populations, and leads to precise and statistically powered* quantifications *of the longitudinal changes in AD, even in mild/premorbid cases.*

6.1 Introduction

The longitudinal analysis of the brain morphology in Alzheimer's disease(AD) is fundamental for *understanding* and *quantifying* the dynamics of the pathology. The analysis of time series of MR images has been based on two different paradigms: hypothesis free and regional analysis. In the former case, the longitudinal atrophy is modeled at fine scales on the whole brain such as in the voxel/tensor based morphometry and cortical thickness analysis [Fox et al., 2001, Thompson et al., 2003]. These methods are useful for exploratory purposes, but usually lack robustness for a reliable quantification of the changes at the subject level, due to the high variability of the measurements and the multiple comparison problems. On the other hand, the regional analysis is focused on the detection of significant changes on regions which are usually identified thanks to segmentation. For instance, the boundary shift integral identifies the longitudinal atrophy as the shift of the segmented boundaries [FreeBorough and Fox, 1997], and led to powered measure for the longitudinal hippocampal changes in Alzheimer [Leung et al., 2010]. However, this kind of approaches relies on strong a priori hypotheses on the localization of the dynamics of interest, and might fail to detect more complex patterns of changes which are likely to underly the evolution of the pathology. Providing a longitudinal measure which could at the same time identify, *consistently localize*, and *reliably quantify* the longitudinal changes is crucial for understanding the dynamics of the pathological evolution and to provide stable measures for the clinical setting.

Non rigid registration encodes the morphological changes between pairs of longitudinal MRIs as deformation fields. It has been employed for both whole brain exploratory analysis and regional quantification, for instance through the Jacobian determinant analysis. However, the regional quantification still relies on prior segmentation, and is still sensitive to the biases, for instance for the numerical derivative required for computing the Jacobian. The deformation fields implicitly encode the spatial location of relevant atrophy processes, and novel analysis techniques are required to consistently extract and analyze these features. It has been proposed in [Hansen et al., 2009] to parametrize the deformations by irrotational and divergence-free components, according to the Helmholtz decomposition of vector fields. If we assume that the atrophy can be completely described by a change of volume, then it is completely encoded by the irrotational part, while the divergence-free one only accounts for the tissue reorganization. Thus, the maximal/minimal locations of the irrotational potential define the centers of expanding and contracting regions, and may represent a promising measure for morphometric studies. A different measure of volume change associated to the deformation field is the flux across surfaces [Chung et al., 2001], which is the mathematical formulation of the boundary shift. However flux-based analysis has been seldom used in morphometric studies, due to the complexity of reliably integrate vector normals on probabilistic segmentations of the surface boundaries.

In this study we propose the regional flux analysis, a new approach for the study of morphological changes based on the Helmholtz decomposition of vector fields. In Section 1 we introduce the Helmholtz theorem, and the relationship between pressure and flux of deformations. These measure are used in Section 2 to consistently define through a hierarchical model the subspace of regions involved in the atrophy processes . These regions are then used at the subject level for the probabilistic flux integration. Finally, the framework is applied in Section 3 on a large sample of longitudinal observation from the ADNI dataset [Mueller et al., 2005], to *describe* and *quantify* the pathological changes at different clinical stages, from premorbid, to early and late Alzheimer stages.

6.2 Helmholtz Decomposition for Stationary Velocity Fields

The present work is based on the registration based on stationary velocity fields (SVF), which has been already applied for the longitudinal analysis of deformations [Lorenzi et al., 2011a], and for which an implementation of the LCCDemons algorithm was already proposed (Chapter 2).

6.2.1 Pressure Potential and Flux Through a Region

The Helmholtz theorem states that, given a vector field v defined on $\mathbb{R}^3$ which vanishes when approaching to infinity, it can be uniquely factored as the sum of an irrotational and a divergence free component, $v = \nabla p + \nabla \times A$. The irrotational component ∇p is the gradient of a *scalar* pressure (potential) field p. Since $\nabla \times \nabla p = 0$, the component encodes the information concerning the volume change. On the other hand the divergence-free component is by definition such that $\nabla \cdot \nabla \times A = 0$ and therefore it describes the rotational part of the velocity. Finally, the flux of a stationary velocity field across a given surface ∂V is given by the Divergence (or Ostrogradsky's) theorem, and can be rewritten as $\oint_{\partial V} v \cdot \boldsymbol{n}\, dS = \int_V \nabla \cdot v\, dV$. Recently the Helmholtz decomposition has been introduced in the Demons registration in order to estimate incompressible deformations [Mansi et al., 2010]. Here we propose to use it on the contrary for the analysis of the compressible part, which encodes the observed matter loss as a smooth compression/expansion process. In such a model, the associated divergence quantifies the apparent anatomical changes as the flux of the estimated vector field across surfaces.

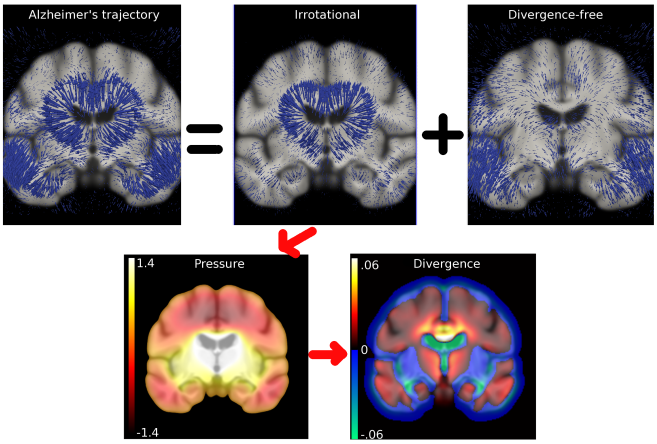

Figure 6.1: Helmholtz decomposition of a longitudinal trajectory in Alzheimer's disease, and pressure potential and divergence maps associated to the irrotational component. The divergence describes the critical areas of local expansion and contraction.

6.2.2 Topology of Pressure Fields

Theoretically, one could partition the whole space into *critical areas* of positive and negative divergence, each of them containing a critical point of local maximal/minimal pressure (Figure 6.1). From the divergence theorem, the flux across the boundaries of these areas is either flowing inward or outward. The saddle points for the pressure are on the boundaries of those regions, and identify a change in the flow.

The analysis of the critical points of a pressure map can be addressed by the *Morse-Smale* theory as a topological problem, leading to a complex of regions, boundaries, edges and vertices. Although intriguing, the application of such concepts to the medical imaging is still difficult, due to the missing statistical version of the Morse theory. In order to obtain a tractable approach to the problem, we propose to first focus on the definition of a consistent *subset* of critical regions across subjects, to robustly describe the atrophy processes at group level as a spatial process governed by key areas. This is a first step towards a topology definition and provides a sparse description of the deformation.

6.3 Flux-based Analysis of Longitudinal Trajectories

The goal of this section is to estimate the group-wise set of critical regions, from the locations of maximal/minimal pressure. These regions are then used to evaluate the flux of the longitudinal deformations at the subject level.

6.3.1 Group-wise Pressure Potential from Longitudinal SVFs

Consider the longitudinal observations from a group of subjects composed of baseline I_0^i and follow-up I_1^i brain scans. For each subject i, the log-Demons non rigid registration of the pair I_0^i, I_1^i estimates the longitudinal trajectory of changes as a diffeomorphism parametrized by stationary velocity field $\exp(v_i)$, such that $I_0^i \circ \exp(v_i) \simeq I_1^i$. The SVF v_i can then be decomposed according to the Helmholtz theorem in order to identify the corresponding pressure map p_i.

One interest in this decomposition is that the transport of each atrophy trajectory $\varphi_i = \exp(v_i) = \exp(\nabla p_i)$ through a subject-to-template deformation ψ_i can be obtained by simple scalar interpolation of the pressure field $\varphi_i^T = \exp(v_i^T) = \exp(\nabla(p_i \circ \psi_i))$, rather than parallel transporting vector quantities, $\varphi_i^T = \exp(\Pi^{\psi_i}(v_i))$, which generally leads to computationally intensive and potentially more unstable operations.

The pressure maps in the template space $p_i \circ \psi_i$ are integral quantities, and might differ by an arbitrary constant. However, an average pressure map can still be consistently defined either as $\overline{p} = \overline{p_i \circ \psi}$, or as the pressure map $\overline{p}$ associated to $\overline{v} = \overline{v_i^T} = \overline{\nabla(p_i \circ \psi_i)}$.[1]

6.3.2 Probabilistic Estimation of Group-wise Critical Regions

Let $\{x_k\}$ be the set of critical points, maxima and minima, of $\overline{p}$. These points define the critical areas T_k of local expansion and contraction, i.e. of positive and negative divergence. Then, the probability of a point x to belong to a critical region depends on the proximity to the region T_k, and on the observed divergence. We can express this through the Bayes rule:

$$P(x \in T_k | \nabla \cdot v(x) = d) \quad = \quad \frac{P(\nabla \cdot v(x) = d | x \in T_k) P(x \in T_k)}{P(\nabla \cdot v(x) = d)} \tag{6.1}$$

Since the denominator is a normalizing factor, in the following only the numerator is considered. The flux of the subject specific deformations $\exp(v_i)$ through the regions T_k can be easily estimated with (6.1) through a hierarchical model. At the first level, based on spatial priors for the location of the critical points, we can estimate a group-wise confidence map for the critical regions:

- Given a set of critical points $\{x_k\}$, define the spatial priors $P(x \in T_k) = \exp((x - x_k)^2/(2\sigma^2))$
- Define a group-wise prior $\overline{F_i^{\pm}}(x)$ for the critical areas as the group-wise average of the binary masks of positive/negative divergence $F_i^+ = \left\{x \in \Omega | \nabla \cdot v_i^T(x) > 0\right\}$, and $F_i^- = \left\{x \in \Omega | \nabla \cdot v_i^T(x) < 0\right\}$.
- From formula (6.1), define the confidence maps for the critical areas $P_k^{\pm}(x) = P(\nabla \cdot v_i^T(x) = d | x \in T_k) P(x \in T_k) = \overline{F^{\pm}}(x) \exp((x - x_k)^2/(2\sigma^2)$.

---

[1] In fact, if $p_i' = p_i \circ \psi_i + c_i$, with c_i constant, then $\overline{p} = \overline{p_i \circ \psi_i} + \overline{c}$ leads to $\overline{v} = \nabla \overline{p} = \overline{\nabla(p_i \circ \psi_i)}$

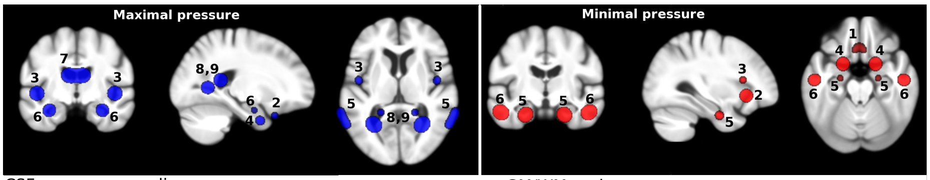

CSF areas surrounding:

E1 - inferior orbital cortex
E2/3 - insula/superior temporal pole
E4 - Mid-temporal pole
E5 - Sup/Mid temporal pole

Ventricles areas:
E6 - Temporal horn hippocampus
E7/8/9 - Ventricles

GM/WM regions:

C1 - Gyrus rectus
C2 - Insula
C3 - Inferior frontal gyrus
C4 - Amygdalae/parahipp gyrus
C5 - Hippocampus
C6 - Temporal poles

Figure 6.2: Critical points associated to the Alzheimer's average pressure map.

Finally, the group-wise confidence maps are reintroduced in (6.1) for the second level analysis :

- Transport the confidence maps $P_k^{\pm}$ in the subject space to obtain $P_{k,i}^{\pm} = P_k^{\pm} \circ \psi^{-1}$
- Apply (6.1) by considering $P(x \in T_k) = P_{k,i}^{\pm}$, and $F_i^{\pm} \circ \psi_i^{-1}$ as likelihood term.

6.3.3 Probabilistic Integration of the Regional Flux

The confidence maps in the subject space can then be used as weights for the integration of the divergence across the space Ω thanks to the Divergence theorem, to provide a measure of the subject specific flux across the critical regions T_k. The weighted integration of the divergence implicitly defines the critical regions in a maximum a posteriori approach through the posterior (6.1), therefore automatically accounting for the registration biases in the anatomical localization (e.g. due to the regularization).

6.4 Apparent Gain and Loss of Matter in Alzheimer's Disease Through Regional Flux Quantification

Baseline and one year follow-up brain scans of 200 healthy controls, 150 MCI, and 142 AD patients from the ADNI dataset were linearly aligned and non-rigidly registered with the log-Demons. The pressure maps p_i corresponding to the intra-subject longitudinal trajectories $\exp(v_i)$ were transported into a previously defined anatomical reference along the subject-to-template deformations ψ_i.

The set of local maxima and minima for the pressure in AD has been defined from the mean pressure map associated to the longitudinal deformations of 20 randomly selected AD patients. Of these sparse sets of points, 9 local minima and 6 local maxima have been manually labeled to define the set $\{x_k\}$ of critical points.

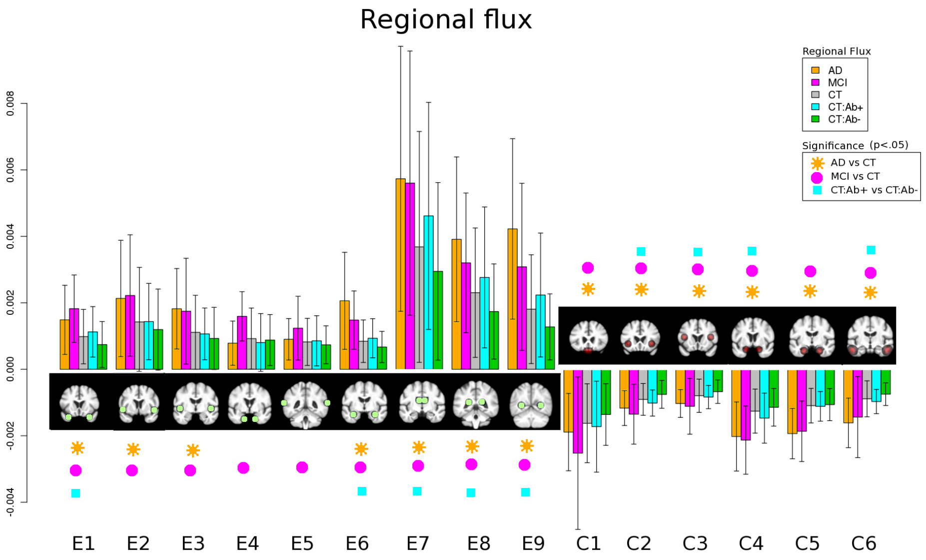

Figure 6.3: Average regional flux for AD, MCI, healthy controls, and healthy $A\beta^+$ and $A\beta^-$ subgroups. E1 to E9: expanding regions. C1 to C6: contracting regions.

The spatial priors T_k were defined through inflation (4 voxels neighborhood) and right/left symmetry (Figure 6.2).

The hierarchical model of Section 6.3 was used for the regional probabilistic integration of the flux for the remaining patients and the healthy controls. Moreover, the healthy population was stratified depending on the positivity to the CSF $A\beta_{42}$ marker (<192 pg/ml), and the flux analysis was performed to detect the effect of the positivity on the atrophy progression.

Figure 6.3 summarizes the group-wise regional flux. As we can see, the flux is higher for the ADs and MCIs with respect to the controls. Interestingly, the MCIs have larger flux than the ADs in some regions, which might indicate greater structural longitudinal changes at the early stages of the disease, or underline different aspects of the heterogeneous MCI condition. The subgroup of healthy subject positive to the $A\beta42$ marker consistently show increased flux when compared to the negative, which is significant for several regions, and might suggest a possible effect of the $A\beta42$ marker on the future development of AD.

A power analysis based on the regional flux was performed to define the sample size required by an hypothetical 1-year clinical trial to detect a 25% difference of the progression of the measure with 80% power when considering the group alone, or by comparing with normal aging [Leung et al., 2010]. The regional measurements provided different sample size estimations (Table 6.1), to summarize the lowest sample size for the AD group was provided by the flux across C5 (hippocampus): 38 (95% CI [33,44]) by considering the AD alone, and 203 [145,307] when controlling by normal aging. For the MCI group, the lowest sample size was given by the region E4 (mid-temporal pole): 54 [47,63] for the group alone and 307 [192,567] when

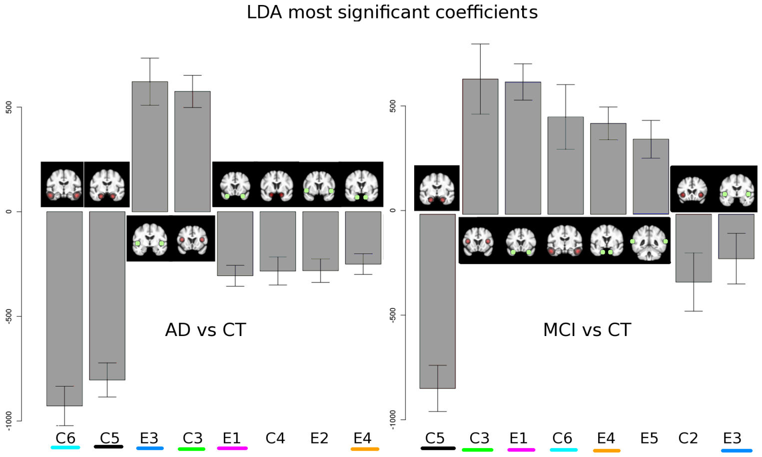

Figure 6.4: LDA coefficients associated to the most discriminant critical regions for the longitudinal atrophy of the AD and MCI groups wrt normal aging. Among these regions, 6 of the 8 are common to both AD and MCI, and are indicated by the common colors.

controlled for normal aging.

Finally a linear discriminant analysis was performed to define the combination of such regions which maximises the flux differences for respectively AD and MCI vs healthy subjects. The analysis was carried out through a 2-folds cross-validation, with 1000 iterations (Figure 6.4). An additional power analysis was performed during the cross validation, to test the effectiveness of the LDA combination of the regional flux as a clinical measure. The average sample size (and average 95% CI) required for the LDA score when controlling for normal aging was 164 [106,290] for the AD group, and 277 [166,555] for the MCI.

6.5 Conclusions and Perspectives

We proposed to decompose the longitudinal trajectories according to the Helmholtz theorem, in order to analyze the atrophy processes through the pressure potential map and the associated flux. This new approach studies the temporal dynamics as a topological problem, and opens the path to new analysis methods based on graph and complex theory. The proposed work provided precise and statistically powered *quantifications* of the group-wise regional atrophy processes. Moreover the presented method *describes* and compares the patterns of dynamic changes between clinical populations, and might thus lead to potentially new anatomical findings, such as differential atrophy trajectories at different disease stages.

Table 6.1: Sample size analysis. Estimated sample size (mean(95%CI)) to detect a 25% difference of the progression of the regional flux with 80% power when considering the group alone (columns 1 and 3), or by controlling for normal aging (columns 2 and 4). Last row: average sample size (average 95%CI) from the LDA analysis, when considering the score given by the combination of the regional flux. The standard formula is sample size= $(u+v)^2(2\sigma)^2/(\Delta\mu)^2$, with $u = 0.841$ (80% power), $v = 1.95$ (5% significance level), $\Delta\mu$ is the annualized percentage rate of atrophy, and σ is the standard deviation of the patients group.

	AD alone	AD (+CT)	MCI alone	MCI (+CT)
Expansions				
E1	122 (96,160)	1067 (515,3395)	78(66,93)	366(239,628)
E2	169 (128,232)	1532 (633,7765)	170(133,225)	1323(614,4682)
E3	111 (88,143)	730 (382,1906)	208(159,285)	1574(729,5597))
E4	179 (135,250)	5920 (1119,8811)	54(47,63)	307(193,567)
E5	119 (94,156)	15502(1833,18816)	151(120,197)	1358(652,4376)
E6	125 (99,166)	361 (239,610)	88(73,107)	475(299,870)
E7	121 (96,159)	948 (466,2886)	208(159,285)	475(299,871)
E9	104 (83,133)	317 (211,528)	166(130,220)	972(524,2391)
Contractions				
C1	95 (77,121)	4802 (1182,9850)	207(158,283)	1629(778,5317)
C2	50 (43,60)	1006 (481,3280)	112(91,140)	1033(561,2500))
C3	41 (36,48)	808 (386,2635)	143(114,184)	1758(805,6427)
C4	66 (55,80)	462 (284,880)	58(50,68)	347(234,564)
C5	38 (33,44)	203 (145,307)	60(51,70)	348(238,558)
C6	54 (46,64)	266 (180,431)	180(140,241))	1232(648,239)
LDA		164 (106,290)		277 (166,555)

Chapter 7

Flux analysis for the reliable measurement of the longitudinal atrophy in Alzheimer's disease

---

Contents

This chapter details the methodological framework presented to the MICCAI Challenge "Atrophy Measurement Biomarkers Using Structural MRI for Alzheimer's Disease" [Lorenzi et al., 2012a]. It extends the flux analysis of Chapter 6 to the longitudinal analysis of the hippocampal atrophy and of the ventricular enlargment.

7.1 Introduction

Alzheimer's disease (AD) is a neurodegenerative pathology of the brain, characterized by a co-occurrence of different phenomena, starting from the deposition of amyloid plaques and neurofibrillary tangles, to the development of functional loss, to finally cause the cell death [Jack et al., 2010b]. Among these pathological changes, the cerebral atrophy measured through magnetic resonance (MR) is usually identified as the "footprint" of the disease which may become dramatic in the latest stages, but which it has been shown to start before the clinical conversion to AD, already at early and premorbid stages [Ridha et al., 2006]. As a consequence, the monitoring of the brain structure has been included in the list of recommended diagnostic criteria [Dubois et al., 2007], and the volume changes of key areas like the hippocampus are now employed as surrogated biomarker in clinical trials. The MR imaging is thus a fundamental instrument for the clinical practice, which is also cheaper and more feasible then other imaging modalities. Therefore, the development of robust tools for the analysis of MRIs is now a central field of research in the medical imaging.

7.1.1 Consistent quantification of longitudinal atrophy for clinical applications

Among the different techniques for the quantification of the brain structural changes we can identify segmentation based approaches (like the Boundary Shift Integral (BSI) [FreeBorough and Fox, 1997] or SIENA [Smith et al., 2002]), and non-rigid registration based ones (for instance voxel compression maps (VCM) [Fox et al., 2001], RAVENS maps [Resnik et al., 2000] and cortical pattern matching (CPM) [Thompson et al., 2003]). Non-rigid registration is a powerful instrument which found application in several research context, since it provides a rich description of the atrophy process which ranges from the local (voxel) to the regional level. However, in spite of its large employment in research, non-rigid registration is not very diffuse in the clinical setting, for example for the longitudinal atrophy quantification in clinical trials. This is partly due to the higher technical requirements asked in the clinical context in terms of accuracy, robustness to the biases affecting the medical images, and stability of the measures over time. The failing in controlling these factors inevitably leads to the decreased sensibility of the atrophy measures, and thus to the potential failing or increase in cost of the trial.

The scenario was recently pointed in [Fox et al., 2012]. This interesting paper identifies a set of "quality criteria" that an imaging tool should satisfy in order to find application in the clinical setting:

- *Biological plausibility.* The algorithm should provide atrophy measurements consistent with the known pathophysiology.
- *Symmetry.* The atrophy quantified from A to B should be consistent with the one quantified from B to A.
- *Transitivity.* The atrophy quantified from A to C should be equivalent to the cumulative one from A to B and B to C.
- *Comparison with the "state of art".* The atrophy measurements should be validated on shared data and compared to those obtained from more established algorithms.
- *Reproducibility on back-to-back images.* The group average on same days scans should be zero.

- *Statistical validation.* The accuracy of the measurements should be evaluated by sample size analysis based on the differential progression between AD and normal aging.

In Chapter 6 we proposed the regional flux analysis of the one-year changes in AD, based on non-rigid registration of follow-up images. The framework automatically defines a set of consistent group-wise atrophy regions for AD, which are then used to provide powered measurements of the longitudinal structural changes. In light of these encouraging results, it is therefore interesting to assess the reliability of the flux analysis on the above mentioned “quality criteria”, and to benchmark it on public data with respect to validated methods. However, since the flux analysis proposed in Chapter 6 does not rely on prior hypothesis on the location of the regional atrophy, a different approach should be introduced for the atrophy quantification in apriori regions.

Aim of this work is to provide a framework based on the flux analysis for the quantification of the longitudinal atrophy in the hippocampi and ventricles. After recalling the basic concepts of the flux analysis of deformation fields we detail in Section 7.3 the proposed framework for the quantification of the regional longitudinal atrophy. Finally, in Section 7.4 we validate the framework by testing the above criteria on the ADNI longitudinal images (baseline, 12, and 24 months) from a group of healthy subjects and AD patients.

7.2 Vector Field Divergence to Quantify the Observed Atrophy

We recall here the basic concept introduced in the previous chapter.

Let consider the longitudinal changes between a pair of follow-up brain images estimated by the LCCDemons non-rigid registration. The associated diffeomorphism $\varphi = \exp(\mathbf{v})$ densely represents the local atrophy as a complementary compression/expansion process across adjacent areas. The compression models the shrinking of the anatomical structures due to the observed matter loss, while the expansion is a complementary process which indicates growth, for instance of the CSF areas in the ventricles, or in the sulci surrounding the gray matter. These processes are induced by the estimated deformation field and can be quantified by the flux of the vectors across the boundary of the regions: the inward (resp. outward) flow across a surface induces the compression (resp. expansion), which quantifies the atrophy (resp. growth).

The flux is is the mathematical formulation of the boundary shift, and is identified by the divergence $\nabla \cdot \mathbf{v}$ associated to the field $\mathbf{v}$ (Figure 7.1). In fact, from the Divergence (or Ostrogradsky’s) theorem, the integral of the divergence of a vector field in a given region is the flux of the vector field across the boundaries of the region. The rate of volume change of the region is then the integral of the divergence over the volume:

$$\frac{\int_{\Omega} \nabla.\mathbf{v}\, d\omega}{\int_{\Omega} d\omega} = \frac{\int_{\partial\Omega} \mathbf{v} \cdot \mathbf{n}\, ds}{Vol(\Omega)},$$

We finally note that the areas of maximal/minimal divergence automatically identify the spatial locations of expansion/compression, i.e. involved in the process of matter loss[Lorenzi et al., 2012d]. In the following, the divergence associated to the pairwise deformations is used to localize the areas of relevant longitudinal atrophy and to quantify the associated rate of volume change.

7.3 Measurement of the Hippocampal and Ventricular Longitudinal Changes in AD

Given a sequence of follow-up images I_i $(i = 0, \ldots, N)$ for a given subject, the proposed framework is composed by the following steps.

7.3.1 Alignment of the Sequence to the Template Space

In this step (Processing Step 1) the images are aligned and normalized to a pre-defined anatomical template estimated from a group of healthy elderly subjects of the ADNI cohort. The alignment to the Template space is needed for the subsequent propagation of the anatomical regions through non-rigid registration. The global affine transformation is estimated by the FLIRT software [Jenkinson and Smith, 2001]. The resampling is performed by linear interpolation on the intensities.

We notice that all the images undergo only one interpolation, and are therefore consistently processed in order to not introduce biases on the intensities due to asymmetric resamplings [Yushkevich et al., 2010].

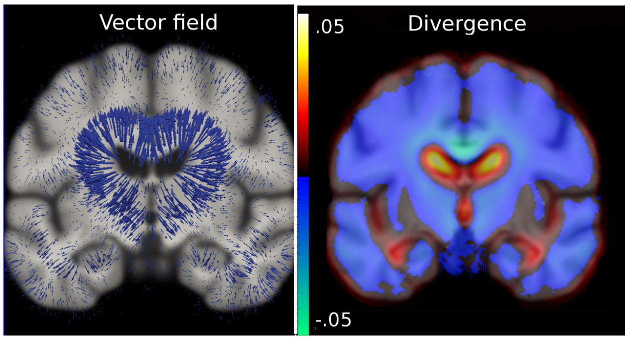

Figure 7.1: Divergence associated to a vector field. Left: vector field of a longitudinal deformation in Alzheimer's disease. Ventricles and temporal lobes are the region of higher flux (vector flow) from the CSF areas to the gray/white matter ones. Right: Divergence associated to the vector field. The areas of maximal/minimal divergence (ventricles, temporal lobes) are those of higher volume change.

Processing Step 6 Consistent alignment of the time series.

Given a sequence of follow-up images I_i $(i = 0, \dots, N)$:

1. Estimate the "9 parameters affine" global transformation to the baseline $A_i : I_0 \simeq I_i \circ A_i$ $(i = 0, \dots, N)$.
2. Skull strip the baseline I_0 (ROBEX software [Iglesias et al., 2011]). Mask the I_i $(i = 0, \dots, N)$ with the estimated brain mask to get I_i^M.
3. Refine the initial transformation. Estimate the "9 parameters affine" global transformation A_i^M: $I_0^M \simeq I_i^M \circ A_i^M$ $(i = 0, \dots, N)$.
4. Register the baseline I_0^M to the template space T. Estimate the 12 parameters global affine transformation A_0^T: $T \simeq I_0 \circ A_0^T$.
5. Compute the aligned time series $I_i^T = I_i \circ \left(A_0^T \circ A_i^M \circ A_i\right)$.

7.3.2 Definition of Consistent Spatial Regions of Atrophy

Prior group-wise regions for the quantification of the hippocampal and ventricular longitudinal changes were defined in the template space T. The regions were estimated from a mixture of anatomical segmentation and of prior information of the longitudinal AD atrophy. The longitudinal atrophy in AD was estimated from a group of AD patients from the ADNI dataset [Lorenzi et al., 2011a], and is here quantified by the divergence of the modeled average longitudinal progression (Figure 7.2A'). The regions were defined as follow:

- Region of ventricular expansion R_v. The prior region of ventricular expansion was decomposed in two complementary parts $R_v = R_{v-} \cup R_{v+}$ (Figure 7.2A) of respectively compression and expansion (red and yellow in the figure). These areas are defined by the maximal and minimal average divergence (Figure 7.2A') within a predefined ventricle mask (Figure 7.2A", blue).

- Region of hippocampal atrophy R_h. The prior region of longitudinal hippocampal atrophy was decomposed in two complementary parts $R_h = R_{h-} \cup R_{h+}$ of respectively hippocampal atrophy and temporal horn expansion. The first one (R_{h-}) is the anatomical mask of the hippocampi computed by segmentation propagation in the template space of the automatically segmented ADNI subject-specific hippocampal masks [Patenaude et al., 2011] (Figure 7.2A, green). The resulting probabilistic hippocampal mask is the area for the quantification of the longitudinal matter loss. The second one (R_{h+}) is defined similarly for the ventricles from the locations of maximal average divergence in the hippocampal mask (Figure 7.2A" red), and encodes the expansion of the temporal horn which is complementary to the hippocampal atrophy (Figure 7.2A purple).

The subject specific regional longitudinal changes are computed by following the Processing Step 7.

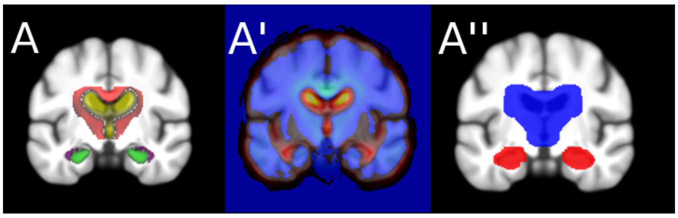

Figure 7.2: Prior region of longitudinal atrophy in AD. A) Prior anatomical areas for the hippocampal (purple and green), and ventricular (yellow and red) expansion and contraction. A') Average divergence map for the longitudinal atrophy in AD (from [Lorenzi et al., 2011a]). A") Ventricular and hippocampal mask for the extraction of the maximal/minimal divergence areas.

```
**Processing Step 7** Quantification of subject-specific regional atrophy.
Given the sequence of aligned follow-up images $I_i^T$ $(i = 0, \ldots, N)$:
1. Non linearly register the follow-up images to the baseline with the LCC-Demons algorithm. Estimate $v_i$ such that $I_0^T \simeq I_i^T \circ \exp(v_i)$.
2. Compute the average longitudinal divergence map $D = \overline{\nabla . v_i}$.
3. Transport the prior regions $R_h$ and $R_v$ in the subject space through the subject-to-template deformation to define $R_v^s$ and $R_h^s$.
4. Restrict the hippocampal region to the subject specific areas of compression/expansion:
       $R_{h-}^s \cap \{x | D(x) < 0\}$,
       $R_{h+}^s \cap \{x | D(x) > 0\}$.
5. Define the atrophy rate at the time point $i$ as the algebraic sum of the average divergence $D_i$ in the compression and expansion areas of the resulting ventricular and hippocampal regions.
```

7.4 Longitudinal Atrophy on the ADNI Dataset

The presented method was applied for the quantification of the longitudinal hippocampal atrophy in a sample of 96 AD subjects and 160 healthy controls from the ADNI dataset. Images of 0, 12, and 24 months were aligned according to the Step 6 and the longitudinal atrophy was evaluated as in Step 7 to test the following quality criteria:

- *Consistency with the clinical condition.* As indicated by Table 7.1 the AD group has significantly higher ventricular expansion and hippocampal atrophy for all the considered intervals ($p < 0.001$, standard t-test). The estimated atrophy rates are consistent with those reported in literature [Frisoni et al., 2010, Schott et al., 2010, Leung et al., 2010].

- *Symmetry.* The longitudinal atrophy measure is perfectly symmetric, due to the symmetry of the registration algorithm. Therefore the absolute changes measured from A to B are equal (with opposite sign) to those from B to A.

	Hippocampi		Ventricles	
	Ctrls	AD	Ctrls	AD
[0-12]	2.38 (1.64)	5.28 (2.38)	1.89 (2.09)	4.03 (2.79)
[0-24]	3.52 (2.04)	10.09 (4.5)	3.56 (2.82)	8.9 (5.32)
[12-24]	1.19 (1.4)	4.89 (2.94)	1.72 (2.19)	4.9 (3.3)

Table 7.1: Estimated percentage atrophy rates (SD) in the ventricular and hippocampal regions for the pairs T12-T0, T24-T0, and T24-T12.

- *Linearity over two years.* Table 7.2, first row, shows the estimated mean and standard deviation for the ratio of the estimated atrophy between 2- and 1-year atrophy rate. The ratios are never significantly different from the reference value of 2.

- *Transitivity.* Table 7.2, second row, shows the compatibility in time of the atrophy measures computed as the error between the measure from A to C and the cumulative one from A to B and B to C. As indicated, the transitivity error is never significantly different from 0, even though it is close to significance for the hippocampal atrophy in AD. We notice that this error is however small relatively to the atrophy rate at 24 months (about 1%).

	Hippocampi		Ventricles	
	Ctrls	AD	Ctrls	AD
[0-24]/[0-12]	1.77 (1.19)	1.98(0.67)	1.48 (5.65)	2.65 (3.96)
p	0.44	0.8	0.39	0.11
[0-12]+[12-24]-[0-24]	0.04 (0.3)	0.09 (0.5)	0.05 (0.61)	0.08 (0.75)
p	0.1	0.08	0.28	0.3

Table 7.2: Linearity and transitivity of the estimated atrophy rates. First row: mean (SD) of the ratio 2-years over 1-year atrophy. The p-value indicates the significance of the difference relative to the reference value of 2. Second row: mean (sd) of the transitivity error. The p-value indicates the significance of the difference relative to 0 (paired t-test).

- *Sample size analysis.* Based on the reported atrophy rates, we estimated the sample size required to detect a 25% difference in the AD longitudinal progression relative to the normal aging (80% power, 0.05 significance). The sample size (Table 7.3) are in line with those reported in the previous studies [Leung et al., 2010, Schott et al., 2010].

7.5 Conclusions and Perspectives

We presented a framework based on the flux analysis of vector fields for the quantification of the longitudinal hippocampal and ventricular changes in AD. The frame-

	[0-12]	[0-24]
Hippocampi	169 (119,255)	117 (89,162)
Ventricles	426 (249,880)	249 (168,410)

Table 7.3: Sample size analysis provided by the estimated atrophy rates. Average sample size (95% CI) to detect a 25% difference in the AD progression relative to the normal aging with 80% power and significance level of $p = 0.05$.

work estimates the longitudinal changes by non-rigid registration performed by the LCC-Demons, a robust and symmetric non-rigid registration algorithm, and quantifies the atrophy by integration of the flux of the vector fields on consistently defined group-wise regions. Experimental results indicate accurate and consistent quantification of the longitudinal atrophy, which lead to statistically powered results. The proposed method does not rely on the segmentation of the anatomical structures, but is based on the propagation of prior regions of longitudinal atrophy defined in a template space. Thus it can be easily adapted for the atrophy quantification in different areas, identified in a general way. For instance, the ventricular region used in this work was defined from the divergence estimated in a previous study. Such a region is consistent with the registration framework and represents the expected areas of longitudinal atrophy and CSF expansion. Being able to easily define more general regions might be of relevant importance in a clinical trial setting, since it allows the investigation of the drug efficacy on more complex atrophy patterns than the one provided by the single measurement from a specific region, and might finally lead to more accurate and powered quantifications.

Part IV

Disentangling the Normal Aging from the Pathological AD progression

Chapter 8

Quantifying the Pathological Atrophy After Detection and Removal of the Normal Aging.

Contents

Longitudinal models have interesting applications in the cross sectional setting. This chapter was presented in [Lorenzi et al., 2012e] and introduces the projection of brain anatomies on a spatio temporal atlas of the healthy aging, in order to separately analyse accelerated aging and abnormal pathology-specific atrophy.

The morphology observed in the brain of patients affected by Alzheimer's disease (AD) is the contribution of different biological processes such as the normal aging and the AD-specific pathological matter loss. The ability to differentiate these complementary biological factors is fundamental in order to reliably evaluate the pathological AD-related structural changes, especially at the earliest phase of the disease, at prodromal and pre-clinical stages. We propose a method based on non rigid-registration to estimate the different contributions of these complementary factors, and to identify the brain structural changes which are specific for the pathological component. The experimental results provide a description of the anatomical changes observed *across the AD time span: normal aging, normal aging at risk, conversion to MCI and latest AD stages. More advanced AD stages are associated to "virtually older" brains, and to increased specific morphological changes that are not related to the normal aging. These results provide new insights that can lead to new understandings of the AD dynamics, and to novel techniques for the modeling and the early detection of the disease.*

8.1 Introduction

The objective of computational anatomy applied to neurodegenerative diseases such as Alzheimer's disease (AD) is the understanding of the pathological changes affecting the brain morphology. This is particularly relevant for monitoring the disease evolution in clinical trials and for diagnostic purposes [Frisoni et al., 2010, Scahill et al., 2002].

However, the morphology of the brain affected by AD is not completely related to the disease, especially in asymptomatic and prodromal stages, and is the consequence of specific biological processes:

- *Age related anatomical changes.* It is well known that the healthy aging is characterized by the progressive deterioration of the brain structural integrity [Long et al., 2012] which involves essentially hippocampal loss and ventricular enlargement.

- *Disease related anatomical changes.* AD involves a specific pathological process which was demonstrated to be complementary to the healthy aging [Nelson et al., 2011, Barnes, 2011], and to produce patterns of neurodegeneration in specific areas which cannot be ascribed to any kind of global accelerated aging process [Frisoni et al., 2010].

If we could independently model these physiological changes it would then be possible to describe a given anatomy as the contribution of distinct and complementary factors, each of them representing a precise biological process. Such decomposition would be extremely interesting not only for the improvement of the understanding of the disease, by removing sources of variability not related to the pathology, but also for clinically oriented purposes, such as the early diagnosis and the development of drugs aimed to target the disease specific component.

However, such a decomposition comes with a number of issues that must be dealt with. For instance, it is important to notice that, although induced by completely different biological mechanisms, aging and AD often map to common areas, and the correct identification of the respective contributions may be difficult, especially in morphometric studies. Moreover it is plausible that these phenomena are not completely independent, and might interact in a kind of positive "feedback" process. Thus, the increase of the specific changes leads to an accelerated global aging process in the long term. This hypothesis is supported by recent studies on the estimation of aging indices based on the structural MRI of the brain

[Franke et al., 2010, Davatzikos et al., 2009]. For instance, in [Franke et al., 2010] the authors showed a strong correlation between the predicted age and the biological one, but estimated a gap of $+10$ years for subjects with AD.

The reliable estimation of the aging component is also relevant for modeling the evolution of the disease and for the subsequent statistical analysis. For example, when comparing the longitudinal observations from different clinical groups at different aging stages it is crucial to correctly position the observations on the time axis. This is not an evident task, since the disease appears at different ages, and biologically older brains might have greater structural integrity than younger ones affected by the pathology. For this purpose it is very important to define a“virtual” aging stage relative to a reference anatomical evolution.

The objective of this work is to introduce a framework for the identification and the disentanglement of the biological processes due to aging and pathological changes. In particular, by following the model which relates the development of AD to the abnormal processing of beta-amyloid (Aβ) peptide [Jack et al., 2010b], we investigate the atrophy patterns in healthy subjects positive to the CSF Aβ42 marker, in MCI converters to AD, and finally in AD. The method is based on the diffeomorphic non rigid-registration and is detailed in Section 8.2. In Section 8.3 we show that such framework provides an accurate description of the anatomical changes across the AD stages, which can find effective applications in the modeling of the disease and for diagnostic purposes.

8.2 Projecting the Brain Anatomy on the Healthy Aging Trajectory

Given a subject k, we model the brain anatomy I_k observed in a magnetic resonance image (MRI) by non-rigid registration to a pre-defined reference anatomical space T. If we parameterize the subject-to-template deformation ϕ_k by a stationary velocity fields (SVFs) w_k such that $\phi_k = \exp(w_k)$, the observed anatomical structure is then described by the SVF w_k, which is a tangent vector field in the deformation space.

By taking advantage of the log-Euclidean nature of the SVF, we assume that w_k is the contribution of the normal aging plus a complementary component: $w_k = w^k_{age} + w^k_{specific}$.

The proposed framework analyzes these different components by describing the observed anatomy in separate modeling steps which respectively address:

1. Identification and extraction of the aging component w_{age} by estimation of a “virtual age” with respect to a reference evolution for the normal aging.

2. Identification and analysis of the remaining specific component $w_{specific}$. The specific component describes the cross-sectional changes which cannot be attributed to the aging, and which encode the pathological atrophy.

Each modeling step is separately addressed in the following sections.

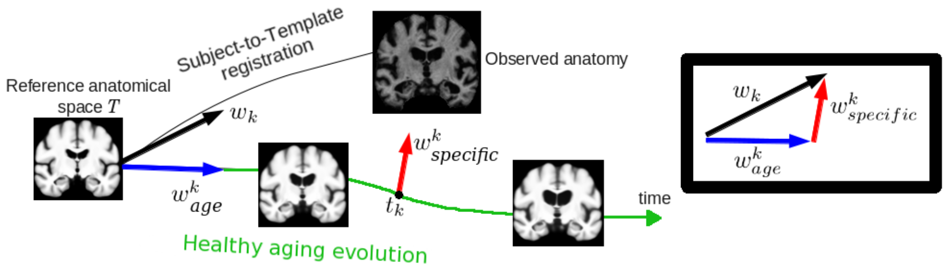

Figure 8.1: An observed anatomy can be described in terms of an aging factor plus a subject specific component not related to the healthy aging.

8.2.1 The "Virtual Age" with Respect to a Model of Healthy Aging

We want to differentiate the morphological patterns in the image I_k due to the normal aging from those related to different biological processes.

We consider a model of the healthy aging defined in a reference anatomical space T. As proposed in [Lorenzi et al., 2011a] we assume that the aging process is stationary and linearly evolving according to the SVF μ_0, so that the aging is defined as the trajectory $\mu(t) = t\mu_0$.

Theoretically, given a longitudinal evolution $\exp(\mu(t))$ for the healthy aging in a reference anatomy T, we want to project the subject's anatomy I_k on the "closest" point of the trajectory $T \circ \exp(\mu(t))$ in order to determine its progression stage t_k with respect to the evolution. Defining $\exp(w_k)$ as the subject-to-template deformation, and given a metric $<, >$ on the tangent space, the projection of the image I_k in the trajectory $T \circ \exp(\mu)$ is given by the decomposition of the vector into orthogonal components $w_k = w^k_{age} + w^k_{specific} = t_k\mu_0 + \nu_k$. In the present work the projection is based on the standard L^2 metric.

In such decomposition the time point t_k defines a "virtual age" index of the subject k with respect to the model μ, while the vector field ν_k encodes the morphological changes which cannot be related to the aging process (Figure 8.1). The time point t_k defines the projection on the longitudinal evolution $\mu(t)$ and is given by the whole brain average of the voxel-by-voxel (L^2) projections: $t_k = \frac{<w_k,\mu_0>_{(x)}}{||\mu_0||^2_{(x)}}$. Once t_k is determined, the specific vector component is simply computed voxel-wise as $\nu_k = w_k - t_k\mu_0$.

By estimating the time point t_k on the whole brain we make a precise assumption on the aging process, which is here defined *globally*. Therefore, the accelerated aging is constrained with respect to the model $t\mu_0$, and any local departure from it (for instance in some specific regions), is interpreted as a *specific* morphological change, independent from aging. On the contrary, by considering only regional projections on specific areas (for instance hippocampi or ventricles) we may mistake specific patterns of neurodegeneration as global accelerated aging, and thus introduce a bias in the decomposition.

8.2.2 Identification and Analysis of the Specific Component

The removal of the factor $t_k\mu_0$ allows to directly compare across subjects the remaining component $w^k_{specific} = \nu_k$, which encodes the variability that cannot be attributed to the normal aging. In this section, we investigate the ability of such component to correctly encode the information inherent the pathology, in order to reliably discriminate between different clinical populations.

8.2.3 Divergence Associated to the Specific Components

We are interested in the analysis of the specific *matter loss* which characterizes different clinical groups. The diffeomorphic constraint of the non-rigid registration encodes the morphological changes as a complementary compression/expansion process across adjacent areas. The compression models the shrinking of the anatomical structures due to the observed matter loss, while the expansion is a complementary process which indicates growth, for instance of the CSF areas in the ventricles or in the sulci surrounding the gray matter. These processes are induced by the estimated deformation fields and can be quantified by the flux of the vectors across the boundary of the regions: the inward (resp. outward) flow across a surface induces the compression (resp. expansion) which quantifies the atrophy (resp. growth).

The compression/expansion processes are identified by the divergence $\nabla \cdot \nu_k$ associated to the vector component ν_k. We recall that from the Divergence (or Ostrogradsky's) theorem, the integral of the divergence of a vector field in a given region is the flux of the vector field across the boundaries of the region, and that the flux is the mathematical formulation of the boundary shift [Lorenzi et al., 2012d]. Since the regional divergence is the flux across regions, it measures the percentage matter loss.

8.2.4 Discriminative analysis on the specific component

In the present analysis we tested the ability of the divergence maps $\nabla \cdot \nu_k$ to discriminate between a set of patients P and a control group C.

We computed the voxel-by-voxel effect size map for the group-wise divergence $ES = (mean(\nabla \cdot \nu_P) - mean(\nabla \cdot \nu_C))\,/sd(\nabla \cdot \nu_P)$ which quantifies the magnitude of the differences between patients and control populations. We chose a set of regions relevant for AD (hippocampi, medial temporal lobes (MTL), posterior cingulate (PC), and ventricles) where we identified the voxels of maximal positive and negative effect size. These voxels were then inflated and symmetrized in order to define a set of regions for the discriminative analysis (Fisher's discriminant analysis) of the flux associated to the specific component. The discriminative analysis was performed by leave-one-out cross validation to test the correct group classification.

8.3 Virtual Aging and AD Specific Atrophy on the ADNI Dataset

We chose the ADNI structural MRIs for 57 healthy subjects with normal levels of CSF Aβ42 ($>$ 192 pg/ml, group Aβ-), 41 healthy subjects with abnormal levels (group Aβ+), 86 subjects with mild cognitive impairment who consequently converted to AD (group MCI_{conv}), 110 MCI subjects who remained stable during the observation period (group MCI_{stable}), and 134 AD patients (group AD). Demographical as well clinical information are based on the ADNI data updated to March 2012, with a follow-up period of 3 years from baseline.

Previous studies showed that healthy elders with pathological CSF Aβ42 levels ($> 192pg/ml$) have a more pronounced brain atrophy progression [Lorenzi et al., 2011a, Fjell et al., 2010, Tosun et al., 2010], which might be a marker of pre-symptomatic stage of AD. Therefore we defined the healthy aging progression by considering only the Aβ- group as reference healthy population. The longitudinal observations (from baseline to 3 years) for the Aβ- group were used to model the reference healthy evolution μ_0 [Lorenzi et al., 2011a] normalized to an anatomical reference T estimated from the ADNI healthy population.

In order to unbias the analysis with respect to the healthy (Aβ+) population, we centered the SVFs by subtracting the average subject-to-Template SVF of the Aβ- group.

The unbiased SVF were then analyzed by following the proposed framework, to show that advanced AD stages are associated with accelerated aging plus a disease specific anatomical pattern. The effectiveness of the disease specific component in encoding information relevant to the pathology was tested by performing two different discriminative analysis on the classification between AD vs healthy, and MCI_{conv} vs MCI_{stable}.

8.3.1 Estimated virtual aging

The normal aging modeled for the Aβ- group is shown in Figure 8.2 (left), and is characterized mainly by the ventricular enlargement and by atrophy in the temporal areas. The estimated virtual age is significantly correlated with the biological one for all the considered groups (minimum Pearson's r for the MCI_{conv} (0.3) and maximum for the MCI_{stable} (0.54), $p < 0.005$) . However, even though the considered groups did not significantly differ for age, the virtual age increases as the clinical condition gets closer to AD. In fact, as shown in Figure 8.2, Aβ+, MCI_{conv}, and AD are increasingly virtually older when compared to the healthy Aβ- (p-values in the boxes). Interestingly, MCI_{conv} are significantly older than MCI_{stable} (p=0.035), to indicate a possible accelerated aging process induced by the ongoing AD.

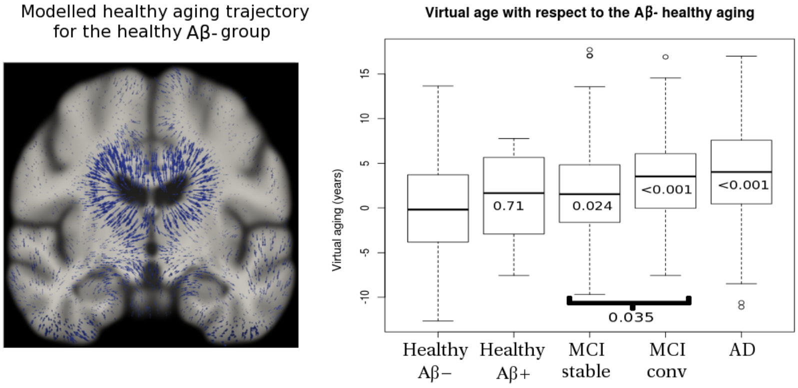

Figure 8.2: Left: Normal aging modeled for the group of Aβ- healthy subjects. Right: Average virtual age estimated for the clinical groups with respect to the normal aging. The estimated virtual ages describe statistically significant older brains (standard t-test, p-value in the boxes) with respect to the healthy Aβ- for all the considered groups. Interestingly, MCI converters are "virtually older" than the MCI stables ($p < 0.0392$).

8.3.2 Analysis of the specific component

Figure 8.3 shows the average specific deformation components ν_k associated to the different groups once centered with respect to the healthy population. The morphological changes specific for the healthy Aβ+ are mild, while the changes specific for the MCI converters are more pronounced and map to the frontal cortex, ventricles, temporal poles, entorhinal cortex and hippocampi. The same pattern is appreciable for the AD patients.

In Figure 8.3, second row, we notice that the change in the clinical condition (from Aβ+, to MCI_{conv} and AD) is associated with larger and more intense divergence patterns (i.e. flux across regions). For each anatomical region we can identify the associated location of high positive divergence (growth of the CSF regions), and the correspondent area of high negative divergence (brain atrophy), which indicate more intense expansion/compression mapping mainly to ventricles, temporal poles and hippocampi.

Figure 8.4 shows the effect size between the divergence maps of respectively MCI converters vs stable, and AD vs healthy controls. As expected, the effect size between AD and healthy controls is higher than the one between MCI converters and stables, to indicate the larger variability in the MCI group.

Finally, Table 8.1 shows the regional and pooled prediction accuracy in the discriminative analysis between AD vs $Ctrls$, and MCI_{conv} vs MCI_{stable}. The fair classification results (91% sensitivity, 84% specificity for AD vs Ctrls, and 67%, 63% for MCI_{conv} vs MCI_{stable}) indicate the ability of the specific pathological component to encode information relevant for the disease condition and the clinical group. The provided predictions are significantly better than those given by pure

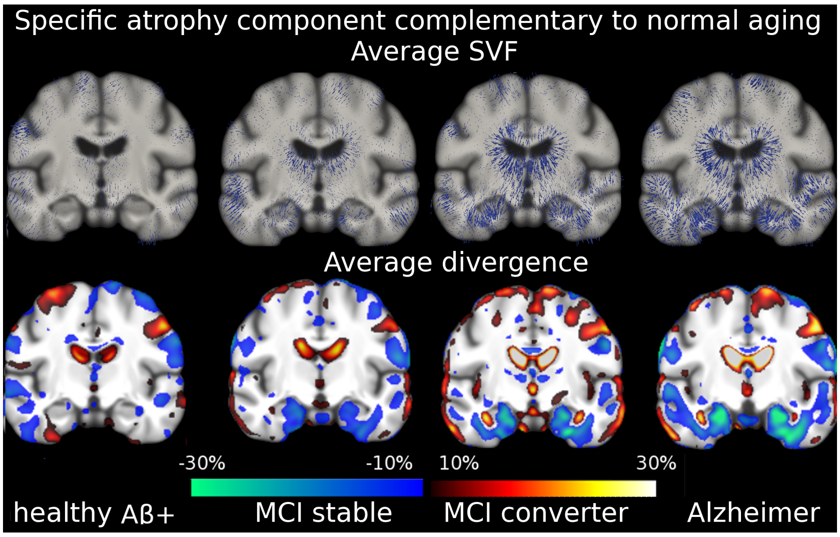

Figure 8.3: First row: average specific deformation component not related to normal aging. MCI converters and AD patients show the more pronounced pattern of morphological changes mapping mainly to ventricles, temporal poles, entorhinal cortex and hippocampi. Second row: percentage matter loss measured by the average divergence maps extracted from the specific component.

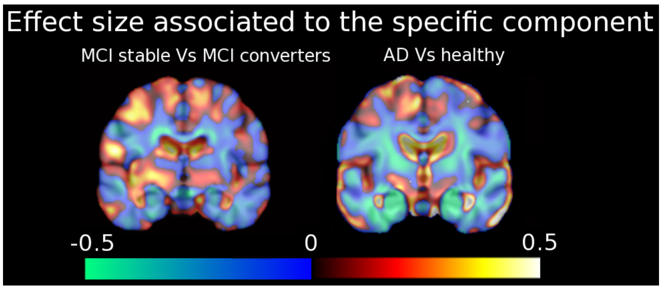

Figure 8.4: Effect size associated to the divergence maps of the specific components.

chance ($p < 0.001$, McNemar's Chi-Square test), and are in line with those available in the literature on the ADNI dataset [Chupin et al., 2009a, Cuingnet et al., 2011, Chincarini et al., 2011, Wolz et al., 2011].

8.4 Conclusions and Perspectives

We proposed a method to decompose the brain atrophy into complementary components: aging and AD specific. These components identify different clinical stages, and are compatible with the hypothesis that points to the positivity to the CSF Aβ42 as a presymptomatic marker of AD in the healthy stages. We showed that

	AD vs $Ctrls$					MCI_{conv} vs MCI_{Stable}			
	Sens	Spec	PPV	NPV		Sens	Spec	PPV	NPV
All features	**91**	**84**	**85**	**90**		54	54	54	54
MTL (-)	86	81	85	82		53	51	52	52
MTL (+)	73	77	76	74		57	57	57	57
Hippocampi (-)	77	71	75	73		55	47	51	51
Hippocampi (+)	77	63	73	67		**67**	**63**	**64**	**65**
Ventricles (+)	65	69	68	66		61	43	52	52
Ventricles (-)	68	69	69	68		58	56	57	57
PC (-)	58	59	59	59		58	58	58	58
PC (+)	59	50	54	54		47	74	64	58

Table 8.1: Regional classification accuracy for the leave-one-out discrimination. The analyzed features are the positive and negative flux (+ and -) of the specific component across the regions of interest.

more advanced AD stages (from Aβ+ to MCI converters, and finally to AD) are associated to both "virtually older" brains, and to increased specific morphological changes not related to the normal aging.

Different MRI-based indices of brain aging were proposed in the past [Franke et al., 2010, Davatzikos et al., 2009]. Our model integrates these approaches into a richer description of the AD process. In fact we showed that AD is *not only* represented by accelerated brain aging, but is also composed by a specific and complementary quote of atrophy. While confirming the results from the other studies, our method points to a completely different conclusion. Since AD is not only an accelerated aging process, the design of *disease specific* modifying drugs which do not have impact on the natural normal aging is then justified.

To conclude, our approach provide new insights which may help the understandings of the AD dynamics, and which might promote the development of novel diagnostic techniques for the early detection of the disease.

Chapter 9

Conclusions and Perspectives

Contents

9.1 Scope of the Thesis

The study of Alzheimer's disease poses several challenges in terms of modeling and development of computational methods for the effective analysis of imaging data. In this thesis we presented a computational framework for the analysis of longitudinal T1 brain MRIs which satisfies precise research and clinical needs in term of efficiency, reliability and robustness. We built upon state-of-art methods for designing a toolkit that could find application in both image processing and clinical research fields.

The proposed instruments are computationally efficient and can be reliably applied to medical images. For instance, the LCC-Demons was designed for dealing with the acquisition biases, is fully automated and computationally cheap. All the proposed tools rely on open source software and can be easily shared and deployed on different systems.

The toolkit was designed to find application in the clinical research on Alzheimer's disease. The proposed methods were mainly tested on large and publicly available data, so we could *benchmark and compare* the results with the available literature and state of art methods.

Finally, the last part of the thesis was dedicated to the *translation* to the clinical domain. We defined flexible and robust measures of cerebral atrophy, with explicit clinically oriented purpose. Particular attention was given to the definition of plausible measures which could be compared with the standard ones used in clinic, as *percentage volume changes*, and that could be easily interpreted from the biological point of view, such as the *virtual age* relative to aging models.

9.2 Contributions

In chapter 2, we proposed the LCC-Demons registration framework. This tool was extensively tested and applied on different settings, and showed good results in terms of robustness, reliability, and efficiency. It might thus represent a valuable instrument for the analysis of large dataset from multicentric studies. We are currently preparing a future release of the software, similarly to the Symmetric Log-Demons[1]. Moreover, we are currently working on the ITK implementation of the stationary velocity field class, which will include the methods described in this work for the stable computation of the Jacobian matrix and determinant, and for the parallel transport.

The parallel transport of longitudinal trajectories is currently a topic of active research and several questions are still open. However, the material presented in chapter 3 initiated the investigation of the parallel transport on a new basis, by digging into the geometrical properties which one can endow on a manifold by moving forward with respect to the classical Riemannian setting proposed with LDDMM. Different applications of the Pole Ladder are currently under study, for instance for the group-wise modeling the cardiac cycle, which intrinsically involves longitudinal and inter-subject analysis.

We showed in chapter 4 that the Lie group theory offers a rich geometrical setting for the definition of geodesics and transport methods. The Cartan-Shouten affine connection space setting offers new perspectives with respect to the Riemannian approach built upon the Levi-Civita connection, and might promote the investigation of novel affine connections for parallel transporting vectors, for instance by requiring the preservation of specific motion properties. From the practical point of view, the proposed parallel transport are already a valuable tool for the longitudinal analysis of follow-up images. For instance, in chapter 5 we experienced the increased accuracy in analysing the transported longitudinal trajectories rather than the standard Jacobian determinant scalar values.

The hierarchical model presented in chapter 5 is now a fully operative computational tool, and is implemented on grid-based research infrastructures (NeuGRID[2] and NeuroLog[3]). The aim is to perform validation studies on large data on dataset different from ADNI, in order to refine and generalize the preliminary findings illustrated in the present thesis. Moreover, the proposed framework is fully generalizable and might find important applications for the definition of spatio-temporal atlases in different domains, like cardiac imaging or brain development in childhood.

In chapters 6 and 7 we introduced the regional flux analysis, a novel approach for the *exploration* and *quantification* of longitudinal morphological changes encoded by deformation fields. The proposed method showed good reliability and accuracy. Chapter 6 proposes a novel setting for the analysis of SVF deformations, which relies on the study of the associated topological properties using the Helmholtz

---

[1] http://www.insight-journal.org/browse/publication/644

[2] http://www.neugrid.eu

[3] http://neurolog.i3s.unice.fr/

decomposition. The volume changes encoded by the deformation field are completely characterized by a pressure potential and novel mathematical instruments can be used to quantify and compare pathological patterns of this new geometrical object. As a scalar function, the pressure can be studied by the Morse Smale theory. Morse Smale studies the topological properties of a function by analyzing the underlying complex defined by the critical points, i.e. the local maxima, minima and saddle points, and the cells defined by the flow from maximum to minimum. In our case Morse Smale theory might provide a novel description of the atrophy through the analysis of the properties of the corresponding complex, like the persistence of the atrophy pattern at different spatial scales and the efficiency of the underlying graph.

From the clinical point of view, further investigations of the flux associated to the pressure potential might provide powerful instruments for the monitoring of the Alzheimer's evolution in the brain, especially at the earliest stages. In fact the flexibility of the method proposed in Chapter 7 can be used to evaluate the atrophy in brain areas which are usually more difficult to segment, for instance amigdalae, parahippocampi or the posterior cingulate, and to combine these measures to define a more precise and robust index of neurodegeneration.

Finally, the work introduced in chapter 8 describes the morphological changes in the brain by *combining longitudinal and cross-sectional analysis*. This model reduces the complexity of the subject-to-template deformation by identifying biologically meaningful components: *virtual aging* and *disease specific atrophy*. The information carried by these complementary parts have precise clinical meaning and might be of relevant interest for diagnostic purposes. In fact the virtual aging could be seen as an index of the structural "brain reserve", i.e. of the resilience of the brain to the pathological effects, while the specific component evaluates the pathological structural damage. These components characterize the morphological pattern of a given brain, and provide informative and quantitative diagnostic indices. The translation of the proposed computational model to clinic requires important validation efforts, and we are currently planning to deepen and further investigate the validity of such a model.

9.3 Perspectives and Future Applications

The work proposed in this thesis is already an effective instrument for the analysis of longitudinal brain structural images in AD. Moreover, due to their generality and reusability, we believe that the proposed tools could find further application for the study of different imaging modalities, and in different domains.

9.3.1 Multimodal longitudinal Atlas of AD

This thesis focused on the modeling of the *structural* changes in the brain affected by Alzheimer's. This is only a preliminary contribution towards the development of a comprehensive model of the disease, which should be based on biochemical, functional, and neuropsychological data, in addition to the pure modeling of the brain atrophy. From the imaging point of view, the proposed longitudinal framework can be extended to a multimodal/multiscale model of amyloid deposition, metabolic and connectivity changes, and gray and white matter atrophy.

For instance, we might consider the multichannel registration of paired MRI and diffusion weighted images (DWI) [Siless et al., 2012], in order to include information about the white matter disruption which is not detectable in T1 MRIs. The tools for the longitudinal statistical analysis and quantification detailed in chapters 4 and 6, as well as the spatio-temporal registration framework proposed in appendix A, can be straightforwardly extended in case of T1+DWI multimodal registration, and provide a more complete description of the longitudinal anatomical changes.

A more complex extension of the model would account for the brain functional activity, for instance mapped by 18F-FDG PET imaging, and for the amyoid deposition detected by 11C-PIB PET (figure 9.1).

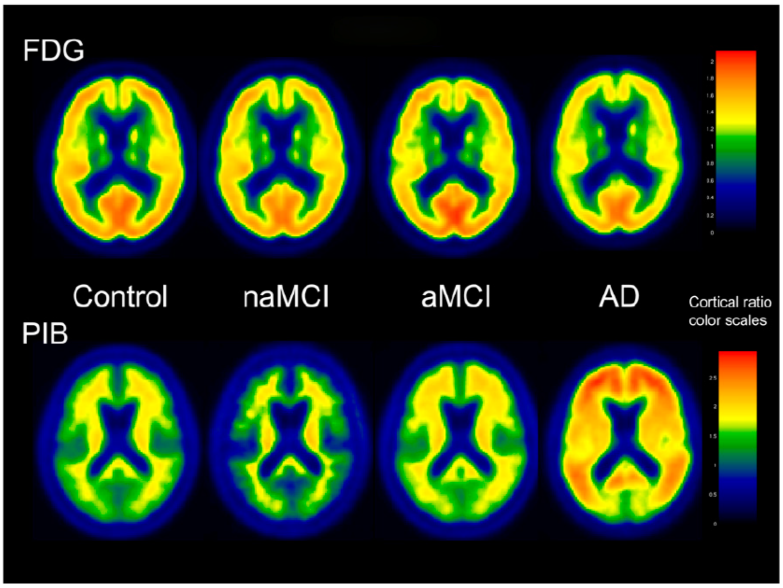

Figure 9.1: Hypometabolism and cortical amyloid deposition across the time span of AD [Lowe et al., 2009]. Group-wise average for the 18F-FDG PET (top) and the 11C-PIB (bottom) images.

The model would enable the testing of specific hypothesis for the disease evolution, such as the amyloid cascade hypothesis [Jack et al., 2010a], and might be extremely valuable for the understanding of the disease mechanisms. In this case, the framework of chapter 8 might be used to temporally align different patients according to the aging stage, and to subsequently model the biochemical and metabolic changes in time. However, the consistent integration of different modalities is challenging, due to the different nature of the acquisition, the partial volume effects, and most importantly to the lack of a valid apriori model of interaction between the different biomarkers.

9.3.2 Spatio-temporal Model of the Cardiac Cycle

Cardiac imaging is a very active field of research where non-rigid registration is used for the modeling of the cardiac motion. When registering the frames of the cardiac sequence we want to capture the properties of the heart cycle, which can be analyzed for disease diagnosis or therapy guidance. For instance, the group-wise estimation of a cardiac atlas finds several applications which include statistical analysis among populations, segmentation of heart structures, disease detection and motion characterization. The problem requires the estimation of the anatomical motion in time through serial observation from different patients, and is therefore purely 4-dimensional.

Recently the log-Demons algorithm was adapted to the estimation of patient specific incompressible cardiac motion [Mansi et al., 2011a], which can thus be described by SVFs.

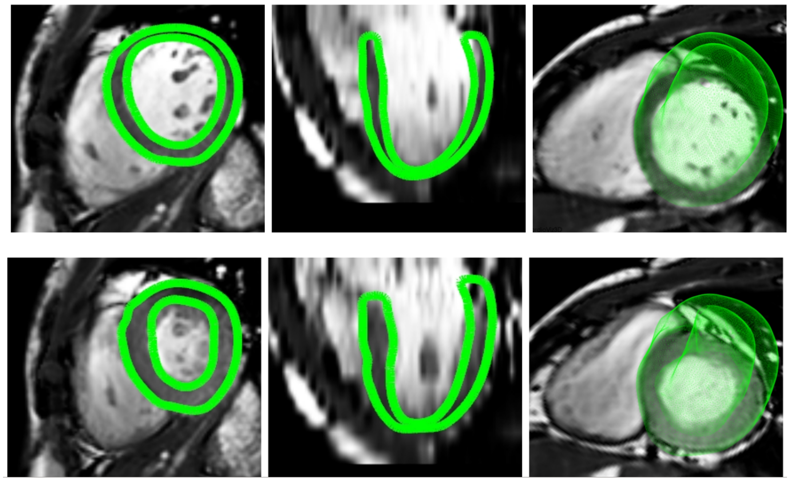

Figure 9.2: Example of incompressible log-Demons based cardiac registration from [McLeod et al., 2012]. Top row: Three views of the reference frame (end diastole) with segmented mask over-laid in green. Bottom row: Same views of peak systole with the segmented reference mask deformed by the computed deformation field.

If we want to develop a group-wise atlas for the heart cycle we need then to transport the longitudinal SVF on a common anatomical reference, and we can thus apply the tools proposed in this thesis. However, the cardiac motion has a completely different nature than the longitudinal anatomical changes in the brain, and is usually magnitude higher. This would require to adapt the proposed transport techniques to this novel context.

9.3.3 Modeling the mass effect in brain tumors

Non-rigid registration finds different applications in brain tumor modeling. For instance, if we are interested in analyzing the longitudinal changes in the brain structure or function, non-rigid registration accounts for brain tissue deformation due to tumor growth (mass effect) [Stretton et al., 2011]. The mass effect itself is a very important index of the tumor evolution, since it causes brain damage and blockage of fluid and can be potentially life-threatening, whether a brain tumor is benign or malignant. Monitoring the longitudinal mass effect is therefore important when following patients in time.

In Appendix B we proposed a regularization scheme for the log-Demons algorithm for registering brain images in presence of tumor, by penalizing the estimation of the deformation in low weight regions (Figure 9.3).

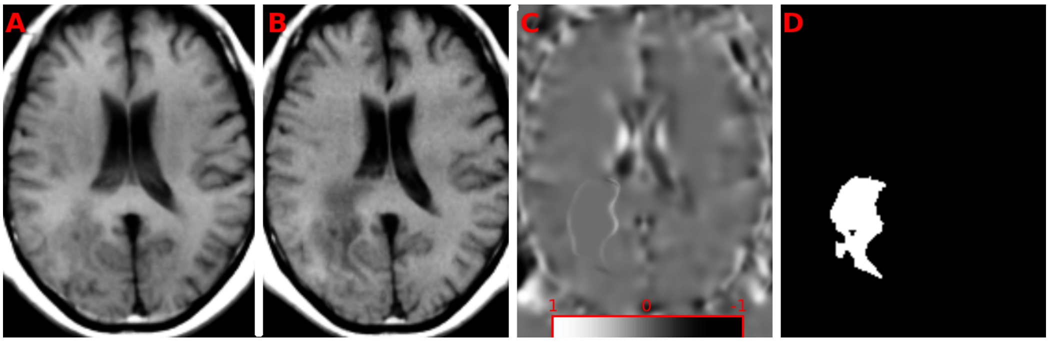

Figure 9.3: Mass effect analysis. A,B) Two-years follow-up sequence of T1 MRIs for a low-grade glioma patient , C) divergence scalar map associated to the longitudinal deformation, D) prior mask for the tumor.

In figure 9.3 we notice the high divergence areas locate in the ventricles, to indicate the swelling due to the tumor growth. We can therefore use the framework proposed in Chapter 6 and 7 to effectively discover and quantify the volume changes induced by the mass effect, in order to monitor the tumor growth and evaluate indirect treatment effects. Contrarily to the Alzheimer's case, we do not have here any prior hypotheses about the location of these changes, and we require a kind of completely automated method to identify consistent and persistent areas of change across multiple time points. As previously observed, Morse Smale theory could help in identifying persistent relationship between local maxima and minima pressure points, and therefore highlight meaningful dynamics of the mass effect.

Part V

Appendix

Appendix A

Log-Demons Spatio-Temporal Registration

This chapter is based on the MICCAI workshop paper [Lorenzi et al., 2010b], and introduces the 4D registration method which is employed in the hierarchical model proposed in [Lorenzi et al., 2011a].

A.A Introduction

The consistent evaluation of changes across serial images is a fundamental requirement to gain in stability and robustness of the measurements, as well as in higher accuracy in detecting biological phenomena like pathological trends. The registration of time series image-data plays a central role in many field of research, like cardiac imaging [Peyrat et al., 2008] or motion analysis [Ren et al., 2009]. In the field of neuroimaging, a 4D registration procedure for serial images was introduced in [Shen and Davatzikos, 2004], where a subject-specific 4D template is warped to match the sequence of serial images. The study introduced the idea of Gaussian smoothing along a multidimensional neighborhood, to impose spatial and temporal constraints on the resulting 4-dimensional deformation field. In [Avants et al., 2007] it was proposed the consistent longitudinal intra-subject diffeomorphic registration with the LDDMM framework. In the study, the diffeomorphisms matching the baseline image to the related serial scans were sampled in a standardized time range to produce a subject-specific description of the temporal trajectory of the brain changes. Another method was presented in [Davis et al., 2007] to perform a regression of the brain shapes as a function of age. Still based on LDDMM, a complete framework for the consistent 4-dimensional registration of shapes was presented in [Durrleman et al., 2009]. However, the high complexity and the important computational requirements often limit or even prevent the use in the practical context, especially for the analysis on volumetric images in longitudinal dataset, due to the increasing number of registrations required.

We propose here a framework based on the log-Demons registration for the temporally consistent diffeomorphic registration of serial MRI data.

A.B Spatio-Temporal regularization in the log-Demons

The framework is based on the log-Demons registration scheme detailed in Chapter 2.

The longitudinal perspective in the registration process increases the dimensionality of the registration and adds a new level of estimation along the temporal dimension. To consistently register a temporal series of images I_i, $i = 0 \dots n$, we propose a hierarchical approach from the statistical multilevel modeling:

- *First level of inference.* We estimate the deformations $\phi_i = \exp(\mathbf{v_i})$, $i = 1 \dots n$, to match each image I_i to the baseline I_0.
- *Second level of inference.* The sequence of $\mathbf{v_i}$ is used to model in the log-domain a subject-specific temporal trajectory $\bar{\mathbf{v}}(t)$.
- *Hierarchical estimation.* The trajectory $\bar{\mathbf{v}}(t)$ is then reintroduced in the first level as a prior term to drive the re-estimation of the deformations at each time point.

The introduction of the new prior term $\bar{\mathbf{v}}(t)$ in the log-Demons can be done at the regularization level (Section 2.2.1), to constrain the solution for the optimal SVF $\mathbf{v}$:

$$E_{\mathrm{reg}}(\mathbf{v}) = \frac{1}{\sigma_x^2}\| \exp(-\mathbf{v}) \circ \exp(\mathbf{v_x})\|^2_{L_2} + \frac{1}{\sigma_t^2}\|\mathbf{v} - \bar{\mathbf{v}}(t)\|^2_{L_2} + \frac{1}{\sigma_T^2}\mathrm{Reg}(\mathbf{v}) \quad (A.1)$$

It can be easily shown that the optimization of the above formula leads to the following optimal solution for the log-Demons regularization:

$$\mathbf{v} = G_\sigma * \left(\frac{\sigma_t^2 \mathbf{v_x} + \sigma_x^2 \bar{\mathbf{v}}(t)}{\sigma_t^2 + \sigma_x^2} \right) \quad (A.2)$$

We notice that the solution is still obtained through Gaussian convolution and is therefore compatible with the log-Demons structure. The optimal SVF $\mathbf{v}$ is the weighted average between the field correspondence field $\mathbf{v_x}$ and the temporal prior $\bar{\mathbf{v}}(t)$. The parameters σ_x and σ_t determine the trade-off between spatial and the temporal information. With this approach, the estimated deformation takes into account the global temporal evolution while remaining consistent with the classical log-Demons registration framework. It has been previously proposed to perform longitudinal registration through regularization of the 4D deformation field in a 4-dimensional neighborhood, i.e. by minimization of the temporal gradient [Shen and Davatzikos, 2004]. That is actually a special case of the presented framework, where the prior $\bar{\mathbf{v}}(t)$ is estimated through kernel regression from the sequence of the $\mathbf{v_i}$.

A.C Preliminar Experiments

The above registration was tested on the longitudinal images acquired for a sample ADNI MCI subject. The deformation trajectory $\mathbf{v}_i$ with respect to the baseline image was computed with the log-Demons, and the temporal evolution $\bar{\mathbf{v}}(t)$ was estimated through a linear model in time. The fitted $\bar{\mathbf{v}}(t)$ was then used to constrain

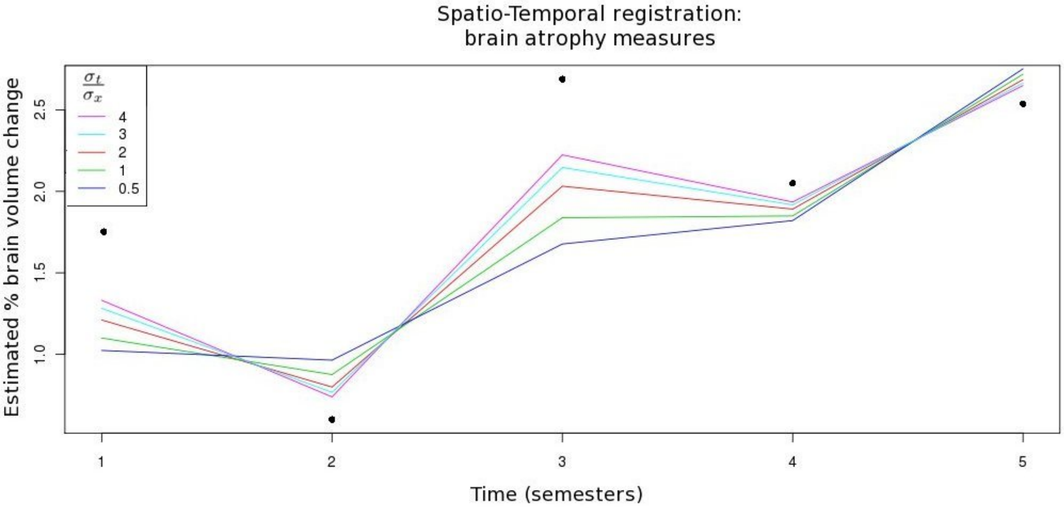

Figure A.1: Flux-derived brain volume change in time for a specific subject without temporal regularization (black dots) and with different trade-off $\frac{\sigma_t}{\sigma_x}$ for the temporal constraint (coloured lines). The amount of the weight on the temporal constraint lead to a more linear

the new estimation of the deformations, and different regularization weights for the trade-off between spatial ad temporal informations were tested: $\frac{\sigma_t}{\sigma_x} = 0.5, 1, 2, 3, 4$.

Figure A.1 illustrates the effects of the temporal regularization on the measurements of the longitudinal brain volume changes. It can be noticed that the increase of the weight on the temporal constraint leads to a more linear (regular in time) estimation of the progression.

A.D Conclusion and Perspectives

We showed that the log-Demons algorithm can be easily extended into a 4D registration framework by introducing at the regularization level a prior term representing a temporal model of the longitudinal trajectory. The presented framework increases the regularity in time of the longitudinal measures, and thus reduces the intra-subject variability. This is an important feature which might for instance increase the power of a longitudinal clinical trial. Due to the limited number of longitudinal observations the preliminary results were obtained through a linear model in time for the SVFs. Even though a linear progression could not track faithfully the real underlying biological process, this first order approximation led to reliable results in the spatio-dimensional registration.

Further studies are needed to define the optimal trade-off between spatial and temporal weights in terms of registration accuracy, stability of the longitudinal measures and increased statistical power.

Appendix B

Locally weighted non-rigid registration

This chapter describes a preliminar work on the introduction of local confidence weights in the log-Demons algorithm, in order to account for missing correspondences in the image registration. Such a method updates the one proposed by [Lamecker and Pennec, 2010], and provided better results when tested in the PhD work of Erin Stretton in Asclepios team[1], for the longitudinal modeling of tumor growth in brain images.

B.A Introduction

Non-rigid registration finds different applications in brain tumor modeling. For instance, if we are interested in analyzing the longitudinal changes in the brain structure or function, non-rigid registration accounts for brain tissue deformation due to tumor growth (mass effect) [Stretton et al., 2011].

From the technical point of view, the registration of longitudinal brain tumor images needs to account for the intensity changes due to the edema and bleedings caused by the tumor growth on the surrounding healthy tissues. This intensity shift is a potential bias for the estimation of the deformation field, and should be explicitly modeled in the registration. If we are interested in modeling the mass effect, we want to exclude the tumor areas in order to not affect the motion detection in the remaining part of the brain. From the registration point of view this requires to specify local confidence weights to model the areas where the correspondence is missing, and thus the estimated deformation is ureliable. In [Stefanescu et al., 2004] it was proposed to impose a diffusive regularization governed by a spatially varying local confidence parameter, where the pathological regions are modeled with low or zero confidence. This method leads however to a highly non-trivial mathematical optimization problem. A more efficient solution was proposed by [Lamecker and Pennec, 2010], where the Symmetric log-Demons was adapted in order to perform differential regularization on *binary masks*. However, the alternate optimization scheme of the log-Demons is broken and the proposed solution is not consistent anymore with the original regularization framework.

We show in this chapter how to derive a log-Demons based weighted regularization consistently with the mathematical formulation of the algorithm, and which preserves the original computational structure.

---

[1] https://sites.google.com/site/erinstrettonweb/

B.B Locally weighted log-Demons registration

We propose here to adapt the log-Demons regularization in order to account for local weights in the estimation of the optimal deformation. Let consider the regularization energy 2.4:

$$E\text{reg}(\mathbf{v}) \quad = \quad \frac{1}{\sigma_x^2}\| \log(\exp(\mathbf{v_x}) \circ \exp(-\mathbf{v}))\|_{L_2}^2 + \frac{1}{\sigma_T}\text{Reg}(\mathbf{v}). \tag{B.1}$$

The weights can be introduced as a probability mask $w(x)$ which multiplies the coupling term. In this way, we require to the optimal $\mathbf{v}$ to be close to the correspondence $\mathbf{v_x}$ in the high confidence areas ($w(x)$ close to 1), while in the areas of low confidence we enforce only the regularity imposed by the term Reg($\mathbf{v}$).

The regularity term Reg($\mathbf{v}$) can be explicitly written as sum of infinite order isotropic differential quadratic forms $Q_k(\mathbf{v}) = \alpha_k \partial_{i_1 \dots i_k} \mathbf{v}_{i_{k+1}} \partial_{i_1 \dots i_k} \mathbf{v}_{i_{k+1}} + \beta_k \partial_{i_1 \dots i_k} \mathbf{v}_{i_{k+1}} \partial_{i_{k+1} i_2 \dots i_k} \mathbf{v}_{i_1}$ [Cachier and Ayache, 2004]. $\partial_{i_1 \dots i_k}$ denotes the composition of spatial derivatives, while $\alpha_k \geq 0$ and $\beta_k \geq -\alpha_k$ are scalar coefficients which ensure the positiveness of the differential quadratic form. We obtain

$$E\text{reg}(\mathbf{v}) \quad = \quad \frac{w}{\sigma_x^2}\| \log(\exp(\mathbf{v_x}) \circ \exp(-\mathbf{v}))\|_{L_2}^2 + \frac{1}{\sigma_T}\int \sum_{k=1}^{\infty} Q^k(\mathbf{v}).$$

In order to preserve the shape of the impulse response [Cachier and Ayache, 2004], we consider the weight σ_T as a parameter of the regularizer which depends on the order k of the quadratic forms

$$E\text{reg}(\mathbf{v}) \quad = \quad \frac{w}{\sigma_x^2}\| \log(\exp(\mathbf{v_x}) \circ \exp(-\mathbf{v}))\|_{L_2}^2 + \int \sum_{k=1}^{\infty} \frac{Q^k(\mathbf{v})}{\sigma_T^{2k}}.$$

By considering the zeroth-order approximation for the BCH formula, and by optimizing with respect to $\mathbf{v}$ we obtain

$$\mathbf{v} + (w-1)\,\mathbf{v} + \sigma_x^2 \sum_{k=1}^{\infty} \frac{(-1)^k}{\sigma_T^{2k}} \left[\alpha_k \Delta^k \mathbf{v} + \beta_k \Delta^{k-1} \nabla\nabla^T \mathbf{v}\right] \quad = \quad w\,\mathbf{v_x}.$$

For sake of simplicity, as shown in [Mansi et al., 2011a] we choose $\alpha_k = \frac{1}{\sigma_x^2 k!}$ and $\beta_k = 0$ in order to constrain the regularization to standard Gaussian filtering. By applying the Fourier transform $\mathcal{F}$, the above equation becomes

$$exp(\frac{\xi^T \xi}{\sigma_T^2})\tilde{\mathbf{v}} + \mathcal{F}(w-1) * \tilde{\mathbf{v}} \quad = \quad \mathcal{F}(w\,\mathbf{v_x}),$$

with $\xi = \mathcal{F}(x)$, and $\tilde{\mathbf{v}} = \mathcal{F}(\mathbf{v})$. We thus have

$$\tilde{\mathbf{v}} + exp(\frac{\xi^T \xi}{\sigma_T^2})\,[\mathcal{F}(w-1) * \tilde{\mathbf{v}}] \quad = \quad \mathcal{F}(w\,\mathbf{v_x}).$$

By assuming the exponential function $exp(\frac{\xi^T\xi}{\sigma_T^2})$ locally constant (i.e. sufficiently smooth with respect to $\mathcal{F}(w-1)$), the equation becomes

$$\tilde{\mathbf{v}} + \left[exp(\frac{\xi^T\xi}{\sigma_T^2})\mathcal{F}(w-1) \right] * \tilde{\mathbf{v}} \quad = \quad \mathcal{F}(w\,\mathbf{v_x}). \tag{B.2}$$

Transforming back to the real domain we obtain

$$\mathbf{v} + G_\sigma * (w-1) \cdot \mathbf{v} \quad = \quad G_\sigma * (w\,\mathbf{v_x}),$$

and thus

$$\mathbf{v} = \frac{G_\sigma * (w\,\mathbf{v_x})}{1 + G_\sigma * (w-1)} \quad = \quad \frac{G_\sigma * (w\,\mathbf{v_x})}{G_\sigma * (w)}$$

B.C Preliminary Results

The proposed weighted regularization was used to register a follow-up brain tumor image of a low-glioma patient to the baseline. The data was kindly provided by Bjöern Menze (Computer Vision Laboratory, ETH Zurich) on behalf of Prof. Marc-André Weber (Department of Diagnostic and Interventional Radiology, Heidelberg University).

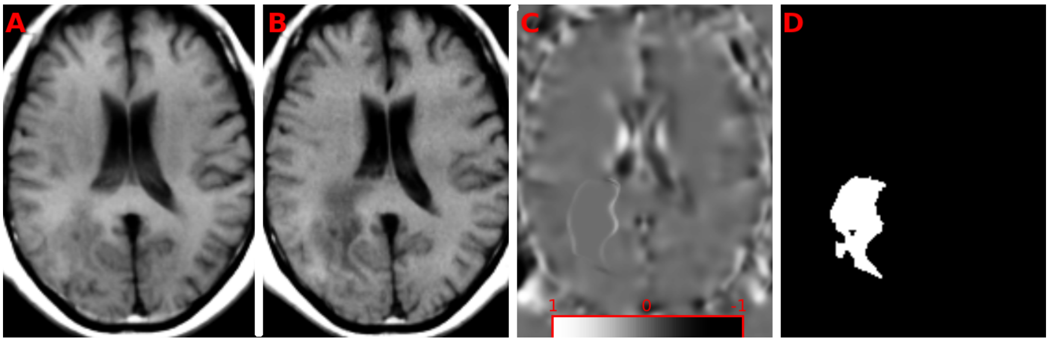

Figure B.1: Mass effect analysis. A,B) Two-years follow-up sequence of T1 MRIs for a low-grade glioma patient , C) divergence scalar map associated to the longitudinal deformation, D) prior mask for the tumor of the follow-up image. We notice that the divergence in the tumor area is null.

In figure B.1 it is shown that the divergence associated to the longitudinal deformation is null inside the tumor mask. By comparison we notice the high divergence areas located in the ventricles, to indicate the swelling due to the tumor growth.

B.D Conclusion and perspectives

We showed that, when adding in the log-Damons *spatially smoothly varying* weights for the local confidence of the registration, the optimal solution is the weighted convolution of the correspondence field. Interestingly the present solution does not alter the classical optimization scheme of the log-Demons, and thus preserves the computational efficiency. The framework found a preliminar application in the registration of follow-up brain tumor images, in which the tumor is masked in order to reliably detect the mass effect. The method can find different applications from the proposed one, for all the cases in which there exist no one-to-one correspondence between pairs of images. Further validation of the method is however still required from both quantitative and qualitative points of view. Finally, the relationship between mask smoothness and regularization strength emerged in equation B.2 is another important aspect that deserves future further investigation.

Appendix C

Enrichment through biomarkers in clinical trials of Alzheimer's drugs in patients with mild cognitive impairment

---

This chapter resumes the journal paper [Lorenzi et al., 2010c] that was written in collaboration with the LENITEM team directed by Dr. Giovanni Frisoni, and that was finalized during the first part of my PhD.

The design of a clinical trial is the first and critical step for reliably testing the effectiveness of treatments. In this work we investigated different enrollment strategies for an hypothetical clinical trial based on the screening through different AD makers.

C.A Introduction

It is widely believed that MCI patients with abnormal brain structure, metabolism, or biochemical marker profile are more likely to develop AD than the parent MCI population. A proposal for new diagnostic criteria has been developed that could allow diagnosis of AD at the MCI stage based on atrophy of medial temporal lobe structures (among which the hippocampus) on structural magnetic resonance imaging (MRI), hypometabolism in the temporoparietal cortex on 18F-FDG PET, low Aβ42 or high tau or phospho-tau in the CSF, and positivity on amyloid imaging with tracers such as 11C-PIB [Dubois et al., 2007] . A corollary of this is that AD markers might be employed in clinical trials of MCI patients to screen out non-AD MCI cases and select a population of MCI enriched with truly AD cases to be randomized.

Of course, the ideal marker is one with 100% sensitivity and specificity, which would support screening out of all non AD and screening in all AD cases. However, this is hardly a realistic scenario. In a clinical trial scenario, a good marker will be one which maximises the proportion of AD cases which are screened positive and included, i.e. the true positive rate, and minimizes the proportion of AD cases which are screened negative and excluded, i.e. the false negative rate.

C.B Patient Enrollment through Screening with the AD Biomarkers

405 MCI patients (143 converters and 262 non converters to AD within 2 years) of ADNI were used. Markers for enrichment were hippocampal atrophy on MR, temporoparietal hypometabolism on FDG PET, CSF biomarkers (Aβ42, tau, and phospho-tau), and cortical amyloid deposition (11C-PIB PET). Two separate enrichment strategy were tested aimed respectively to A) maximize the proportion of MCI converters screened-in, and B) minimize the proportion of MCI converters screened-out. Figure C.1 shows that the distribution of markers was roughly bell-shaped for all markers in the three groups of healthy elderly controls, MCI converters, and MCI non converters.

Figure C.2 shows that with enrichment strategy A, increasingly restrictive thresholds (from none to the 99th percentile of the distribution of healthy elderly controls) generally lead to select a monotonously increasingly enriched proportion of future converters among those screened in, except in the case of CSF markers where the correspondence of the distribution curves of MCI converters and non converters led to a monotonous increase. The highest proportion of future converters was achieved by hippocampal volume thresholded at the first percentile of the healthy elders distribution, and by 11C-PIB PET thresholded at the 95th percentile, increasing from 36% with no threshold to 59 and 60%, respectively. However, this enrichment was obtained at the expense of a marked increase of screened out rate, up to 77% and 84% of those MCI enrolled.

The Figure shows also the thresholds found with enrichment strategy B. The lowest proportion of screened out converters was achieved by ADAS-cog (7.5%) and 11C-PIB PET (9%) at the 58th and 85th percentile respectively. For CSF biomarkers, the proportion of screened-out MCI converters was monotonously decreasing with decreasing marker values, thus preventing to identify an optimal threshold.

C.C Conclusions

Screening through imaging and biological markers can lead to a significant enrichment of groups of MCI patients enrolled in clinical trials of AD drugs with “true AD cases”, i.e. patients who will convert in the following months. A key point is the role of the screening thresholds: in a hypothetical clinical trial, the balance between enrichment of screened-in and loss of screened-out patients should be viewed in the light of 1) the gain of power and the relative decreased costs brought about by enrichment, and 2) the increased costs brought about by the exclusion of screened-out patients.

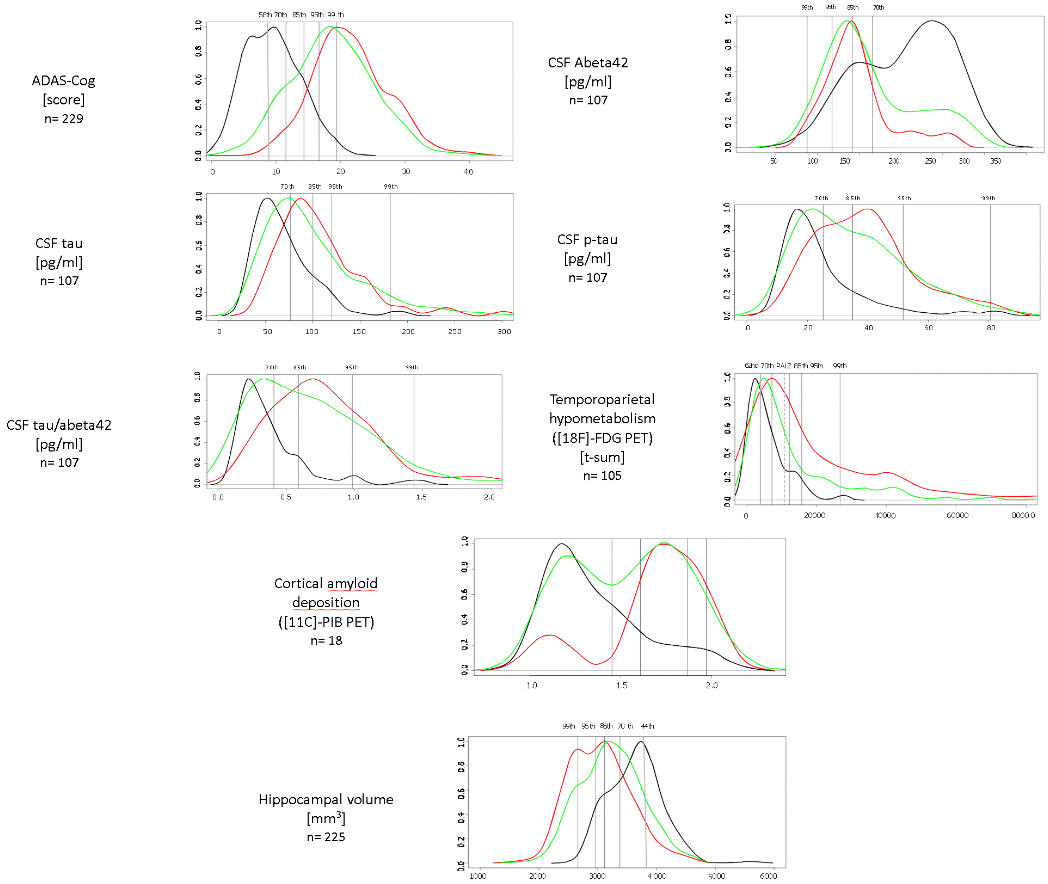

Figure C.1: MCI non converters and MCI converters among screened-in and screened-out at increasingly restrictive thresholds of Alzheimer's disease markers. Red, green, and black lines denote the distributions of MCI converters, MCI non converters, and healthy elderly controls. Thresholds refer to the distribution of the marker values in healthy elders.

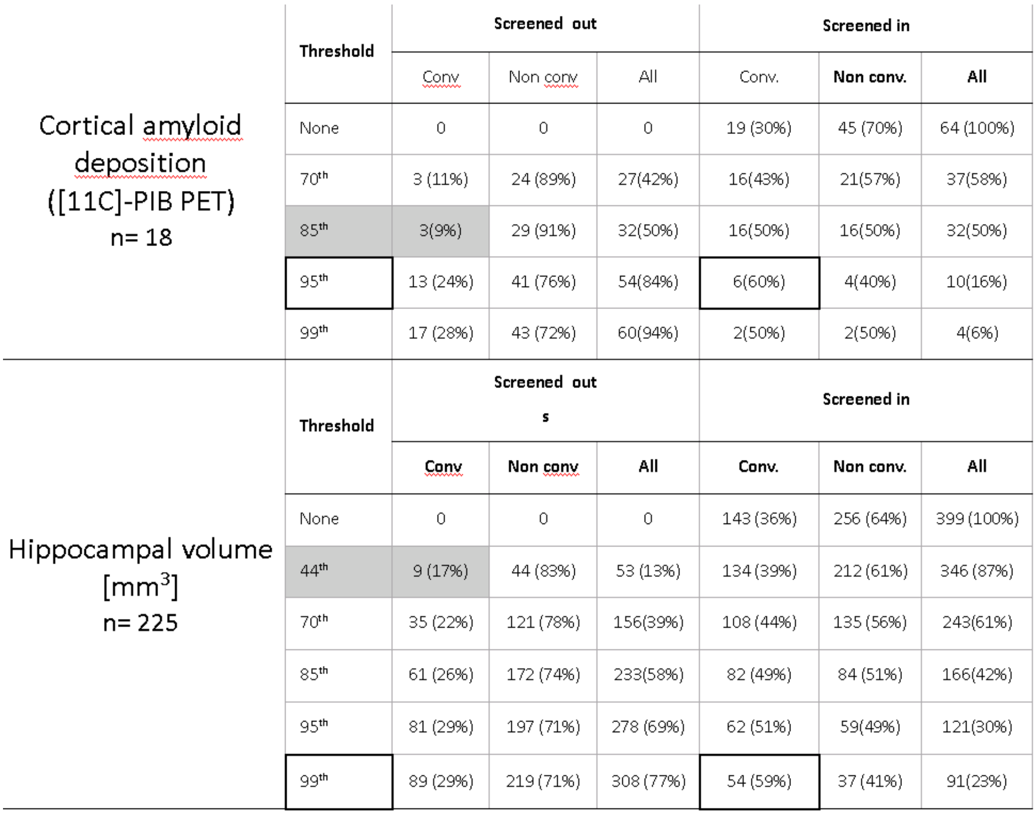

	Threshold	Screened out			Screened in		
		Conv	Non conv	All	Conv.	Non conv.	All
Cortical amyloid deposition ([11C]-PIB PET) n= 18	None	0	0	0	19 (30%)	45 (70%)	64 (100%)
	70th	3 (11%)	24 (89%)	27(42%)	16(43%)	21(57%)	37(58%)
	85th	3(9%)	29 (91%)	32(50%)	16(50%)	16(50%)	32(50%)
	95th	13 (24%)	41 (76%)	54(84%)	6(60%)	4(40%)	10(16%)
	99th	17 (28%)	43 (72%)	60(94%)	2(50%)	2(50%)	4(6%)

	Threshold	Screened out s			Screened in		
		Conv	Non conv	All	Conv.	Non conv.	All
Hippocampal volume [mm^3] n= 225	None	0	0	0	143 (36%)	256 (64%)	399 (100%)
	44th	9 (17%)	44 (83%)	53 (13%)	134 (39%)	212 (61%)	346 (87%)
	70th	35 (22%)	121 (78%)	156(39%)	108 (44%)	135 (56%)	243(61%)
	85th	61 (26%)	172 (74%)	233(58%)	82 (49%)	84 (51%)	166(42%)
	95th	81 (29%)	197 (71%)	278 (69%)	62 (51%)	59(49%)	121(30%)
	99th	89 (29%)	219 (71%)	308 (77%)	54 (59%)	37 (41%)	91(23%)

Figure C.2: MCI non converters and MCI converters among screened-in and screened-out at increasingly restrictive thresholds of Alzheimer's disease markers. Thresholds refer to the distribution of the marker values in healthy elders. The percentages of all screened-out and all screened-in refer to the whole group of MCI patients, while the percentages of converters and non converters refer to screened-in and screened-out. Cells with thick margins denote the threshold associated with the highest percentage of converters among screened-in (enrichment strategy A), while grey cells denote those associated with the lowest percentage of converters among screened-out (enrichment strategy B).

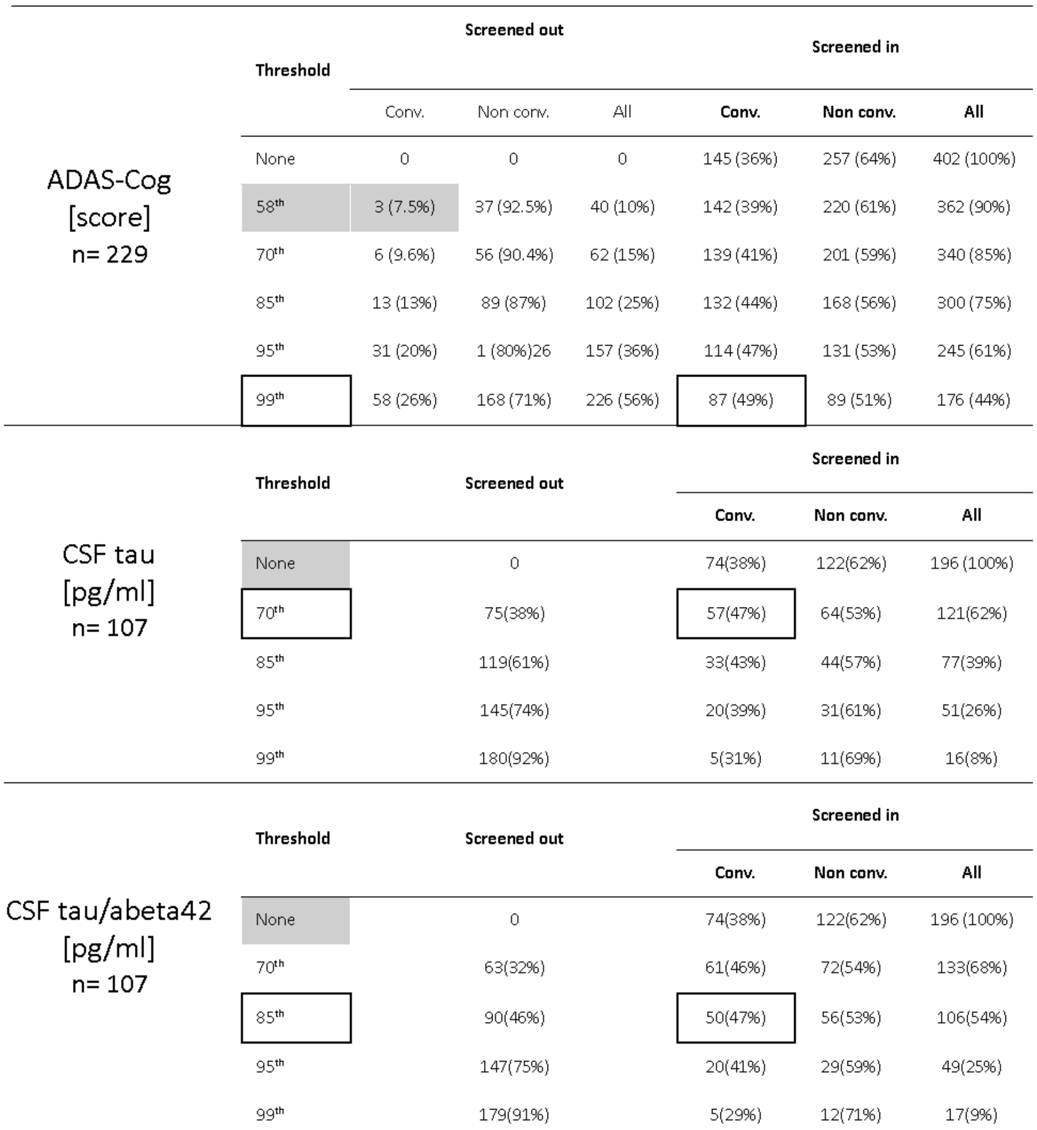

	Threshold	Screened out			Screened in		
		Conv.	Non conv.	All	**Conv.**	**Non conv.**	**All**
ADAS-Cog [score] n= 229	None	0	0	0	145 (36%)	257 (64%)	402 (100%)
	58th	3 (7.5%)	37 (92.5%)	40 (10%)	142 (39%)	220 (61%)	362 (90%)
	70th	6 (9.6%)	56 (90.4%)	62 (15%)	139 (41%)	201 (59%)	340 (85%)
	85th	13 (13%)	89 (87%)	102 (25%)	132 (44%)	168 (56%)	300 (75%)
	95th	31 (20%)	1 (80%)26	157 (36%)	114 (47%)	131 (53%)	245 (61%)
	99th	58 (26%)	168 (71%)	226 (56%)	87 (49%)	89 (51%)	176 (44%)

	Threshold	Screened out	Screened in		
			Conv.	**Non conv.**	**All**
CSF tau [pg/ml] n= 107	None	0	74(38%)	122(62%)	196 (100%)
	70th	75(38%)	57(47%)	64(53%)	121(62%)
	85th	119(61%)	33(43%)	44(57%)	77(39%)
	95th	145(74%)	20(39%)	31(61%)	51(26%)
	99th	180(92%)	5(31%)	11(69%)	16(8%)

	Threshold	Screened out	Screened in		
			Conv.	**Non conv.**	**All**
CSF tau/abeta42 [pg/ml] n= 107	None	0	74(38%)	122(62%)	196 (100%)
	70th	63(32%)	61(46%)	72(54%)	133(68%)
	85th	90(46%)	50(47%)	56(53%)	106(54%)
	95th	147(75%)	20(41%)	29(59%)	49(25%)
	99th	179(91%)	5(29%)	12(71%)	17(9%)

	Threshold	Screened out	Screened in		
			Conv.	Non conv.	All
CSF Abeta42 [pg/ml] n= 107	None	0	74(38%)	122(62%)	196 (100%)
	192 pg/ml	51 (26%)	65 (45%)	80 (55%)	145 (74%)
	70th	69(35%)	59(47%)	68(53%)	127(65%)
	85th	108(55%)	38(43%)	50(57%)	88(45%)
	95th	159(81%)	16(43%)	21(57%)	37(19%)

	Threshold	Screened out	Screened in		
			Conv.	Non conv.	All
CSF p-tau [pg/ml] n= 107	None	0	74(38%)	122(62%)	196 (100%)
	70th	72(37%)	56(45%)	68(55%)	124(63%)
	85th	108(55%)	41(47%)	47(53%)	88(45%)
	95th	163(83%)	12(36%)	21(64%)	33(17%)
	99th	191(97%)	2(40%)	3(60%)	5(3%)

	Threshold	Screened out			Screened in		
		Conv.	Non Conv.	All	Conv.	Non conv.	All
Temporoparietal hypometabolism ([18F]-FDG PET) [t-sum] n= 105	None	0	0	0	61 (29%)	146 (71%)	207 (100%)
	11,090	32 (24%)	100 (76%)	132(64%)	29(38%)	46(61%)	75(36%)
	62nd	13 (16%)	67 (84%)	80 (39%)	48 (38%)	79 (62%)	127 (61%)
	70th	19 (19%)	81 (81%)	100(48%)	42(39%)	65(61%)	107(52%)
	85th	32 (23%)	108 (77%)	140 (68%)	29(43%)	38(57%)	67(32%)
	95th	39 (25%)	115 (75%)	154 (74%)	22(41%)	31(59%)	53(26%)
	99th	46 (74%)	133 (26%)	179(86%)	15(53%)	13(47%)	28(14%)

Appendix D

Modelling power for change in hippocampal atrophy with differential rates of subject removal

We have seen in the previous chapter the critical importance of the enrollment strategy for the outcome of a clinical trial. This chapter resumes the report on the statistical analysis performed within the PHARMA-COG clinical project, for the study of the optimal enrollment strategy for a longitudinal trial on MCI, based on the distribution of the Aβ42 marker among the subjects at the baseline. The statistical analysis was supervised by Dr. David R. Willé (GlaxoSmithKline).

D.A The PHARMA-COG european project

The PHARMA-COG consortium[1] consists of 30 public (Univeristies, Research Centres, Hospitals) and private partners (SMEs and EFPIA members), as well as a patients' Association Alzheimer Europe, coming from 10 different EU Members states.

Workpackage 5 of PharmaCog (Identification of biomarkers sensitive to disease progression: Clinical Studies - European ADNI) is about the development of markers to track the progression of the disease in humans that are homologous to those used in animal models. WP5 uses as core markers those harmonized in the context of the North American ADNI and expands them with specific structural, functional, microstructural, molecular, central, and peripheral markers.

The study plans to enroll 150 MCI patients and to compare the evolution of a set of AD markers between those MCI with low levels ($<$192 pg/ml) of CSF Amyloid β42 (Aβ42+) and those with high levels of CSF Amyloid β42 (Aβ42-) for a 3-year follow-up. Conversion to AD determines the exclusion of the subject from the trial, and thus contributes to the loss of sample size. The rationale of this design is based on the amyloid cascade hypothesis, suggesting that brain amyloidosis is the initiating event in AD, and increase of brain amyloid deposits is reflected by a reduction of Aβ42 levels in the CSF. Most current clinical trials are on anti-amyloid drugs and some of these target MCI patients who are selected based on brain amyloidosis, i.e.

---

[1] http://www.alzheimer-europe.org/Research/PharmaCog

on CSF Aβ42 levels. In a clinical trial-like population (ADNI1-like), the proportion of those with brain amyloidosis based on CSF analysis is about 2/3.

D.B Calibrating the Enrollment Ratio Between Aβ42+ and Aβ42-

The study is powered on the power to detect a difference in the rate of hippocampal atrophy between CSF Aβ42+ and CSF Aβ42- subjects over the study period. Since changes in hyppocampal volume are calculated at the end of the study at year three, and the expected rates of conversion between the two Aβ42 groups differ, we ask, for this primary endpoint:

- What is the power of the study at the three years, for given total sample and looked for effect size?
- What is the optimal ratio of Aβ42+ and Aβ42- at the start of the trial to maximise this power? Moreover, what is the cost in terms of loss of power if another starting ratio is selected?

The answers to these questions depended on the effect of the Aβ42 ratio on the total population attrition. Since Aβ42+ cases are more likely to convert to AD, this increases as the ratio of Aβ42+ to Aβ42- at recruitment also increases.

Our analysis is based upon a collection of MCI data from the ADNI dataset. The population analyzed was composed by 195 MCI subjects followed during a three years follow-up study with longitudinal clinical and MR assessment. The mean age of the group was of 67.6 years with a standard deviation of 15.4. In the group, 146 subjects (74.8% of the population) were Aβ42+.

At subject-by-subject level, a strong linear trend was observed for the hippocampal atrophy over time which formed the basis of our model (Figure D.1).

The corresponding rates were compared between the two Aβ42 loading groups, and used as the basis of a t-test. This, mathematically equivalent to a full random coefficient mixed model for suitable choices of error covariance structure, provided a simpler and more tractable framework for power calculation. Instantaneous rates of MCI to AD conversion (0.066 and 0.187 years for respectively Aβ42- and +) where then estimated from the observed three year conversion probabilities (0.43 and 0.18), and used to model the decline in each study population combined with an additional 10% attrition loss (rate of 0.105) due to other causes.

The optimal starting population was shown to be enriched for Aβ42+ by a ratio of 1.19:1. Every moderate deviation from this only had a minor effect on overall power. Starting from initial starting ratio of 2:1 only resulted in a loss of power equivalent to running a study with 141 instead of 150 subjects.

Figure D.2 summarizes the predicted overall power to be expected at year three taking into account not only the change in the relative sizes of the Aβ42 population over the study period, but also their fall in absolute value.

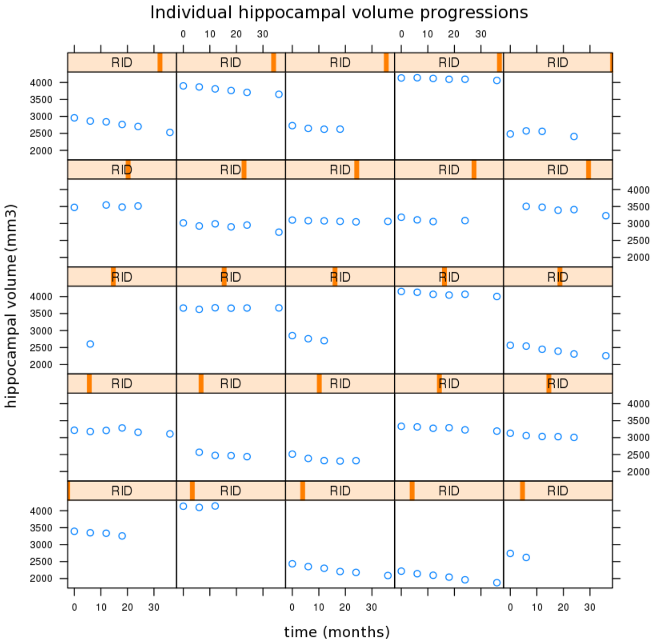

Figure D.1: Hippocampal volume progression for a sample of MCI subjects of the ADNI dataset.

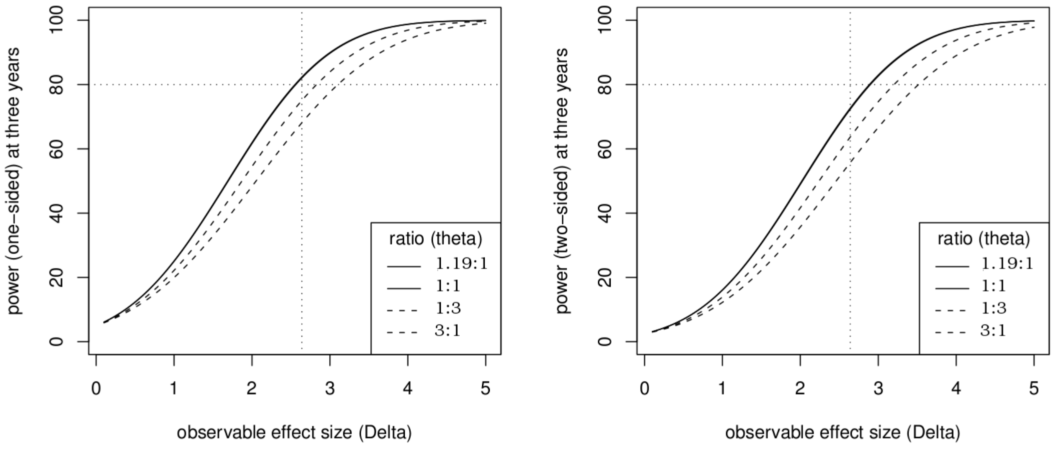

Figure D.2: Power analysis based on the initial ratio of Aβ42+ over Aβ42- for one and two sided hypothesis (left and right pictures respectively).

This shows that the study is able to pick up reference change of 2.64 (that observed in the ADNI study) with an 80% power with a one-sided tests but falls short of this objective if the more conventional two-sided approach is used. This is interesting because whereas it is not statistically indicated (the always decreasing volumes making the one-sided framework here a valid statistical construct) this will not be the case for most other biomarkers or combinations of biomarkers.

D.C Conclusions

Power analysis shows that the change of power is minimal between ratios 1:1 and 2:1 (CSF Aβ42+ to CSF Aβ42-). The ADNI data indicate that patients who are CSF Aβ42+ are 2/3 of the total (ratio 2:1). Although there is no indication in the literature what the proportion of Aβ42+ might be, it is reasonable to assume that it lies between 1/2 and 2/3, corresponding to ratios between 1:1 and 2:1. Interestingly, when removals in addition to MCI to AD conversion are taken into account, the study is powered only when using a one-sided test, which exploits the fact that the brain atrophy always increases.

Bibliography

[Alexander et al., 2001] Alexander, D., Pierpaoli, C., Basser, P., and Gee, J. (2001). Spatial transformations of diffusion tensor magnetic resonance images. *IEEE Transactions on Medical Imaging*, 20(11). (Cited on page 43.)

[Aljabar et al., 2008] Aljabar, P., Bhatia, K., Murgasova, M., Hajnal, J., Boardman, J., Srinivasan, L., Rutherford, M., Dyet, L., Edwards, A., and Rueckert, D. (2008). Assessment of brain growth in early childhood using deformation-based morphometry. *NeuroImage*, 39(1):348–358. (Cited on page 7.)

[Arsigny et al., 2006] Arsigny, V., Commowick, O., Pennec, X., and Ayache, N. (2006). A Log-Euclidean framework for statistics on diffeomorphisms. In *Medical Image Computing and Computer-Assisted Intervention - MICCAI*, volume 9, pages 924–931. (Cited on pages 8, 20, 22, 62, 70 and 94.)

[Ashburner, 2007a] Ashburner, J. (2007a). A fast diffeomorphic image registration algorithm. *NeuroImage*, 38(1):95–113. (Cited on page 20.)

[Ashburner, 2007b] Ashburner, J. (2007b). A fast diffeomorphic image registration algorithm. *NeuroImage*, 38(1):95 – 113. (Cited on page 70.)

[Ashburner and Friston, 2000] Ashburner, J. and Friston, K. (2000). Voxel-based morphometry – the methods. *NeuroImage*, 11:805–821. (Cited on pages 5 and 20.)

[Ashburner and Friston, 2005] Ashburner, J. and Friston, K. (2005). Unified segmentation. *NeuroImage*, 26:839–851. (Cited on page 5.)

[Ashburner et al., 1998] Ashburner, J., Hutton, C., Frackowiak, R., Johnsrude, I., Price, C., and Friston, K. (1998). Identifying global anatomical differences: Deformation-based morphometry. *Human Brain Mapping*, 6(5):348–357. (Cited on page 4.)

[Atlaswerks, 2007] Atlaswerks (2007). AtlasWerks: A set of high-performance tools for diffeomorphic 3D image registration and atlas building. Scientific Computing and Imaging Institute (SCI). (Cited on page 72.)

[Avants et al., 2007] Avants, B., Anderson, C., Grossman, M., and Gee, J. (2007). Spatiotemporal normalization for longitudinal analysis of gray matter atrophy in frontotemporal dementia. In *Proceedings of Medical Image Computing and Computer Assisted Intervention (MICCAI)*, volume 10, pages 303–310. (Cited on pages 20, 92 and 139.)

[Avants et al., 2008] Avants, B. B., Epstein, C. L., Grossman, M., and Gee, J. C. (2008). Symmetric diffeomorphic image registration with cross-correlation: evaluating automated labeling of elderly and neurodegenerative brain. *Medical Image Analysis*, 12(1):26–41. (Cited on pages 19 and 20.)

[Bajcsy et al., 1993] Bajcsy, R., Gee, J. C., and Reivich, M. (1993). Elastically deforming 3d atlas to match anatomical brain images. *Journal of Computer Assisted Tomography*, 17(2):225–36. (Cited on page 19.)

[Barnes, 2011] Barnes, C. (2011). Secrets of aging: What does a normally aging brain look like? *Biol Rep.*, 3(22). (Cited on page 122.)

[Barnes et al., 2007] Barnes, J., Boyes, R. G., Lewis, E. B., Schott, J. M., Frost, C., Scahill, R. I., and Fox, N. C. (2007). Automatic calculation of hippocampal atrophy rates using a hippocampal template and the boundary shift integral. *Neurobiol Aging*, 28(11):1657–63. (Cited on page 7.)

[Benjamini and Hochberg, 1995] Benjamini, Y. and Hochberg, Y. (1995). Controlling the False Discovery Rate: A Practical and Powerful Approach to Multiple Testing. *Journal of the Royal Statistical Society. Series B (Methodological)*, 57(1):289–300. (Cited on page 6.)

[Bossa et al., 2007] Bossa, M., Hernandez, M., and Olmos, S. (2007). Contributions to 3D diffeomorphic atlas estimation: Application to brain images. In *Medical Image Computing and Computer-Assisted Intervention - MICCAI*, volume 10, pages 667–674. (Cited on pages 20, 23, 50 and 70.)

[Bossa et al., 2010] Bossa, M., Zacur, E., and Olmos, S. (2010). On changing coordinate systems for longitudinal tensor-based morphometry. *Spatio Temporal Image Analysis Workshop (STIA), 2010*. (Cited on pages 44 and 61.)

[Boyes et al., 2006] Boyes, Rueckert, Aljabar, et al. (2006). Cerebral atrophy measurements using Jacobian integration: Comparison with the boundary shift integral. *NeuroImage*, 32. (Cited on pages 7 and 21.)

[Brookmeyer et al., 2007] Brookmeyer, R., Johnson, E., Ziegler-Graham, K., and Arrighi, H. (2007). Forecasting the global burden of Alzheimer's disease. *Alzheimers Dement*, 3(3):186–191. (Cited on page 1.)

[Cachier, 2002] Cachier, P. (2002). Recalage non rigide d'images madicales volumiques, contributions aux approches imconiques et geometriques. *PhD thesis*. (Cited on page 91.)

[Cachier and Ayache, 2004] Cachier, P. and Ayache, N. (2004). Isotropic energies, filters and splines for vectorial regularization. *J. of Math. Imaging and Vision*, 20:251–265. (Cited on pages 72 and 144.)

[Cachier et al., 2003] Cachier, P., Bardinet, E., Dormont, D., Pennec, X., and Ayache, N. (2003). Iconic feature based nonrigid registration: The pasha algorithm. *Computer Vision and Image Understanding*, 89(2-3):272–298. Special Issue on Nonrigid Registration. (Cited on pages 19, 24 and 94.)

[Cachier and Pennec, 2000] Cachier, P. and Pennec, X. (2000). Non-rigid registration by gradient descent on a gaussian-windowed similarity measure using convolutions. In *Proceedings of the IEEE Workshop on Mathematical Methods in Biomedical Image Analysis*, MMBIA '00, pages 182–, Washington, DC, USA. IEEE Computer Society. (Cited on page 19.)

[Camara et al., 2008] Camara, O., Schnabel, J., Ridgway, G., et al. (2008). Accuracy assessment of global and local atrophy measurement techniques with realistic simulated longitudinal Alzheimer's disease images. *NeuroImage*, 42. (Cited on pages 7 and 21.)

[Carmichael et al., 2005] Carmichael, O. T., Aizenstein, H. A., Davis, S. W., Becker, J. T., Thompson, P. M., Meltzer, C. C., and Liu, Y. (2005). Atlas-based hippocampus segmentation in Alzheimer's disease and mild cognitive impairment. *Neuroimage*, 27(4):979–990. (Cited on page 6.)

[Cartan and Schouten, 1926] Cartan, E. and Schouten, J. (1926). On the geometry of the group-manifold of simple and semi-simple groups. *Proc. Akad. Wekensch, Amsterdam*, 29:803–815. (Cited on page 65.)

[Chetelat et al., 2005] Chetelat, G., Landeau, B., Eustache, F., Mezenge, F., Viader, F., de la Sayette, V., Desgranges, B., and Baron, J.-C. (2005). Using voxel-based morphometry to map the structural changes associated with rapid conversion in MCI: a longitudinal MRI study. *Neuroimage*, 27(4):934–46. (Cited on page 6.)

[Chincarini et al., 2011] Chincarini, A., Bosco, P., Calvini, P., et al. (2011). Local MRI analysis approach in the diagnosis of early and prodromal Alzheimer's disease. *NeuroImage*, 58(2):469–480. (Cited on page 128.)

[Chung et al., 2001] Chung, M., Worsley, K., Paus, T., et al. (2001). A unified statistical approach to deformation-based morphometry. *NeuroImage*. (Cited on pages 5, 7, 21, 44 and 103.)

[Chupin et al., 2009a] Chupin, M., Gérardin, E., Cuingnet, R., Boutet, C., Lemieux, L., Lehéricy, S., Benali, H., Garnero, L., Colliot, O., and Alzheimer's Disease Neuroimaging Initiative (2009a). Fully automatic hippocampus segmentation and classification in Alzheimer's disease and mild cognitive impairment applied on data from ADNI. *Hippocampus*, 19(6):579–587. (Cited on page 128.)

[Chupin et al., 2009b] Chupin, M., Hammers, A., Liu, R. S. N., Colliot, O., Burdett, J., Bardinet, E., Duncan, J. S., Garnero, L., and Lemieux, L. (2009b). Automatic segmentation of the hippocampus and the amygdala driven by hybrid constraints: Method and validation. *NeuroImage*, 46(3):749–761. (Cited on page 6.)

[Collins et al., 1995] Collins, L. D., Holmes, C. J., Peters, T. M., and Evans, A. C. (1995). Automatic 3-D model-based neuroanatomical segmentation. *Human Brain Mapping*, 3(3):190–208. (Cited on page 19.)

[Crum et al., 2001] Crum, W. R., Scahill, R. I., and Fox, N. C. (2001). Automated hippocampal segmentation by regional fluid registration of serial MRI: validation and application in Alzheimer's disease. *Neuroimage*, 13(5):847–855. (Cited on page 6.)

[Cuingnet et al., 2011] Cuingnet, R., Gerardin, E., Tessieras, J., Auzias, G., Lehèricy, S., Habert, M., Chupin, M., Benali, H., and Colliot, O. (2011). Automatic classification of patients with Alzheimer's disease from structural MRI: a comparison of ten methods using the ADNI database. *NeuroImage*, 56(2):766–781. (Cited on page 128.)

[Davatzikos et al., 2009] Davatzikos, C., Xu, F., An, Y., Fan, Y., and Resnik, S. (2009). Longitudinal progression of Alzheimer's-like patterns of atrophy in normal older adults: the SPARE-AD index. *Brain*, 132(8):2026–2035. (Cited on pages 123 and 129.)

[Daviglus et al., 2010] Daviglus, M., Bell, C., Berrettini, W., et al. (2010). National institutes of health state-of-the-science conference statement: Preventing Alzheimer disease and cognitive decline. *Ann Intern Med*, 153(3):176–181. (Cited on page 1.)

[Davis et al., 2007] Davis, B., Fletcher, P., Bullit, E., and Joshi, S. (2007). Population shape regression from random design data. *ICCV*, 4:375–405. (Cited on pages 20 and 139.)

[DeCarli et al., 2007] DeCarli, C., Frisoni, G., Clark, C., et al. (2007). Qualitative estimates of medial temporal atrophy as a predictor of progression from mild cognitive impairment to dementia. *Arch Neurol*, 64(1):108–115. (Cited on page 3.)

[Demokis, 2007] Demokis, G. (2007). Disability in Alzheimer's disease: causes, consequences, and economic considerations. *J Health Hum Serv Adm*, 30(3):292–305. (Cited on page 1.)

[do Carmo, 1992] do Carmo, M. (1992). *Riemannian Geometry*. Mathematics. Birkhäuser, Boston, Basel, Berlin. (Cited on page 62.)

[Dong and Boyer, 1995] Dong, L. and Boyer, A. L. (1995). An image correlation procedure for digitally reconstructed radiographs and electronic portal images. *International Journal of Radiation Oncology*Biology*Physics*, 33(5):1053 – 1060. (Cited on page 19.)

[Dubois et al., 2007] Dubois, B., Feldman, H., Jacova, C., et al. (2007). Research criteria for the diagnosis of Alzheimer's disease: revising the NINCDS-ADRDA criteria. *Lancet Neurol*, 6:734–746. (Cited on pages 3, 112 and 147.)

[Durrleman et al., 2011] Durrleman, S., Fillard, P., Pennec, X., Trouvé, A., and Ayache, N. (2011). Registration, atlas estimation and variability analysis of white matter fiber bundles modeled as currents. *NeuroImage*, 55(3):1073–1090. (Cited on page 61.)

[Durrleman et al., 2012] Durrleman, S., Pennec, X., Trouvé, A., Ayache, N., and Braga, J. (2012). Comparison of the endocranial ontogenies between chimpanzees and bonobos via temporal regression and spatiotemporal registration. *Journal of Human Evolution*, 62(1):74 – 88. (Cited on page 20.)

[Durrleman et al., 2009] Durrleman, S., Pennec, X., Trouvé, A., Gerig, G., and Ayache, N. (2009). Spatiotemporal atlas estimation for developmental delay detection in longitudinal datasets. In *Medical Image Computing and Computer-Assisted Intervention - MICCAI*, volume 12, pages 297–304. (Cited on pages 61 and 139.)

[Fischl et al., 2002] Fischl, B., Salat, D. H., Busa, E., Albert, M., Dieterich, M., Haselgrove, C., van der Kouwe, A., Killiany, R., Kennedy, D., Klaveness, S., Montillo, A., Makris, N., Rosen, B., and Dale, A. M. (2002). Whole brain segmentation: automated labeling of neuroanatomical structures in the human brain. *Neuron*, 33(3):341–355. (Cited on page 6.)

[Fjell and Walhovd, 2012] Fjell, A. and Walhovd, K. (2012). Neuroimaging results impose new views on Alzheimer's disease-the role of amyloid revised. *Mol Neurobiol*, 45(1):153–172. (Cited on page 2.)

[Fjell et al., 2010] Fjell, A., Walhovd, K., Notestine, C., and et al. (2010). Brain atrophy in healthy aging is related to csf levels of Ab1-42. *Cereb. Cortex*, 20-9. (Cited on pages 98 and 126.)

[Fox et al., 2000] Fox, N., Cousens, S., Scahill, R., Harvey, R., and Rossor, M. (2000). Using serial registered brain magnetic resonance imaging to measure disease progression in Alzheimer disease: power calculations and estimates of sample size to detect treatment effects. *Arch Neurol*, 57(3):339–344. (Cited on pages 3 and 33.)

[Fox et al., 2001] Fox, N., Crum, W., Schaill, R., Stevens, J., Janssen, J., and Rossnor, M. (2001). Imaging of onset and progression of alzheimer's disease with voxel compression mapping of serial magnetic resonance images. *Lancet*, 358:201–205. (Cited on pages 5, 20, 102 and 112.)

[Fox et al., 2012] Fox, N., Ridgway, G., and Schott, J. (2012). Algorithms, atrophy and Alzheimer's disease: Cautionary tales for clinical trials. *NeuroImage*, 57(1):15–18. (Cited on pages 7 and 112.)

[Franke et al., 2010] Franke, K., Ziegler, G., Klöppel, S., and Gaser, C. (2010). Estimating the age of healthy subjects from T1-weighted MRI scans using kernel methods: Exploring the influence of various parameters. *NeuroImage*, 50(3):883–892. (Cited on pages 123 and 129.)

[FreeBorough and Fox, 1997] FreeBorough, P. and Fox, N. (1997). The boundary shift integral: An accurate and robust measure of cerebral volume changes from registered repeat mri. *IEEE Transaction on Medical Imaging*, 16(5). (Cited on pages 6, 7, 21, 22, 25, 102 and 112.)

[Frisoni et al., 2010] Frisoni, G., Fox, N., Jr, C. J., Scheltens, P., and Thompson, P. (2010). The clinical use of structural MRI in alzheimer disease. *Nat Rev Neurol*, 6:67–77. (Cited on pages 3, 92, 116 and 122.)

[Frisoni et al., 2009] Frisoni, G. B., Lorenzi, M., Caroli, A., Kemppainen, N., Nagren, K., and Rinne, J. O. (2009). In vivo mapping of amyloid toxicity in alzheimer disease. *Neurology*, 72(17):1504–11. (Cited on page 5.)

[Gallot et al., 1993] Gallot, S., Hulin, D., and Lafontaine, J. (1993). *Riemannian Geometry*. Springer Verlag, 2nd edition edition. (Cited on page 62.)

[Galluzzi et al., 2009] Galluzzi, S., Testa, C., Boccardi, M., Bresciani, L., Benussi, L., Ghidoni, R., Beltramello, A., Bonetti, M., Bono, G., amd G. Magnani amd G. Minonzio, A. F., Piovan, E., Binetti, G., and Frisoni., G. (2009). The Italian Brain Normative Archive of structural MR scans: norms for medial temporal atrophy and white matter lesions. *Aging Clin Exp Res.*, 21(4-5):264–5. (Cited on page 74.)

[Gaser et al., 2001] Gaser, C., Nenadic, I., Buchsbaum, B. R., Hazlett, E. A., and Buchsbaum, M. S. (2001). Deformation-based morphometry and its relation to conventional volumetry of brain lateral ventricles in mri. *NeuroImage*, pages 1140–1145. (Cited on pages 5 and 7.)

[Guimond et al., 2000] Guimond, A., Meunier, J., and Thirion., J. (2000). Average brain models: A convergence study. *Computer Vision and Image Understanding*, 77-2. (Cited on page 96.)

[Hansen et al., 2009] Hansen, M. S., Larsen, R., and Christensen, N. V. (2009). Curl-gradient image warping - introducing deformation potentials for medical image registration using Helmholtz decomposition. In *VISAPP 2009*, volume 1, pages 179–185. (Cited on page 102.)

[Helgason, 1978] Helgason, S. (1978). *Differential Geometry, Lie groups, and Symmetric Spaces*. Academic Press. (Cited on pages 62 and 67.)

[Hermosillo and Faugeras, 2004] Hermosillo, G. and Faugeras, O. D. (2004). Well-posedness of two nonrigid multimodal image registration methods. *SIAM Journal of Applied Mathematics*, 64(5):1550–1587. (Cited on page 19.)

[Hernandez et al., 2009] Hernandez, M., Bossa, M., and Olmos, S. (2009). Registration of anatomical images using paths of diffeomorphisms parameterized with stationary vector field flows. *International Journal of Computer Vision*, 85:291–306. (Cited on page 70.)

[Holden, 2008] Holden, M. (2008). A review of geometric transformations for nonrigid body registration. *IEEE Trans Med Imaging*, 27(1):111–128. (Cited on page 4.)

[Iglesias et al., 2011] Iglesias, J., C.Liu, Thompson, P., and Tu, Z. (2011). Robust brain extraction across datasets and comparison with publicly available methods. *IEEE Trans. Med. Imaging*, 30(9):1617–1634. (Cited on pages 6 and 115.)

[Jack et al., 2010a] Jack, C., Knopman, D., Jagust, W., et al. (2010a). Hypothetical model of dynamic biomarkers of the Alzheimer's pathological cascade . *Lancet Neurol*, 9(1):119–128. (Cited on pages 2, 3 and 134.)

[Jack et al., 2010b] Jack, C., Knopman, D., Jagust, W., Shaw, L., Aisen, P., Weiner, M., Petersen, R., and Trojanowski, J. (2010b). Hypothetical model of dynamic biomarkers of the Alzheimer's pathological cascade. *Lancet Neurol*, 9(1):119–128. (Cited on pages 111 and 123.)

[Jack et al., 2004] Jack, C., Shiung, M., Gunter, J., et al. (2004). Comparison of different MRI brain atrophy rate measures with clinical disease progression in AD. *Neurology*, 62(4):591–600. (Cited on page 3.)

[Jack et al., 2003] Jack, C., Slomkowski, M., Gracon, S., et al. (2003). MRI as a biomarker of disease progression in a therapeutic trial of milameline for AD. *Neurology*, 60(2):253–260. (Cited on page 2.)

[Jenkinson and Smith, 2001] Jenkinson, M. and Smith, S. (2001). A global optimisation method for robust affine registration of brain images. *Medical Image Analysis*, 5(2):143–156. (Cited on page 114.)

[Jolly et al., 2010] Jolly, M.-P., Guetter, C., and Guehring, J. (2010). Cardiac segmentation in MR cine data using inverse consistent deformable registration. In *ISBI*, pages 484–487. (Cited on page 19.)

[Joshi et al., 2004a] Joshi, S., Davis, B., Jomier, B. M., and B, G. G. (2004a). Unbiased diffeomorphic atlas construction for computational anatomy. *Neuroimage*, 23:151–160. (Cited on page 20.)

[Joshi et al., 2004b] Joshi, S., Davis, B., Jomier, M., and Gerig, G. (2004b). Unbiased diffeomorphic atlas construction for computational anatomy. *NeuroImage*, pages S151–S160. (Cited on page 72.)

[Joshi and Miller, 2000] Joshi, S. and Miller, M. (2000). Landmark matching via large deformation diffeomorphisms. *IEEE Transactions on Image Processing*, 9(8):1357–1370. (Cited on page 72.)

[Khesin and Wendt, 2009] Khesin, B. A. and Wendt, R. (2009). *The Geometry of Infinite Dimensional Lie groups*, volume 51 of *Ergebnisse der Mathematik und ihrer Grenzgebiete. 3. Folge / A Series of Modern Surveys in Mathematics*. Springer Verlag. (Cited on page 68.)

[Kheyfets et al., 2000] Kheyfets, A., Miller, W., and Newton, G. (2000). Schild's Ladder parallel transport for an arbitrary connection. *International Journal of Theoretical Physics*, 39(12):41–56. (Cited on pages 45 and 67.)

[Klein et al., 2009] Klein, A., Andersson, J., Ardekani, B., and et al. (2009). Evaluation of 14 nonlinear deformation algorithms applied to human brain mri registration. *NeuroImage*, 46(3):786–802. (Cited on pages 29 and 30.)

[Kolev, 2007] Kolev, B. (2007). Groupes de lie et mécanique. http://www.cmi.univ-mrs.fr/ kolev/. Notes of a Master course in 2006-2007 at Université de Provence. (Cited on page 66.)

[KSchild, 1970] KSchild, A. (1970). Tearing geometry to pieces: More on conformal geometry. unpublished lecture at Jan. 19 1970 Princeton Univesity relativity seminar. (Cited on pages 45 and 67.)

[Lamecker and Pennec, 2010] Lamecker, H. and Pennec, X. (2010). Atlas to image-with-tumor registration based on demons and deformation inpainting. In *Proc. MICCAI Workshop on Computational Imaging Biomarkers for Tumors - From Qualitative to Quantitative (CIBT'2010)*, Beijing. (Cited on page 143.)

[Leow et al., 2007] Leow, A., Yanovsky, I., Chiang, M., Lee, A., et al. (2007). Statistical properties of jacobian maps and the realization of unbiased large-deformation nonlinear image registration. *TMI*, 26(6):822–832. (Cited on page 21.)

[Leung et al., 2010] Leung, K., Barnes, J., Ridgway, G., et al. (2010). Automated cross-sectional and longitudinal hippocampal volume measurement in mild cognitive impairment and alzheimer's disease. *NeuroImage*, 51(4):1345 – 1359. (Cited on pages 102, 107, 116 and 117.)

[Leung et al., 2009] Leung, K. K., Clarkson, M. J., Bartlett, J. W., Clegg, S., Jack, C. R., Weiner, M. W., Fox, N. C., and Ourselin, S. (2009). Robust atrophy rate measurement in Alzheimer's disease using multi-site serial MRI: 2 tissue-specific intensity normalization and parameter selection. *NeuroImage*, 59. (Cited on pages 21 and 32.)

[Long et al., 2012] Long, X., Liao, W., Liang, D., Qiu, B., and Zhang, L. (2012). Healthy aging: An automatic analysis of global and regional morphological alterations of human brain. *Acad Radiol.*, 14. (Cited on page 122.)

[Lorenzi et al., 2010a] Lorenzi, M., Ayache, N., Frisoni, G., and Pennec, X. (2010a). 4D registration of serials brain's MR images: A robust measure of changes applyed to Alzheimer's disease. *Spatio Temporal Image Analysis Workshop (STIA), MICCAI.* (Cited on pages 44, 93 and 95.)

[Lorenzi et al., 2012a] Lorenzi, M., Ayache, N., Frisoni, G., and Pennec, X. (2012a). Disentangling the normal aging from the pathological alzheimer's disease progression on cross-sectional structural mr images. In *Virtual Physiological Human European Conference*. London. (Cited on pages 10, 12, 33 and 111.)

[Lorenzi et al., 2010b] Lorenzi, M., Ayache, N., Frisoni, G. B., and Pennec, X. (2010b). 4D registration of serial brain's MR images: a robust measure of changes applied to Alzheimer's disease . In *Spatio-Temporal Image Analysis workshop, MICCAI*. (Cited on pages 12 and 139.)

[Lorenzi et al., 2011a] Lorenzi, M., Ayache, N., Frisoni, G. B., and Pennec, X. (2011a). Mapping the effects of Aβ_{1-42} levels on the longitudinal changes in healthy aging: hierarchical modeling based on stationary velocity fields. In *MICCAI*, LNCS, pages 663–670. Springer. (Cited on pages 10, 11, 20, 62, 91, 103, 115, 116, 124, 126 and 139.)

[Lorenzi et al., 2011b] Lorenzi, M., Ayache, N., and Pennec, X. (2011b). Schild's Ladder for the parallel transport of deformations in time series of images. In *Information Processing in Medical Imaging - IPMI*, volume 22, pages 463–474. (Cited on pages 9, 11, 41, 42, 48, 62, 67, 79, 84, 93 and 95.)

[Lorenzi et al., 2012b] Lorenzi, M., Ayache, N., and Pennec, X. (2012b). LCC-Demons: a robust and accurate diffeomorphic registration algorithm. *Submitted to Medical Image Analysis*. (Cited on pages 9 and 11.)

[Lorenzi et al., 2012c] Lorenzi, M., Ayache, N., and Pennec, X. (2012c). Parallel transport of deformations in time series of images: Schild's and Pole ladders. *In preparation*. (Cited on page 42.)

[Lorenzi et al., 2012d] Lorenzi, M., Ayache, N., and Pennec, X. (2012d). Regional flux analysis of longitudinal atrophy in alzheimer's disease. In *MICCAI*, LNCS. Springer. (Cited on pages 10, 12, 33, 101, 114 and 125.)

[Lorenzi et al., 2012e] Lorenzi, M., Ayache, N., Pennec, X., and Frisoni, G. (2012e). Disentangling the normal aging from the pathological alzheimer's disease progression on cross-sectional structural mr images. In *NIBAD Workshop, MICCAI*. (Cited on pages 11, 12, 33 and 121.)

[Lorenzi et al., 2010c] Lorenzi, M., Donohue, N., Paternicò, D., Scarpazza, C., Ostrowitzki, S., Blin, O., Irving, E., and Frisoni, G. (2010c). Enrichment through biomarkers in clinical trials of alzheimerâĂŹs drugs in patients with mild cognitive impairment. *Neurobiology of Aging*, 31(8):1443 – 1451. (Cited on pages 11, 12 and 147.)

[Lorenzi and Pennec, 2011] Lorenzi, M. and Pennec, X. (2011). Geodesics, parallel transport & one-parameter subgroups for diffeomorphic image registration. In *Mathematical foundations of computational anatomy - MICCAI workshop*. (Cited on pages 9 and 12.)

[Lorenzi and Pennec, 2012] Lorenzi, M. and Pennec, X. (2012). Geodesics, parallel transport & one-parameter subgroups for diffeomorphic image registration. *Submitted to International Journal of Computer Vision - IJCV*. (Cited on pages 9, 11 and 60.)

[Lötjönen et al., 2011] Lötjönen, J., Wolz, R., Koikkalainen, J., Julkunen, V., Thurfjell, L., Lundqvist, R., Waldemar, G., Soininen, H., and Rueckert, D. (2011). Fast and robust extraction of hippocampus from mr images for diagnostics of alzheimer's disease. *NeuroImage*, 56(1):185–196. (Cited on page 6.)

[Lowe et al., 2009] Lowe, V. J., Kemp, B. J., Jack, C. R., Senjem, M., Weigand, S., Shiung, M., Smith, G., Knopman, D., Boeve, B., Mullan, B., and Petersen, R. C. (2009). Comparison of 18F-FDG and PiB PET in cognitive impairment. *J Nucl Med*, 50(6):878–86. (Cited on page 134.)

[Maes et al., 1997] Maes, F., Collignon, A., Vandermeulen, D., Marchal, G., and Suetens, P. (1997). Multimodality image registration by maximization of mutual information. *IEEE Trans. Med. Imaging*, pages 187–198. (Cited on page 19.)

[Mansi et al., 2010] Mansi, T., Pennec, X., Sermesant, M., Delingette, H., and Ayache, N. (2010). Logdemons revisited: Consistent regularisation and incompressibility constraint for soft tissue tracking in medical images. In *Proceedings of Medical Image Computing and Computer Assisted Intervention (MICCAI)*, volume 13, pages 652–659. (Cited on pages 23, 25 and 103.)

[Mansi et al., 2011a] Mansi, T., Pennec, X., Sermesant, M., Delingette, H., and Ayache, N. (2011a). iLogDemons: A Demons-based registration algorithm for tracking incompressible elastic biological tissues. *International Journal of Computer Vision*, 92(1):92–111. (Cited on pages 20, 62, 72, 135 and 144.)

[Mansi et al., 2011b] Mansi, T., Voigt, I., Leonardi, B., Pennec, X., Durrleman, S., Sermesant, M., Delingette, H., Taylor, A., Boudjemline, Y., Pongiglione, G., and Ayache, N. (2011b). A statistical model for quantification and prediction of cardiac remodelling: Application to tetralogy of fallot. *IEEE Transactions on Medical Images*, 30(9):1605–1616. (Cited on page 61.)

[McLeod et al., 2012] McLeod, K., Seiler, C., Sermesant, M., and Pennec, X. (2012). A near-incompressible poly-affine motion model for cardiac function analysis. *Proc. of MICCAI Workshop on Statistical Atlases and Computational Models of the Heart: Mapping Structure and Function (STACOM2012)*. (Cited on pages 20 and 135.)

[Miller et al., 2002] Miller, M., Trouvé, A., and Younes, L. (2002). On the metrics and euler-lagrange equations of computational anatomy. *Annu. Rev. Biomed. Rev.*, 4:375–405. (Cited on pages 44, 61 and 92.)

[Milnor, 1984] Milnor, J. (1984). Remarks on infinite-dimensional Lie groups. In *Relativity, Groups and Topology*, pages 1009–1057. Les Houches. (Cited on page 69.)

[Misner et al., 1973] Misner, C. W., Thorne, K. S., and Wheeler, J. (1973). *Gravitation*. W.H. Freeman and Compagny. (Cited on pages 45 and 67.)

[Modat et al., 2011] Modat, M., Ridgway, G., Daga, P., Cardoso, M., Hawkes, D., Ashburner, J., and Ourselin, S. (2011). Log-euclidean free-form deformation. In *Proc. of SPIE Medical Imaging 2011*. SPIE. (Cited on pages 20 and 70.)

[Modersitzki, 2004] Modersitzki, J. (2004). *Numerical Methods for Image Registration*. Oxford University Press. (Cited on page 4.)

[Mueller et al., 2005] Mueller, S., Weiner, M., Thal, L., and et al. (2005). The Alzheimer's disease neuroimaging initiative. *Neuroimaging Clin.*, 15:869–877. (Cited on pages 96 and 103.)

[Nelson et al., 2011] Nelson, P. T., Head, E., Schmitt, F., Davis, P., et al. (2011). AlzheimerâĂŹs disease is not "brain aging": neuropathological, genetic, and epidemiological human studies. *Acta Neuropathol.*, 121(5):571–587. (Cited on page 122.)

[Palmer, 2011] Palmer, A. (2011). Neuroprotective therapeutics for Alzheimer's disease: progress and prospects. *Trends Pharmacol Sci*, 32(3):141–147. (Cited on page 2.)

[Patenaude et al., 2011] Patenaude, B., Smith, S., Kennedy, D., and Jenkinson, M. (2011). A bayesian model of shape and appearance for subcortical brain. *NeuroImage*, 56(3):907–922. (Cited on pages 31, 96 and 115.)

[Pennec and Arsigny, 2012] Pennec, X. and Arsigny, V. (2012). Exponential Barycenters of the Canonical Cartan Connection and Invariant Means on Lie Groups. In Barbaresco, F., Mishra, A., and Nielsen, F., editors, *Matrix Information Geometry*. Springer. (Cited on pages 65 and 66.)

[Peyrat et al., 2008] Peyrat, J., Delingette, H., Sermesant, M., and Pennec, X. (2008). Registration of 4D time-series of cardiac images with multichannel diffeomorphic demons. In *Proceedings of Medical Image Computing and Computer Assisted Intervention (MICCAI)*, volume 11, pages 972–979. (Cited on page 139.)

[Postnikov, 2001] Postnikov, M. M. (2001). *Geometry VI: Riemannian Geometry*. Encyclopedia of mathematical science. Springer. (Cited on pages 62, 64, 65, 66 and 95.)

[Qiu et al., 2009] Qiu, A., Albert, M., Younes, L., and Miller, M. (2009). Time sequence diffeomorphic metric mapping and parallel transport track time-dependent shape changes. *Neuroimage*, 45(1). (Cited on page 44.)

[Qiu et al., 2008a] Qiu, A., Younes, L., Miller, M., and Csernansky, J. (2008a). Parallel transport in diffeomorphisms distinguish the time-dependent pattern of hippocampal surface deformation due to healthy aging and dementia of the Alzheimer's type. *Neuroimage*, 40(1). (Cited on page 44.)

[Qiu et al., 2008b] Qiu, A., Younes, L., Miller, M. I., and Csernansky, J. G. (2008b). Parallel transport in diffeomorphisms distinguishes the time-dependent pattern of hippocampal surface deformation due to healthy aging and the dementia of the Alzheimer's type. *Neuroimage*, 40(1):68–76. (Cited on page 6.)

[Rao et al., 2004] Rao, A., Chandrashekara, R., Sanchez-Hortiz, G., Mohiaddin, R., aljabar, P., Hajnal, J., Puri, B., and Rueckert, D. (2004). Spatial trasformation of motion and deformation fields using nonrigid registration. *IEEE Transactions on Medical Imaging*, 23(9). (Cited on pages 44 and 61.)

[Raschetti et al., 2007] Raschetti, R., Albanese, E., Vanacore, N., and Maggini, M. (2007). Cholinesterase inhibitors in mild cognitive impairment: A systematic review of randomised trials. *PLoS Med*, 4(11):e338. (Cited on page 7.)

[Reiman et al., 2010] Reiman, E., Langbaum, J., and Tariot, P. (2010). Alzheimer's prevention initiative: a proposal to evaluate presymptomatic treatments as quickly as possible. *Biomark Med*, 4(1):3–14. (Cited on page 2.)

[Ren et al., 2009] Ren, W., Singh, S., Singh, M., and Zhu, Y. (2009). State-of-the-art on spatio-temporal information-based video retrieval. *Pattern Recognition*, 42:267–282. (Cited on page 139.)

[Resnik et al., 2000] Resnik, S., Goldszal, A., C., Davatzikos, Golski, S., Kraut, M., Metter, E., Bryan, R., and Zonderman, A. (2000). One year age changes in MRI brain volumes in older adults. *Cerebral Cortex*, 10:464–472. (Cited on pages 20 and 112.)

[Riddle et al., 2004] Riddle, W. R., Li, R., Fitzpatrick, J. M., DonLevy, S. C., Dawant, B. M., and Price, R. R. (2004). Characterizing changes in MR images with color-coded Jacobians. *Magn Reson Imaging*, 22(6):769–777. (Cited on pages 5 and 20.)

[Ridha et al., 2006] Ridha, B., Barnes, J., Bartlett, J., Godbolt, A., Pepple, T., Rossor, M., and Fox, N. (2006). Tracking atrophy progression in familial alzheimer's disease: a serial MRI study. *Lancet Neurol*, 5:828–834. (Cited on page 112.)

[Scahill et al., 2002] Scahill, R., Schott, J., Stevens, J., Rossor, M., and Fox, N. (2002). Mapping the evolution of regional atrophy in alzheimer's disease: unbiased analysis of fluid-registered serial MRI. *Proc Natl Acad Sci*, 99:4703–4707. (Cited on pages 5 and 122.)

[Schmid, 2004] Schmid, R. (2004). Infinite dimensional lie groups with applications to mathematical physics. *J. Geometry and Symmetry in Physics*, 1:1âĂŞ67. (Cited on page 68.)

[Schmid, 2010] Schmid, R. (2010). Infinite-Dimensional Lie Groups and Algebras in Mathematical Physics. *Advances in Mathematical Physics*, 2010:1–36. (Cited on page 69.)

[Schott et al., 2010] Schott, J. M., Bartlett, J., Fox, N., Barnes, J., and the Alzheimer's Disease Neuroimaging Initiative Investigators (2010). Increased brain atrophy rates in cognitively normal older adults with low cerebrospinal fluid Ab1-42. *Annals of Neurology*, 68-6. (Cited on pages 98, 116 and 117.)

[Seiler et al., 2011a] Seiler, C., Pennec, X., and Reyes, M. (2011a). Geometry-aware multiscale image registration via obbtree-based polyaffine log-demons. In *Proceedings of Medical Image Computing and Computer Assisted Intervention (MICCAI)*, pages 631–638, Berlin, Heidelberg. Springer-Verlag. (Cited on page 20.)

[Seiler et al., 2011b] Seiler, C., Pennec, X., and Reyes, M. (2011b). Geometry-Aware Multiscale Image Registration Via OBBTree-Based Polyaffine Log-Demons. In *Medical Image Computing and Computer-Assisted Intervention - MICCAI*, volume 14, pages 631–638. (Cited on page 62.)

[Shattuck et al., 2008] Shattuck, D., Mirza, M., Adisetiyo, V., Hojatkashani, C., Salamon, G., Narr, K., Poldrack, R., Bilder, R., and Toga, A. (2008). Construction of a 3D probabilistic atlas of human cortical structures. *NeuroImage*, 39(3):1064–1080. (Cited on page 75.)

[Shen and Davatzikos, 2004] Shen, D. and Davatzikos, C. (2004). Measuring temporal morphological changes robustly in brain MR via 4-dimensional template warping. *NeuroImage*, 21:1508–1517. (Cited on pages 139 and 140.)

[Siless et al., 2012] Siless, V., Glaunés, J., Guevara, P., Mangin, J.-F., Poupon, C., Bihan, D., Thirion, B., and Fillard, P. (2012). Joint T1 and brain fiber Log-Demons registration using currents to model geometry. In Ayache, N., Delingette, H., Golland, P., and Mori, K., editors, *Medical Image Computing and Computer-Assisted Intervention, MICCAI 2012*, volume 7511 of *Lecture Notes in Computer Science*, pages 57–65. Springer Berlin Heidelberg. (Cited on pages 20 and 134.)

[Smith, 2002] Smith, S. (2002). Fast robust automated brain extraction. *Human Brain Mapping*, 17(3). (Cited on pages 6 and 31.)

[Smith et al., 2002] Smith, S., Zhang, Y., Jenkinson, M., Chen, J., Matthews, P., Federico, A., and Stefano, N. D. (2002). Accurate, robust, and automated longitudinal and cross-sectional brain change analysis. *NeuroImage*, 17. (Cited on pages 25 and 112.)

[Stefanescu, 2005] Stefanescu, R. (2005). Parallel nonlinear registration of medical images with a priori information on anatomy and pathology. *PhD thesis*. (Cited on page 19.)

[Stefanescu et al., 2004] Stefanescu, R., Commowick, O., Malandain, G., Bondiau, P.-Y., Ayache, N., and Pennec, X. (2004). Non-rigid atlas to subject registration with pathologies for conformal brain radiotherapy. In *In MICCAI*, pages 704–711. Springer Verlag. (Cited on page 143.)

[Stretton et al., 2011] Stretton, E., Mandonnet, E., Geremia, E., Menze, B. H., Delingette, H., and Ayache, N. (2011). Predicting the location of glioma recurrence after a resection surgery. In *Proceedings of 2nd International MICCAI Workshop on Spatiotemporal Image Analysis for Longitudinal and Time-Series Image Data (STIA'12)*, LNCS, Nice. Springer. (Cited on pages 136 and 143.)

[Studholme et al., 1996] Studholme, C., Hill, D., and Hawkes, D. (1996). Automated 3-d registration of mr and ct images of the head. *Medical Image Analysis*, 1(2):163–175. (Cited on page 19.)

[Sweet and Pennec, 2010] Sweet, A. and Pennec, X. (2010). Log-domain diffeomorphic registration of diffusion tensor images. *Proc. of WBIR: Workshop on Biomedical Image Registration*. (Cited on page 20.)

[Thompson et al., 2003] Thompson, P., Ayashi, K., Zubicaray, G., Janke, A., Rose, S., Semple, J., Herman, D., Hong, M., Dittmer, S., Dodrell, D., and Toga, A. (2003). Dynamics of gray matter loss in Alzheimer's disease. *The Journal of Neuroscience*, 23:994–1005. (Cited on pages 6, 20, 61, 102 and 112.)

[Tosun et al., 2010] Tosun, D., Schuff, N., Truran-Sacrey, D., and et al. (2010). Relations between brain tissue loss, csf biomarkers, and the apoe genetic profile: a longitudinal MRI study. *Neurobiol Aging*, 31-8. (Cited on pages 98 and 126.)

[Trouvé, 1998] Trouvé, A. (1998). Diffeomorphisms groups and pattern matching in image analysis. *Int. J. Comput. Vision*, 28(3):213–221. (Cited on page 20.)

[Tustison et al., 2010] Tustison, N., Avants, B., Cook, P., Zheng, Y., Egan, A., Yushkevich, P., and Gee, J. (2010). N4ITK: Improved N3 bias correction. *IEEE Transaction in Medical Imaging*, 19. (Cited on page 28.)

[van der Lijn et al., 2008] van der Lijn, F., den Heijer, T., Breteler, M. M. B., and Niessen, W. J. (2008). Hippocampus segmentation in MR images using atlas registration, voxel classification, and graph cuts. *NeuroImage*, 43:708–720. (Cited on page 6.)

[Vasilevskiy and Siddiqi, 2002] Vasilevskiy, A. and Siddiqi, K. (2002). Flux maximizing geometric flows. *IEEE Trans. Pattern Anal. Mach. Intell.*, 24(12):1565–1578. (Cited on page 31.)

[Vercauteren, 2008] Vercauteren, T. (2008). *Image Registration and Mosaicing for Dynamic In Vivo Fibered Confocal Microscopy*. Phd thesis, École Nationale Supérieure des Mines de Paris. (Cited on pages 24 and 35.)

[Vercauteren et al., 2008] Vercauteren, T., Pennec, X., Perchant, A., and Ayache, N. (2008). Symmetric Log-domain diffeomorphic registration: A Demons-based approach. In *Proceedings of Medical Image Computing and Computer Assisted Intervention (MICCAI)*, volume 5241, pages 754–761. (Cited on pages 8, 20, 22, 49, 70, 71, 81, 92 and 93.)

[Wells et al., 1996] Wells, W., Viola, P., Atsumi, H., Nakajima, S., and Kikinis, R. (1996). Multi-modal volume registration by maximization of mutual information. *Medical Image Analysis*, 1(1):35–51. (Cited on page 19.)

[Wolz et al., 2011] Wolz, R., Julkunen, V., Koikkalainen, J., Niskanen, E., Zhang, D. P., Rueckert, D., Soininen, H., and Löjönen, J. (2011). Multi-method analysis of mri images in early diagnostics of Alzheimer's disease. *PLoS One*, 6(10):e25446. (Cited on page 128.)

[Younes, 2007a] Younes, L. (2007a). Jacobi fields in groups of diffeomorphisms and applications. *Q. Appl. Math.* (Cited on pages 44 and 47.)

[Younes, 2007b] Younes, L. (2007b). Jacobi fields in groups of diffeomorphisms and applications. *Q. Appl. Math*, pages 113–134. (Cited on pages 61 and 82.)

[Younes, 2010] Younes, L. (2010). *Shapes and diffeomorphisms*. Number 171 in Applied Mathematical Sciences. Sprimger. (Cited on pages 68 and 69.)

[Younes et al., 2008] Younes, L., Qiu, A., Winslow, R., and Miller, M. (2008). Transport of relational structures in groups of diffeomorphisms. *J Math Imaging Vis*, 32(1). (Cited on pages 61 and 92.)

[Yushkevich et al., 2010] Yushkevich, P., Avants, B., Das, S., J.Pluta, Altinay, M., and Craige, C. (2010). Bias in estimation of hippocampal atrophy using deformation-based morphometry arises from asymmetric global normalization: An illustration in ADNI 3 T MRI data. *NeuroImage*, 50(2):434–445. (Cited on page 114.)

[Yushkevich et al., 2006] Yushkevich, P., Piven, J., Hazlett, H., Smith, R., Ho, S., Gee, J., and Gerig, G. (2006). User-guided 3D active contour segmentation of anatomical structures: Significantly improved efficiency and reliability. *Neuroimage*, 31(3). (Cited on page 53.)

Deformation based morphometry of the brain for the development of surrogate markers in Alzheimer's disease

Abstract: The aim of the present thesis is to provide an effective computational framework for the analysis and quantification of the longitudinal structural changes in Alzheimer's disease (AD). The framework is based on the diffeomorphic non-rigid registration parameterized by stationary velocity fields (SVFs), and is hierachically developed to account for the different levels of variability which characterize the longitudinal observations of T1 brain magnetic resonance images (MRIs). We developed an efficient and robust method for the quantification of the structural changes observed between pairs of MRIs. For this purpose, we propose the LCC-Demons registration framework which implements the local correlation coefficient as similarity metric, and we derived consistent and numerically stable measures of volume change and boundary shift for the regional assessment of the brain atrophy. In order to consistently analyze group-wise longitudinal evolutions, we then investigated the parallel transport of subject-specific deformation trajectories across different anatomical references. Based on the SVF parametrization of diffeomorphisms, we relied on the Lie group theory to propose new and effective strategies for the parallel transport of SVFs, with particular interest into the practical application to the registration setting. These contributions are the basis for the definition of qualitative and quantitative analysis for the pathological evolution of AD. We proposed several analysis frameworks which addressed the differentiation of pathological evolutions between clinical populations, the statistically powered evaluation of regional volume changes, and the clinical diagnosis at the early/prodromal disease stages. **Keywords:** Alzheimer's disease, non rigid registration, longitudinal analysis, structural MRI